MEDNARODNA PODIPLOMSKA ŠOLA JOŽEFA STEFANA
JOŽEF STEFAN INTERNATIONAL POSTGRADUATE SCHOOL

Joaquin Gabriel Miranda Mena

Phase separation in a 2D charged system

DOCTORAL DISSERTATION

LJUBLJANA, July 2010

Phase separarion in a 2D charged system

Joaquin Gabriel Miranda Mena

Doctoral Dissertation
Jožef Stefan International Postgraduate School
Ljubljana, Slovenia, June 2010

Evaluation Board:

Prof. Dr. Dragan Mihailović, Chairman, Jozef Stefan Institute, Jamova 39 SI-1000-Ljubljana.
Asst. Prof. Dr. Viktor Kabanov, Member, Jozef Stefan Institute, Jamova 39 SI-1000-Ljubljana.
Asst. Prof. Dr. Tomaž Mertelj, Member, Jozef Stefan Institute Jamova 39 SI-1000-Ljubljana.
Prof. Dr. Sasha Alexandrov, Member, Loughborough University, Loughborough, Leics LE11 3TU, United Kingdom.

MEDNARODNA PODIPLOMSKA ŠOLA JOŽEFA STEFANA
JOŽEF STEFAN INTERNATIONAL POSTGRADUATE SCHOOL

Joaquin Gabriel Miranda Mena

Phase separation in a 2D charged system

Doctoral Dissertation

Fazna separacija v 2D nabitem sistemu

Doktorska disertacija

Supervisor: Asst. Prof. Viktor Kabanov

Co-Supervisor: Asst. Prof. Tomaž Mertelj

June 2010

Contents

Povzetek

Glavni namen disertacije je opisati nehomogene faze v plastovitih sistemih. Le te nastanejo pod vplivom "tekmovanja" privlačnih z odbojno Coulombsko interakcijo. Pri obravnavi nehomogenih faz smo uporabili dva pristopa. Prvi temelji na uporabi Landauove teorije faznih prehodov, drugi pa na uporabi Monte Carlo simulacij na modelu elektronskega plina na mreži. V okviru prvega pristopa sem preučeval dva univerzalna razreda faznih prehodov z različnima tipoma sklopitve med parametrom reda in gostoto električnega naboja. Za razliko od Landauovega pristopa, pa v drugem pristopu govorimo o mikroskopskem izvoru privlačne interakcije med naboji, ki je opisana z mehanizmom Jahn-Teller (JT). Nehomogenosti v modelu elektronskega plina na mreži so torej rezultat privlačnih interakcij med polaroni JT in odbojne Coulombske interakcije. S pomočjo simulacij Monte Carlo smo v okviru tega modela preučili tudi električne prevodne lastnosti

Abstract.

The main purpose of this thesis is to describe the inhomogeneous phase of a layered system. The phase is the result of the competition between attractive interactions and the long range Coulomb repulsive force (LRCF). In order to achieve this, two different strategies are applied. The first is within the scheme of the Landau theory of phase transitions and the second is based on Monte Carlo simulations of a lattice gas model. An important feature addressed in the first approach is the coupling between the charge density and the order parameter in the presence of LRCF. For this purpose two universal classes of frustrated phase transitions were studied with different type of couplings. Although in the Landau treatment it is not possible to track the microscopic origin of the coupling with the charges, it is in the second approach where it is proposed that the coupling to the order parameter is realized throughout a Jahn-Teller mechanism. Hence, the inhomogeneities arising in the lattice gas model are identified as a result of the competition between short range anisotropic attractions between JT-polarons and the long range repulsion of these charged objects. Subsequently, throughout Monte Carlo simulations, electric transport properties of the systems with such type of coupling are presented.

Abbreviations

APES = adiabatic potential energy surface

ARPES = Angular resolved photo emission surface

CGM = Conjugated gradient method

E-ph = Electron-phonon

EXAFS = Extended X-ray absortion fine structure

JT = Jahn-Teller

HH = Holstein-Hubbard

HTS = High temperature superconductors

HTT = High temperature tetragonal

LRCI = Long range Coulomb interaction

LTO = Low-temperature orthorhombic

LTT = Low-temperature tetragonal

MC = Monte Carlo

PG = Pseudogap

STM = Scanning tunneling microscopic

VRH = Variable range hopping

Chapter 1

Introduction

1.1 Inhomogeneities and their functionality

Ever since our observation of nature we have been intrigued by the phenomena of pattern formations. The black and white stripes observed on the zebra or the colorful spectra given by oil-water mixtures are only two examples. The phenomena can equally appear at a cosmological scale (galaxy clusters) down to a microscopic scale. For instance, different microscopic resolutions have revealed us the symmetry of a snow-flake or a twisted filament of the DNA molecule. Why a system is more likely to be found structured in a pattern rather than in a homogeneous state? What are agents that lead to such formations? Do the patterns have a specific function?

Similar phenomena of pattern formations have been observed in solid state physics. Diverse phenomena related to phase separation have been observed in recent years in a wide variety of materials. They appear at different length scales. As a consequence they have fueled the interest of material scientists. The interest is not fortuitous, they might lead to important and novel properties.

The thesis deals with a specific type of materials in the solid state physics. These are layered systems which tend to form charged textures. The point of view presented throughout the thesis is that patterns are the result of two competing forces. One force which attempts to get together the individual components of system and a second which counterbalances it, trying to keep them far apart. More specifically, charges constrained to a plane and subject to the antagonist presence of short-range attractive forces and long-range Coulomb interaction (LRCI). Often the arrangement arising from these kinds of driven forces is referred as 'self-organized'.

Regarding the subject of pattern functionality, we can adopt a perspective similar to the process of the transition from a gas state to a solid state. After the gas condensation new properties appear. One example is the electrical conductivity. We may end up with a conductor, semiconductor or an insulator, depending on the initial type of atoms and the process of condensation. In the same manner, we could induce a new property to a material throughout the formation of inhomogeneities. Thus, one new frontier of material science is controlling the conditions for "self-assembly" processes. The process has to be done in a such manner that the material can deliver the desired property. This implies the knowledge of tuning the right parameters.

1.2 Relevance of inhomogeneities in transition metal oxides

Experimental techniques suitable to probe either the charge, spin or lattice arrangement have revealed inhomogeneous phases in different materials. They are formed at the mesoscopic level and often in low dimensional systems. In some cases the mechanism for their formation might be the following. Particles interacting solely by some sort of attraction at microscopic origin create macroscopic regions. However, if the particles are charged and the LRCI is present, the formation of large agglomerations is prevented. Moreover, it might lead to charged "microemulsions" as suggested in theoretical works [1]. In the same manner, although Coulomb interaction is common in electronic systems, it is just recently that their subtle effects in two dimensional (2D) systems is understood. For instance, the metal insulator transition in a Si metal oxide semiconductor field transistors [2] and in hole doped 2D GaS [3] cannot be explained in terms of the classical Fermi-liquid theory. The coexistence of metallic and insulating regions suggests a new mechanism for the unusual conductivity they present [4]. Moreover, the metallic state is found in the intermediate doping range where a frustrated first order phase transition between Wigner crystal and Fermi liquid occurs.

Among the materials which have presented signatures of inhomogeneities are the transition metal oxides. Manganites, cuprates, nickelates, rhutenates and pnictides fall into this classification[5]. In these materials the energies of charge, lattice, orbital and spin states are aften close in energy. Therefore, they may develop distinctive properties when they are subject to external agents, e.g. pressure, doping and temperature variations. As a result of this complexity, novel behaviors and phases may arise.

Special attention has been given to the high temperature superconductivity (HTS) in cuprates and the colossal magnetoresistance (CMR) in manganites. It is plausible that

both families of materials present the Jahn-Teller (JT) distortions [6–10]. These local instabilities might assist the coupling of charges leading to formation of bipolarons and possibly polaron domains. More importantly, the JT effect has been proposed as one of the key elements for the mechanism of CMR [9, 11, 12] and HTS. Spatially resolving techniques revealed the presence of stripes in the so-called pseudogap phase of the high-temperature superconductors [13]. Manganites, which are characterized by their colossal magnetoresistance, present a striped phase as well [14, 15]. Although the transition from a paramagnetic-insulator to a ferromagnetic metal in manganites and the superconducting transition in HTS cuprates have different origin, it is plausible that the JT mechanism is playing a key role. These two classes of the transition metal oxides are excellent candidates for the present work.

Regarding the inhomogeneous phase in the cuprates and its link to lattice instabilities, ARPES and inelastic neutron scattering experiments showed that phonon anomalies in the form of local modes [16–18] are within an energy scale corresponding to the so called pseudogap (PG). The energy of the PG was reported by NMR, tunneling and femtosecond pump-probe experiments [19, 20]. The origin of the PG is an issue of a long debate because it could be regarded as a precursor to the HTS in the cuprates. Thus, some theories consider that the superconducting transition is achieved in two steps. First pairs are created at $T = T^*$ and the energy scale responsible for the pairing is identified with the PG. Subsequently pairs would form the supercondutor condensate at $T = T_c < T^*$. Some electronic theories identify the PG as a spin gap. But from the point of view of electron-phonon interactions, it is related to the energy of charge confinement by lattice distortions. For example, structural distortions detected by local structural probes [13] prompt to associate local vibration modes with lattice instabilities.

The PG energy has been related with a type of electronic organization. In particular, at doping 1/8 the stripe phase is observed in diverse experiments. This type of order is a topic of an intense debate. Although there is a consensus that such an order is present, there is no agreement whether the overall effect is advantageous for the superconductivity. Neither it is clear what is the nature of the interaction dominating in the temperature region where stripes or other types of inhomogeneities are present. For example, the spin gap nature of this type of order was put forward in recent spin dynamics measurements [21] along with the predictions of a novel order state emerging from magnetic interactions [22].

1.3 Organization of the thesis

The thesis is organized in two parts. The first part starts with an introduction of the Landau formalism of phase transitions. In the subsequent two chapters we apply this formalism for the description of charged inhomogeneities. Chapter three and four are concerned with two types of coupling between the order parameter and the charge density, both in the presence of LRCI. At the end of each chapter three and four we discuss the effect of disorder.

The second part uses statistical physics to address the phase separation. Here we present a lattice-gas model where the JT instabilities are represented by pseudospins; in addition the model allows to include LRCI. In order to understand what is the context of this part, some details regarding the JT effect are given in chapter five. The original model targets the inhomogeneous phase in cuprates. In the same chapter, two concepts related to the JT effect are also discussed: the formation of polarons and bipolarons. Details of the Monte Carlo method are given in chapter six. Within this chapter, we proceed to show the density of states (DOS) and their associated patterns. After a short introduction to variable range hopping (VRH) in chapter seven we present the single polaron and bipolaron mobility.

Chapter 2

Landau theory of phase transitions

2.1 Introduction

The technique we use to describe inhomogeneities in chapter three and four relies on the theory of phase transitions introduced by L. D. Landau [23]. It provides an important thermodynamic method based on the collective behavior of particles. Usually it is called phenomenological, because it predicts the transition without considering microscopic details. It is a powerful theory; especially since it often leads to a differential equation which may be less complicated than the full microscopic treatment. Additionally, the approach offers a unified scheme for other mean field theories. Among them we find the van der Wals theory of vapor-liquid transition, the Weiss model for paramagnetic-ferromagnetism transition, the Bragg-Williams model for order-disorder transition in alloys and the Bardeen-Cooper-Schrieffer theory of superconductivity. This chapter introduces some of the elements of such approach which will be used in the following two chapters. The chapter provides the concept of the order parameter as well as the thermodynamic potentials that describe first or second order phase transitions. The potentials will be intimately related to the two kinds of couplings given in chapters three and four.

2.2 Response functions

We observe that, when the temperature is decreased, some material may acquire new properties that originally were absent at higher temperatures. For instance, water can be

transformed from gas into liquid or solid. A ferroelectric material develops polarization. Metals may become superconductors. In order to pinpoint these transitions we need to rely on measurements that not only quantify but also classify them. Experimentally a phase transition is said to happen when the measurement of a response function, which can include the presence of a control parameter, diverges near the characteristic temperature of a system. For example, the specific heat, the magnetic and the electric susceptibility are the relevant response functions in the vapor-liquid, the paramagnetic-magnetic and the paraelectric-ferroelectric transitions, respectively. In the first case the transition is attributed to a first order phase transition.

The classification of the transitions was done on the basis of the classical Erhnest classification of phase transitions [24]. The criteria is the absence of analyticity of the free energy at a certain order of the derivative. It can be easily demonstrated that the transition is reflected in the response functions because they are directly related to the derivatives of the internal energy of the system. More accurate, the thermodynamic potential which describes the energy in terms of thermodynamic variables. The most common variables are temperature, pressure and chemical potential.

2.3 Landau description of phase transitions

We owe to the work of Lev D. Landau in 1937 the existence of a phenomenological theory that allows us to deal with phase transitions. The insight of Landau relies on the polynomial expansion, near the transition temperature, of the free energy in terms of a variable named "order parameter" and commonly denoted as η. The method originally describes second order phase transitions, but it can be extended to the first order transitions.

According to Landau, the symmetry of the system in the high or low temperature phase should be reflected by η. This parameter is an ensemble average of microscopic variables, σ, whose magnitude depends on the position i: $\eta \sim < \sigma_i >$. The interaction among different σ_i in the system might be correlated across the volume that occupies the system. At high temperature the material is in the high symmetry phase and the order parameter is equal to zero. If, during the process of lowering the temperature, the order parameter takes a finite value at a critical temperature $T = T_c$, then the phase transition takes place. This is due to the fact that for $T > T_c$ those variables σ_i are usually in a fast random motion, hence their time average $< \sigma_i >_t$ vanishes at each lattice point and hence is independent of the site i. In contrast, below T_c the microscopic σ_i's are in a slow motion and correlated. For $T < T_c$ the states have reduced the symmetric group with respect to the high-T one.

In the three cases mentioned above the natural order parameters are the water density, the magnetization and the electric polarization. It is easy to visualize the concept of symmetry breaking for the two latter cases. At high temperature, single spins are randomly oriented in the paramagnetic state given a net magnetization of zero. Similarly, in the paraelectric state unaligned electric dipoles produce a zero electric field. It is said that both systems are in the disordered states. The spins and dipoles can be regarded as the microscopic variables defined before as σ. As soon as the temperature approaches T_c, let's say the Curie temperature for a magnetic material, the spins choose a preferential orientation. This breaks the time reverse operation, due to a net value of magnetization. In the ferroelectric transition there is a spontaneous electric polarization. For the liquid-vapor phase transformation it is the variations of the molecular density which can help us to describe the transition.

Following Landau, the expansion of the free energy, (F) in terms of the order parameter, near the vicinity of a phase transition, is

$$F = F_0 + \alpha\eta + A\eta^2 + C\eta^3 + B\eta^4 + ..., \tag{2.1}$$

where F_0 is the free energy in the symmetric state. In general the coefficients may be functions of temperature (T) pressure (P) and external fields (h). The combination of the signs and values of the coefficients allows to construct a description of a second or a first order phase transition. Whether terms up to sixth power are retained depends on the order of a transition.

2.3.1 Second order phase transitions

The stability condition for Eq. (2.1) implies that the minimum should satisfy,

$$\frac{\delta F}{\delta \eta} = 0, \tag{2.2}$$

$$\frac{\delta^2 F}{\delta \eta^2} > 0 \tag{2.3}$$

from here, the linear term is canceled out. When the phase transition is caused by changing the temperature, a proper selection of the coefficients as a function of T sets the transition. In addition, as the temperature is lowered, they must lead to a continuous change of η at the critical temperature $T = T_c$. According to the discussion in the previous section, for $T > T_c$ the system is in the highly symmetric phase with $\eta = 0$ so

it requires $A > 0$. While in the low symmetry regime, $T < T_c$, $\eta \neq 0$ and $A < 0$. Hence it is inferred that at $T = T_c$, $A = 0$. Then, we can assume that A has temperature dependence $T - T_c$: $A(T) = a * (T - T_c)$ with $a > 0$. When the phase transition point itself is stable of $T = T_c$ the conditions which also need to be fulfilled are

$$(\frac{\delta^2 F}{\delta \eta^2})_{\eta=0} = 0, \tag{2.4}$$

$$(\frac{\delta^4 F}{\delta \eta^4})_{\eta=0} > 0. \tag{2.5}$$

Symmetry considerations for η at $T < T_c$ may lead to $C = 0$. This is due to the invariance of η under a symmetry operation. For example the projection of spins and dipoles along the z axis of a crystal do not depend on either of the two possible directions. In general B may depend on T, but here it will be considered as weakly dependent on temperature. Therefore the final form of F is

$$F(T, \eta) = F_0 + A(T)\eta^2 + B\eta^4. \tag{2.6}$$

We obtain from $\delta F/\delta \eta = 0$, the solutions of the last equation:

$$\eta = 0, \tag{2.7}$$

$$\eta = \pm[a(T_c - T)/2B]^{1/2}. \tag{2.8}$$

The solution $\eta = 0$ is stable for $T \geq T_c$, while the real solutions to Eq. (2.8) do not exist for the same range of T. On the contrary $\eta = \pm\sqrt{A/2B}$ are the stable solutions at $T < T_c$ while $\eta = 0$ becomes unstable. The reference free energy is F_0 which is the energy in the non-ordered phase. The coefficients take values according to the experimental results or the first principles calculations. Figure 2.1 shows the free energy as function of η for the two representative temperatures. Such type of figures will use F_0 as the zero point of energy.

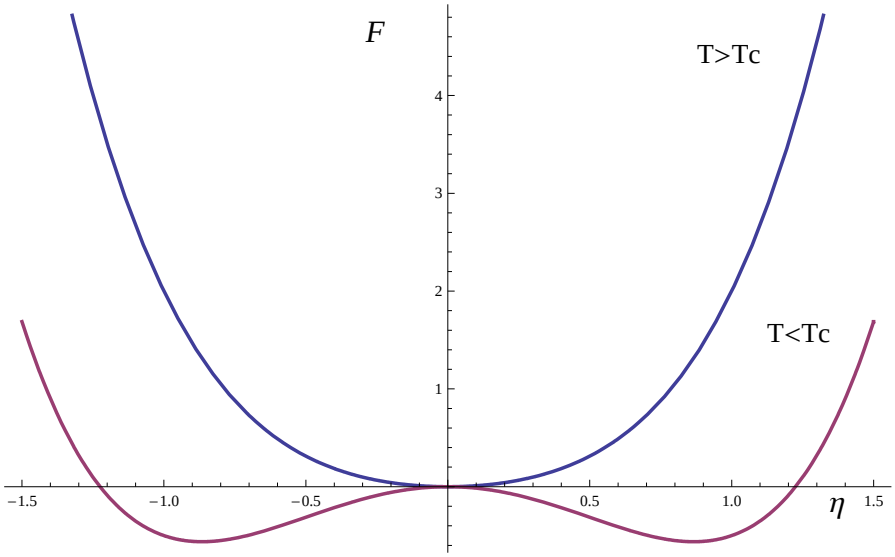

FIGURE 2.1: Representation of a second order phase transition. The minimums develop in such way that the order parameter, η, changes value continuously as the temperature is lowered. This is observed in the free energy for two temperatures $T > T_c$ (blue curve) and $T < T_c$ (purple curve).

2.3.2 First order phase transitions

The same theory of Landau originally conceived for second order phase transitions can be used for first order phase transitions. A first order phase transition can be introduced, if the polynomial expansion of the free energy is extended to the sixth order when $B < 0$.

$$F = F_0 + a(T - T_c)\eta^2 + B\eta^4 + D\eta^6. \tag{2.9}$$

Now in order to have F bounded from below, $D > 0$ is required. Then, the condition for a minimum solution, $\delta F/\delta\eta = 0$, leads to:

$$2a(T - T_c)\eta + 4B\eta^3 + 6D\eta^5 = 0. \tag{2.10}$$

Besides the trivial solution, $\eta = 0$, the other two solutions to this equation are given by

$$\eta^2 = \frac{-B \pm [B^2 - 3aD(T - T_c)]^{1/2}}{3D}. \tag{2.11}$$

The existence of the real values of this solution set an upper limit temperature, T_+.

$$T_+ = T_c + \frac{B^2}{3aD}, \tag{2.12}$$

It must be emphasized that T_+ is not the real transition temperature, though Eq. 2.11 can represent a metastable solution. We should see if F is larger or less than F_0 after Eq. 2.11 is substituted in Eq. 2.9. Indeed, the critical temperature (T_t), which will give place to the first order phase transition, is found from the condition $F - F_0 = 0$; this gives

$$D\eta^4 + B\eta^2 + a(T - T_c) = 0. \tag{2.13}$$

Solving the polynomial equation of the fourth order, we obtain solutions at

$$\eta^2 = -\frac{B \pm \sqrt{B^2 - 4Da(T_c - T)}}{2D}. \tag{2.14}$$

The solution for real values leads, together with T_c and T_+, to the third characteristic temperature:

$$T_t = T_c + \frac{B^2}{4aD}. \tag{2.15}$$

So at $T = T_t$ there are three minima at $\eta = 0$ and $\eta = \pm(-B/2D^{1/2})$. Therefore, the characteristic temperatures $T_c < T_t < T_+$ describe the following regimes. T_+ is the temperature where a second minima in η first appear. Yet $\eta = 0$ remains as the most stable for $T_t < T < T_+$. At $T = T_t$ the order parameter changes discontinuously from $\eta = 0$ to $\eta = \sqrt{-B/2D}$. Hence the change in entropy is

$$\Delta S = \frac{F_0 - F}{T} = \frac{aB}{2D} \tag{2.16}$$

For $T_c < T < T_t$, the ordered phase becomes stable, while disordered phase is metastable. Finally, at $T = T_c$, $\eta = 0$ becomes a spinodal point. T_c corresponds to the absolutely unstable limit of the disordered phase, and $\eta = \pm\sqrt{-2B/3D}$ are perfectly stable. The characteristic temperatures and typical regions can be seen in figures 2.2 and 2.3.

2.4 Ginzburg-Landau theory of phase transitions and domain structures

In the simplest form, the Landau theory leads to a uniform phase transition across the whole sample. The formalism needs to be modified if we want to include a phase

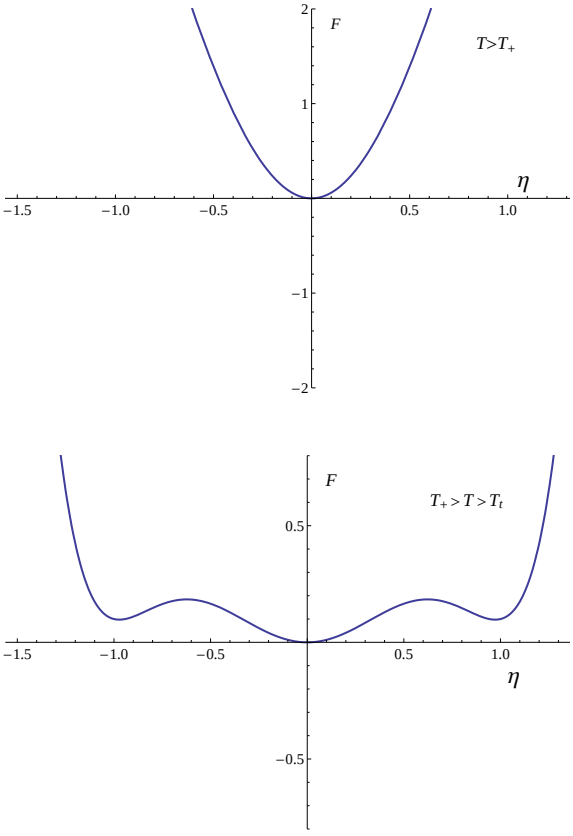

FIGURE 2.2: Two temperatures for a first order phase transition. Upper panel: the system is in a disordered state given by $\eta = 0$. Lower panel: the appearance of a meta-stable phase in the range $< T_t < T < T_+$.

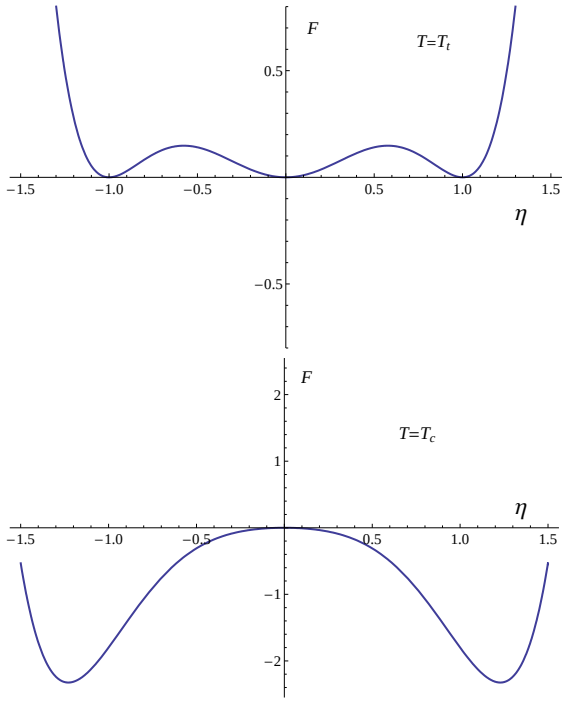

FIGURE 2.3: Two critical temperatures for the first order phase transition. Upper panel: at $T = T_t$, two phases are evenly competing. This is observed by triple minima. Lower panel: at $T = T_c$ the order phase has become the most stable.

separation. Thus, if we allow the order parameter to change as a function of coordinates, we can study domain formation and inhomogeneous phases. In this section we present some elements for an extended version to formalism of Landau [21].

Let us denote the order parameter $\eta = \eta(\overrightarrow{r})$. Then, we can define the density of the free energy as

$$f \equiv f(T, \eta(\mathbf{r}), \nabla\eta(\mathbf{r})), \tag{2.17}$$

and the free energy as

$$F = \int f(T, \eta(\mathbf{r}), \nabla\eta(\mathbf{r}))d\mathbf{r}. \tag{2.18}$$

As before, F can be expanded in powers of $\eta(\mathbf{r})$, where symmetry considerations must be taken into account. From the minimum of equation (2.18), the spatial variation of the order parameter and domain structure can be determined.

Since the order parameter is varying over distance generally the energy cost of the variation depends on $\partial\eta/\partial\mathbf{r} = \nabla\eta(\mathbf{r})$. For example, spins in a ferromagnet are aligned toward one direction and a slow variation in the the relative direction between them is energetically costly. The rate of the variation sets this extra energy. The extra free energy cost associated with the variation of $\eta(\mathbf{r})$ should be a function of $\partial\eta/\partial\mathbf{r}$ and, possibly also $\eta(\mathbf{r})$ itself. Therefore near T_c, the extra energy has the simple form

$$F_{grad} = \int C|\nabla\eta(\overrightarrow{r})|^2 d\mathbf{r}. \tag{2.19}$$

In addition, this is the only invariant (independent of the spatial orientation) containing $\nabla\eta(\mathbf{r})$. Thus,

$$F(T, \eta(\mathbf{r}), \nabla\eta(\mathbf{r})) = \int [A(T)\eta^2(\mathbf{r}) + B\eta^4(\mathbf{r}) + C|\nabla\eta(\overrightarrow{r})|^2] d\mathbf{r}. \tag{2.20}$$

It is the standard form of the Ginzburg-Landau functional for the translational-invariant case.

Chapter 3

Coulomb frustrated first order phase transition. The scalar order parameter.

3.1 Introduction

In the last chapter we introduced two thermodynamic potentials which describe phase transitions with a scalar order parameter. In addition, we included a space dependent order parameter, $\eta(\mathbf{r})$, and a gradient term, $C|\nabla\eta(\mathbf{r})|^2;C>0$, determines the energy cost of spatial variations of $\eta(\mathbf{r})$. However in order to achieve the phase separation we need to include two key elements. The first is the LRCI. The second represents a coupling between the charge density and $\eta(\mathbf{r})$. The coupling allows to describe the influence of the charge degree of freedom on the order parameter.

Recently, it was pointed out that doping of external charges into a system with fixed-charged background leads to a phase separation [1]. The origin of this type of phase transition could be traced when crossing from 3D to 2D systems [25]. In addition, Ortix et al [26]. included electronic compressibility between the two distinctive electronic phases. This extra term in the free energy modifies the critical value of charge density at which the system is phase-separated. An important effort to explain systematically the experimental evidence of phase separation in lanthanum and yttrium based cuprates was given by Fine and Egami [27]. They studied the curvature of the free energy of the two competing states as a function of charge concentration. They argued that the doping destroys the AF correlations and drives the phase separation presented in these materials. Moreover, antiferromagnetic phase transitions are associated with second order phase

transitions. Such cases were examined in [28], where the effect of a long-range Coulomb interaction on a second-order phase transition was studied.

In this chapter we use a combination of analytical and numerical techniques to analyze the role of doping. We explicitly solve the model given by Jamei, Kivelson and Spivak [1]. We show the spatial evolution of the order parameter, the spatial charge modulation and their corresponding energies. Here we investigate the case of linear coupling of the order parameter with the charge density. This is possible because the order parameter is a scalar. The thermodynamic potential, describing first order phase transition represents an η^4 model. The two minima represent two different phases. The charge is coupled to the order parameter as an external field.

3.2 Phase separation in cuprates

Since the discussion of phase separation is centered in the context of cuprates, we start by noticing the following facts. After the discovery of HTS in cuprates it was suggested independently by Zaanen-Gunnarsson [29], Emery-Kivelson [30, 31] and Gorkov-Sokol [32] the importance of charge separation. Later on the discussion in terms of lattice deformations was done by Alexandrov-Kabanov [33], Kusmartsev [34], Bishop-Shenoy-Lookman [35] and Jamei-Spivak-Kivelson [1]. More recently further studies were published by Castellani-Di Castro-Grilli [36], Mihailovic-Kabanov-Muller [37], Fine-Egami [27]. In these works the minimal conditions for the phase separation were set as well as a debate regarding phonon interaction as mechanism that can trigger the phase separation.

Models in which there is a coexistence of inhomogeneities and delocalized fermions as a precursor stage to the phase coherence and superconductivity have been developed [37]. Some of these models highlight the role of the stripe phase. The idea of antiferromagnetic-hole domains in high temperature superconductors was originally proposed for the $t-J$ model [38] where the role of spin interactions is underlined. The role of e-ph interactions was studied in [36]. In this respect Castellani et al.[36] proposed a Holstein-Hubbard model which takes into account lattice distortions as the trigger mechanism. However, these type of models have technical limitations. One of the disadvantage of the models, such as the t-J, the Hubbard or related microscopic models, is the large Hilbert space required to describe the phenomena. This is due to the several degrees of freedom (charge, spin and lattice) present. In order to simplify the problem, very often it is required to make some assumption regarding the energy scale which dominates the interactions. This may lead to calculations in a reduced Hilbert space.

The main advantage of the phenomenological description is that it is free of any microscopic details. Therefore we do not discuss strong electronic correlations and the different time and energy scales of the interactions. Another advantage is that we are not constrained to any temperature range. However, we believe that the long range Coulomb interaction is essential for charge segregation. Although the problem of introducing charge effects in phase separation is not new (besides the previous cited works see [39]), we will propose in chapter four a quadratic coupling of the order parameter to the charge density only explored in this doctoral thesis.

3.3 Free energy

It is expected that doping in a 2D system creates spatial charge segregation. Charges create an electric field that prevents growth of larger charged regions. In order to describe the charged regions we propose the following free energy density, $\widetilde{F}$, formed by the sum of the next four terms:

$$\widetilde{F} = \widetilde{F}_{pt} + \widetilde{F}_{coupl} + \widetilde{F}_{grad} + \widetilde{F}_{Coul}, \tag{3.1}$$

where

$$\widetilde{F}_{pt} = -\frac{\alpha}{2}\Lambda^2(\overrightarrow{r}) + \frac{\beta}{4}\Lambda^4(\overrightarrow{r}), \tag{3.2}$$

$$\widetilde{F}_{grad} = C(\nabla\Lambda(\overrightarrow{r}))^2, \tag{3.3}$$

$$\widetilde{F}_{Coul} = \frac{\widetilde{K}}{2}[\widetilde{\rho}(\vec{r}) - \widehat{\rho}]\int \frac{\widetilde{\rho}(\vec{r'}) - \widehat{\rho}}{|\vec{r} - \vec{r'}|}d\vec{r'}, \tag{3.4}$$

$$\widetilde{F}_{coupl} = -\widetilde{\lambda}(\widetilde{\rho}(\overrightarrow{r}) - \rho_C)\Lambda(\overrightarrow{r}). \tag{3.5}$$

Two minima given by the first term represents two different phases. We assume that $\alpha > 0$ and $\beta > 0$ are the coefficients in the Landau expansion. The second term is the gradient term and the constant $C > 0$ guaranties the stability of the system. This is due to the fact that if $C < 0$, the system may present large spatial fluctuations. The third term describes the Coulomb energy. The local charge density, $\widetilde{\rho}(r)$, fluctuates around the average charge density $\widehat{\rho}$. The last term describes the coupling of the order parameter

to the charge density. The interplay between F_{pt} and F_{coupl} leads to a first order phase transition. Here the charge plays the role of an external field since it is coupled linearly to the order parameter. The average charge density is defined as:

$$\widehat{\rho} = \frac{1}{V}\int \rho d\overrightarrow{r}, \tag{3.6}$$

where V is the volume where the charges are distributed and ρ_C is the critical charge density which onsets the coupling between the order parameter and charge density. Let us define the normalized order parameter, $\Lambda = (\alpha/\beta)^{1/2}\eta$. Therefore, $\widetilde{F} = U_0 F$ (see Appendix B)

where,

$$F = F_{pt} + F_{coupl} + F_{grad} + F_{el}, \tag{3.7}$$

and

$$F_{pt} = (\eta^2(\overrightarrow{r}) - 1)^2, \tag{3.8}$$

$$F_{grad} = (\nabla\eta(\overrightarrow{r}))^2, \tag{3.9}$$

$$F_{Coul} = \frac{K}{2}[\rho(\vec{r}) - \bar{\rho}]\int \frac{\rho(\vec{r'}) - \bar{\rho}}{|\vec{r} - \vec{r'}|} d\overrightarrow{r'}, \tag{3.10}$$

$$F_{coupl} = -\lambda(\rho(\overrightarrow{r}) - 1)\eta(\overrightarrow{r}), \tag{3.11}$$

The definition of the new constants are the following:

$$U_O = \frac{\alpha^2}{4\beta}, \tag{3.12}$$

$$K = \frac{4\rho_C^2\beta\xi\widetilde{K}}{\alpha^2}, \tag{3.13}$$

$$\lambda = \frac{4\rho_c\beta^{1/2}\widetilde{\lambda}}{\alpha^{3/2}}, \tag{3.14}$$

$$\xi = \sqrt{\frac{4C}{\alpha}}. \tag{3.15}$$

The energy barrier between the two minima in the double well potential is defined as U_0. The distances is measured in units of the coherence length $\overrightarrow{r} = \xi \overrightarrow{x}$. It will play an important role when we will study the finite size effects. A normalized local charge density, $\rho = \widetilde{\rho}/\rho_C$, and a normalized average density, $\overline{\rho} = \frac{\widehat{\rho}}{\rho_C}$, were also introduced. Here ρ and $\overline{\rho}$ are 3D charge densities. The factor K defines the ratio of the Coulomb energy and the condensation energy for the new phase.

The minimal energy for specific spatial arrangements of the order parameter can be obtained by minimization of the equation 3.7. Minimization over $\rho(\vec{r'})$ gives

$$-\lambda \nabla^2_{3D} \eta(\overrightarrow{r}) = 4\pi(\rho(\overrightarrow{r}) - \rho)\delta(z)d. \tag{3.16}$$

Explicitly it has been written that the electrostatic field is 3D, but the charge density is confined to a plane (z = 0). The finite thickness is defined by d, ρ is a 3D density and ρd is a 2D charge density. In the next section we solve Eq. (3.16) by means of Fourier transform. We will get an expression that when is substituting back into the free energy, we obtain:

$$\int F d\vec{r} = \int [F_{pt} + F_{grad} - \frac{\lambda^2}{8\pi^2 K d} \int \frac{\nabla\eta(\overrightarrow{r}) \cdot \nabla'\eta(\overrightarrow{r}')}{|\overrightarrow{r} - \overrightarrow{r}'|} d\overrightarrow{r}' - \lambda(\overline{\rho} - 1)\eta(\overrightarrow{r})] d\overrightarrow{r}. \tag{3.17}$$

In order to obtain the optimal charge configurations, we need to find the minimum in the free energy, $F(\eta(\overrightarrow{r}), \rho(\overrightarrow{r}))$, when $\rho(\overrightarrow{r})$ and $\eta(\overrightarrow{r})$ are allowed to change. We use an analytical minimization for $\rho(\overrightarrow{r})$ and once we have $F(\eta(\overrightarrow{r}))$ a numerical minimization for $\eta(\overrightarrow{r})$.

3.4 Analytical treatment in the momentum-space

Minimizing the total free energy over $\rho(\overrightarrow{r})$,

$$\frac{\delta \int F d\overrightarrow{r}}{\delta\rho} = -\lambda\eta(\overrightarrow{r}) + K \int \frac{(\rho(\overrightarrow{r}') - \overline{\rho}) d\overrightarrow{r}'}{|\overrightarrow{r}' - \overrightarrow{r}|} = 0, \tag{3.18}$$

then,

$$\eta(\overrightarrow{r}) = \frac{K}{\lambda}\int \frac{(\rho(\overrightarrow{r}\,') - \overline{\rho})d\overrightarrow{r}\,'}{|\overrightarrow{r}\,' - \overrightarrow{r}|}. \tag{3.19}$$

Applying the Laplace operator on both sides and using the 3D well known identity,

$$\nabla^2 \frac{1}{|\vec{r} - \vec{r}'|} = -4\pi\delta(\vec{r} - \vec{r}'), \tag{3.20}$$

$$\nabla^2_{3D}\eta(\overrightarrow{r}) = \frac{K}{\lambda}\int \nabla^2_{3D}\frac{1}{|\overrightarrow{r}\,' - \overrightarrow{r}|}(\rho(\overrightarrow{r}\,') - \overline{\rho})d\overrightarrow{r}\,' = -4\pi\frac{K}{\lambda}\int(\rho(\overrightarrow{r}\,') - \overline{\rho})\delta(\overrightarrow{r} - \overrightarrow{r}\,')d\overrightarrow{r}\,'. \tag{3.21}$$

we obtain,

$$\nabla^2_{3D}\eta(\overrightarrow{r}) = \frac{-4\pi K d}{\lambda}[\rho(\overrightarrow{r}) - \overline{\rho}]\delta(z), \tag{3.22}$$

where we use the fact that the charge density is distributed on a plane of a finite thickness d.

Applying Fourier transformation we solve the problem in k space. The next relation in momentum space holds for $\eta(\overrightarrow{r})$,

$$\eta(\overrightarrow{r}) = \frac{1}{(2\pi)^3}\int \eta(\overrightarrow{k})e^{-i\overrightarrow{k}\cdot\overrightarrow{r}}d\overrightarrow{k}. \tag{3.23}$$

$$\nabla^2_{3D}\eta(\overrightarrow{r}) = -\frac{1}{(2\pi)^3}\int |k|^2\eta(\overrightarrow{k})e^{-i\overrightarrow{k}\cdot\overrightarrow{r}}d\overrightarrow{k}. \tag{3.24}$$

We need to take into account that in Eq. (3.22) the charge density $\rho(\overrightarrow{r})$ has a 2D dependence, $\rho(\overrightarrow{r}) \equiv \rho(x, y)$, and z dependence is due to $\delta(z)$. Then, since the Fourier transform for these delta function is $\int \delta(z)e^{ik_z z}dz = 1$, after Fourier transforming Eq. (3.22) becomes,

$$\lambda(k^2 + k_z^2)\eta(\overrightarrow{k}) = 4\pi K d(\rho(\vec{k}) - \bar{\rho})d, \tag{3.25}$$

where the momentum was decomposed into a z component given by k_z. The momentum parallel to the plane will be denoted $\overrightarrow{k}$ and d is kept as the finite thickness of the plane. Next, we obtain the solution of the order parameter on the plane, $\eta(\overrightarrow{k})_{z=0}$,

$$\eta(\overrightarrow{k})_{z=0} = \frac{2dK}{\lambda}\int \frac{\rho(\overrightarrow{k}) - \overline{\rho}}{k^2 + k_z^2} dk_z. \tag{3.26}$$

Next, we use

$$\int \frac{dk_z}{k_z^2 + k^2} = \frac{\pi}{|k|}. \tag{3.27}$$

Therefore,

$$\eta(\overrightarrow{k}) = \frac{2\pi Kd}{\lambda}\frac{[\rho(\overrightarrow{k}) - \overline{\rho}]}{k} \tag{3.28}$$

and,

$$\rho(\overrightarrow{k}) - \overline{\rho} = \frac{\lambda k \eta(\overrightarrow{k})}{2\pi Kd}. \tag{3.29}$$

Now we transform back to real space the last expression. By means of

$$\eta(\overrightarrow{k}) = \int \eta(\overrightarrow{r}) e^{i\overrightarrow{k}\cdot\overrightarrow{r}} d\overrightarrow{r}, \tag{3.30}$$

we obtain,

$$\rho(\overrightarrow{r}) - \overline{\rho} = \frac{\lambda}{(2\pi)^3 Kd}\int \eta(\overrightarrow{r}\prime) d\overrightarrow{r}\prime \int k e^{i\overrightarrow{k}\cdot(\overrightarrow{r}-\overrightarrow{r}\prime)} d\overrightarrow{k}. \tag{3.31}$$

From here,

$$\rho(\overrightarrow{r}) - \overline{\rho} = -\frac{\lambda}{(2\pi)^3 Kd}\nabla^2 \int \eta(\overrightarrow{r}\prime) d\overrightarrow{r}\prime \int \frac{e^{i\overrightarrow{k}\cdot(\overrightarrow{r}-\overrightarrow{r}\prime)}}{k} d\overrightarrow{k}. \tag{3.32}$$

We define $\overrightarrow{R} = \overrightarrow{r} - \overrightarrow{r}\prime$ and after using the following relations

$$\int \frac{e^{i\overrightarrow{k}\cdot(\overrightarrow{r}-\overrightarrow{r}\prime)}}{k} d\overrightarrow{k} = \int \frac{e^{i\overrightarrow{k}\cdot\overrightarrow{R}}}{k} k dk d\theta = \int e^{ikR\cos\theta} d\theta dk = 2\pi \int_0^\infty J_0(kR) dk = \frac{2\pi}{|R|} \tag{3.33}$$

where $J_0(x)$ is a Bessel function. Thereby we get

$$\rho(\overrightarrow{r}) - \overline{\rho} = -\frac{\lambda}{(2\pi)^2 Kd}\nabla^2 \int \frac{\eta(\overrightarrow{r}')}{|\overrightarrow{r} - \overrightarrow{r}'|} d\overrightarrow{r}' = -\frac{\lambda}{(2\pi)^2 Kd}\int \eta(\overrightarrow{r}')\nabla^2 \frac{1}{|\overrightarrow{r} - \overrightarrow{r}'|} d\overrightarrow{r}'. \tag{3.34}$$

After a change of variable , $\overrightarrow{r} \to \overrightarrow{r}'$,

$$\nabla^2 \frac{1}{|\overrightarrow{r} - \overrightarrow{r}'|} = \nabla'^2 \frac{1}{|\overrightarrow{r} - \overrightarrow{r}'|}. \tag{3.35}$$

then,

$$\rho(\overrightarrow{r}) - \overline{\rho} = \frac{\lambda}{4\pi^2 Kd}\int \eta(\overrightarrow{r}')\nabla'^2 \frac{1}{|\overrightarrow{r} - \overrightarrow{r}'|} d\overrightarrow{r}'. \tag{3.36}$$

By the virtue of the divergent theorem,

$$\int \nabla'[\eta(\overrightarrow{r}')\nabla' \frac{1}{|\overrightarrow{r} - \overrightarrow{r}'|}] d\overrightarrow{r}' = \int [\nabla'\eta(\overrightarrow{r}')\nabla' \frac{1}{|\overrightarrow{r} - \overrightarrow{r}'|} + \eta(\overrightarrow{r}')\nabla'^2 \frac{1}{|\overrightarrow{r} - \overrightarrow{r}'|}] d\overrightarrow{r}' = 0. \tag{3.37}$$

Therefore,

$$\int \eta(\overrightarrow{r}')\nabla'^2 \frac{1}{|\overrightarrow{r} - \overrightarrow{r}'|} d\overrightarrow{r}' = -\int \nabla'\eta(\overrightarrow{r}')\nabla' \frac{1}{|\overrightarrow{r} - \overrightarrow{r}'|} d\overrightarrow{r}'. \tag{3.38}$$

Similarly we obtain,

$$\int \nabla'\eta(\overrightarrow{r}')\nabla' \frac{1}{|\overrightarrow{r} - \overrightarrow{r}'|} d\overrightarrow{r}' = -\int \frac{\nabla'^2\eta(\overrightarrow{r}')}{|\overrightarrow{r} - \overrightarrow{r}'|} d\overrightarrow{r}'. \tag{3.39}$$

In this way the local fluctuation of the charge density respect to the average charge density is:

$$\rho(\overrightarrow{r}) - \overline{\rho} = -\frac{\lambda}{4Kd\pi^2}\int \frac{\nabla'^2\eta(\overrightarrow{r}')}{|\overrightarrow{r} - \overrightarrow{r}'|} d\overrightarrow{r}' \tag{3.40}$$

On the other hand, we have for the coupling term, Eq. (3.11),

$$F_{coupl} = -\lambda(\rho(\overrightarrow{r}) - 1)\eta(\overrightarrow{r}) = -\frac{\lambda}{4Kd\pi^2}(\rho(\overrightarrow{r}) - \overline{\rho})\eta(\overrightarrow{r}) - \lambda(\overline{\rho} - 1)\eta(\overrightarrow{r}), \tag{3.41}$$

while for F_{Coul}, Eq. (3.10), using Eq. 3.19 we obtain:

$$F_{Coul} = \frac{K}{2}[\rho(\vec{r}) - \bar{\rho}] \int \frac{\rho(\vec{r'}) - \bar{\rho}}{|\vec{r} - \vec{r'}|} d\vec{r'} = \frac{\lambda}{2}(\rho(\overrightarrow{r}) - \overline{\rho})\eta(\overrightarrow{r}). \tag{3.42}$$

Therefore

$$F_{coupl} + F_{Coul} = -\frac{\lambda}{2}(\rho(\overrightarrow{r}) - \overline{\rho})\eta(\overrightarrow{r}) - \lambda(\overline{\rho} - 1)\eta(\overrightarrow{r}). \tag{3.43}$$

Applying Eq. (3.40)

$$F_{Coul} + F_{coupl} = -\frac{\lambda^2}{Kd8\pi^2} \int \eta(\overrightarrow{r}) \frac{\nabla'^2 \eta(\overrightarrow{r}')}{|\overrightarrow{r} - \overrightarrow{r}'|} d\overrightarrow{r}' - \lambda(\overline{\rho} - 1)\eta(\overrightarrow{r}). \tag{3.44}$$

Equivalently, if we use the divergent theorem,

$$\int \frac{\nabla'^2 \eta(\overrightarrow{r}')\eta(\overrightarrow{r})}{|\overrightarrow{r} - \overrightarrow{r}'|} d\overrightarrow{r}' = -\int (\nabla' \eta(\overrightarrow{r}'))(\nabla' \frac{1}{|\overrightarrow{r} - \overrightarrow{r}'|})\eta(\overrightarrow{r}) d\overrightarrow{r}' = \int (\nabla' \eta(\overrightarrow{r}'))(\nabla \frac{1}{|\overrightarrow{r} - \overrightarrow{r}'|})\eta(\overrightarrow{r}) d\overrightarrow{r}'. \tag{3.45}$$

In the last step we made a change of variable $r \to r'$ in order to transform $\nabla' \to \nabla$. Similarly,

$$\int (\nabla' \eta(\overrightarrow{r}'))(\nabla \frac{1}{|\overrightarrow{r} - \overrightarrow{r}'|})\eta(\overrightarrow{r}) d\overrightarrow{r}\, d\overrightarrow{r}' = -\int (\nabla' \eta(\overrightarrow{r}')) \frac{1}{|\overrightarrow{r} - \overrightarrow{r}'|} \nabla \eta(\overrightarrow{r}) d\overrightarrow{r}' d\overrightarrow{r}. \tag{3.46}$$

Thus,

$$\int \nabla \eta(\overrightarrow{r}) \nabla' \frac{1}{|\overrightarrow{r} - \overrightarrow{r}'|} \eta(\overrightarrow{r}) d\overrightarrow{r}' d\overrightarrow{r} = \int \frac{\nabla' \eta(\overrightarrow{r}') \cdot \nabla \eta(\overrightarrow{r})}{|\overrightarrow{r} - \overrightarrow{r}'|} d\overrightarrow{r}' d\overrightarrow{r}. \tag{3.47}$$

We have to bear in mind that the free energy is $\int (F_{Coul} + F_{coupl}) d\overrightarrow{r}$, so

$$\int (F_{Coul} + F_{coupl}) d\overrightarrow{r} = \int [-\frac{\lambda'^2}{Kd8\pi^2} \int \frac{\nabla' \eta(\overrightarrow{r}') \cdot \nabla \eta(\overrightarrow{r})}{|\overrightarrow{r} - \overrightarrow{r}'|} d\overrightarrow{r}' - \lambda(\overline{\rho} - 1)\eta(\overrightarrow{r})] d\overrightarrow{r}. \tag{3.48}$$

Therefore the total free energy is given by

$$\int F d\overrightarrow{r} = \int [F_{pt} + F_{grad} - \frac{\lambda^2}{8\pi^2 K d} \int \frac{\nabla\eta(\overrightarrow{r}) \cdot \nabla'\eta(\overrightarrow{r'})}{|\overrightarrow{r} - \overrightarrow{r}'|} d\overrightarrow{r}' - \lambda(\overline{\rho} - 1)\eta(\overrightarrow{r})] d\overrightarrow{r}. \quad (3.49)$$

Note that the nonlocal gradient term is negative and is similar to Lifshits invariants leading to instabilities of the homogeneous state. In addition, the appearance of the last term acts like an constant external field n_{av}:

$$n_{av} = -\lambda(\overline{\rho} - 1). \quad (3.50)$$

We point out that

$$a = \frac{\lambda^2}{8\pi^2 K d}, \quad (3.51)$$

measures the strength of the coupling. Moreover, due to the fact that it is the coefficient of the a long range term with gradient operators for $\eta(\overrightarrow{r})$, it also controls the degree of frustration.

3.5 Numerical minimization of the free energy

In order to minimize the dimensionless free energy $\int F d\overrightarrow{r}$, we use the conjugated gradient method CGM (Appendix A). We introduce Nx$N(N = 128)$ discrete points on a square of length L (the length is measured in units of ξ). Since we expect that minimization of the free energy is realized on a periodic structure, we apply periodic boundary conditions. To eliminate the role of the incommensurability, we have studied the energy for different sizes of the system. For fixed length, L, the free energy depends on two parameters: $n_{av} = \lambda(\overline{\rho} - 1)$ and $a = \lambda^2/8\pi K d$. The last parameter is also identified as the degree of frustration on the system. As a result, the problem has been reduced to two free parameters and the minimization of the free energy as a function of $\eta(\overrightarrow{r})$. Henceforth we refer in our calculations to the energy E defined by:

$$E = \frac{\int F d\overrightarrow{x}}{U_o \xi^2}. \quad (3.52)$$

We start by computing patterns and the free energy for $a = 0.8$. A detailed discussion for wider ranges of doping and different values of a will be shown afterwards. Because we confine the system in the LxL area, it is important to analyze the finite size effect.

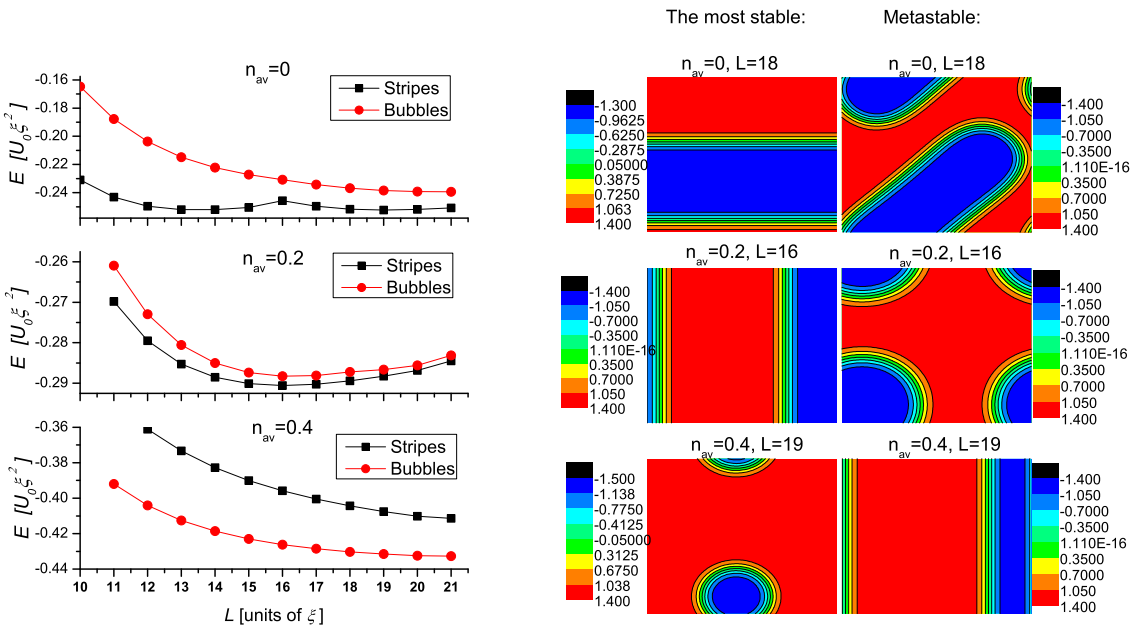

(a) (b)

FIGURE 3.1: (a) Crossover from stripes to bubbles for $a = 0.8$. At $n_{av} = 0$ the stripes structure presents the minimum of the free energy. The commensurate-incommensurate effect is seen as the size of the system is increased. At $n_{av} = 0.2$ bubbles and stripes are very close in energy. At higher doping, $n_{av} = 0.4$, bubbles are the most stable pattern, while stripes become meta-stable. (b) Order parameter distribution, $\eta(r)$, at different n_{av}.

Figure 3.1 shows the result of the minimization of the free energy. Phase separation in the form of bubbles or stripes is obtained. Stripes and bubble shapes are the two competing patterns with different orientations depending on the length L. For the set of parameters chosen for figure 3.1, at $n_{av} = 0$ the stripe pattern presents the lowest energy state. Stripes have minimum energies at $L = 13, 18$. The stripe pattern with the lowest energies is shown in fig. 3.1 b. together with the bubble configuration which represents the metastable phase. Bubbles present similar behavior, crossing from perfect rounded shapes for the minimum energies to elongated bubble shapes for the maximum energies. However in the case of bubbles, we did not observe periodic dependence of the energy as a function of L as in the case of stripes at this doping. The increase of doping to $n_{av} = 0.2$ also reduces the energy difference between these configurations. Both patterns present their minimum energy at $L = 16$. With increase of the doping the bubbles become the most stable configuration. Here the stripes and bubbles energies converge to a constant as L is increased, but always the bubbles present the lowest energy. Figure 3.2 shows the way the order parameter and the charge density are linked (see Eq. 3.40). It corresponds to a cross section of one single stripe. It is observed that the charge density tends to follow the patterns formed by the order parameter, but most

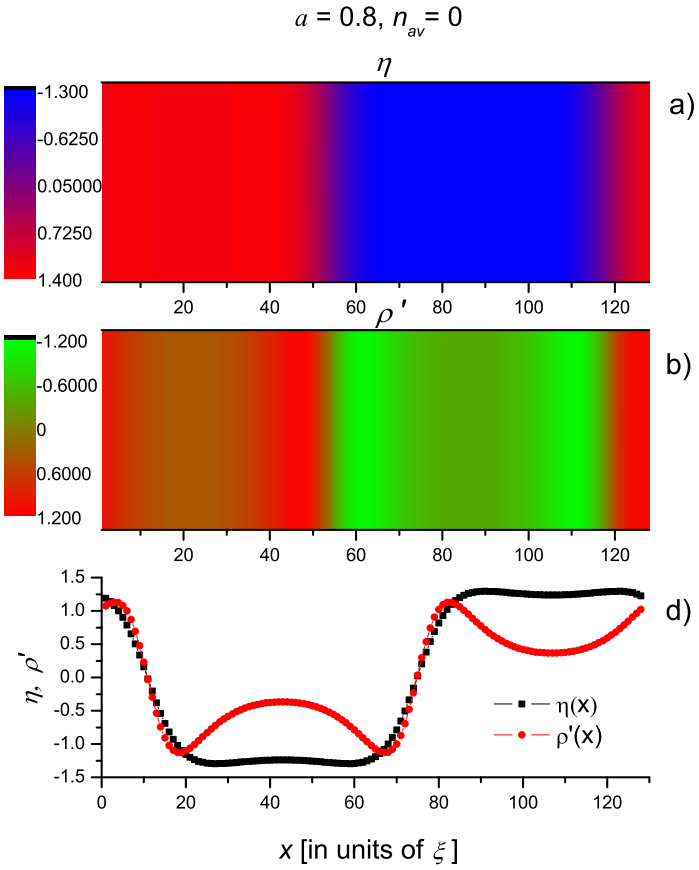

FIGURE 3.2: a) variation of the order parameter $\eta(x, y = const.)$ (black curve in panel c). b) variation of local charge density defined by $\rho' = \rho(x, y = const.) - \overline{\rho}$ (red curve in panel c). The set of parameters used are: $a = 0.8$, $n_{av} = 0$ and $L = 18$.

of the charge density is concentrated in the border of these patterns. This leads to the formation of charged domain walls.

Figure 3.3 shows the free energy of the most stable configurations for $a = 1$ in a broad range of doping. Stripes are dominant at low and intermediate doping while bubbles dominate the phase diagram at high doping. For $0 \leq n_{av} \leq 0.4$ stripes display a periodic dependence of energy as a function of L. At $n_{av} = 0.4$, bubbles also show periodic dependence of energy on L. As in the case of stripes, this effect is due to the incommensurability of bubbles confined in a 2D area of size LxL area. Rather interestingly, both patterns not only follow similar periodicity but they also have similar energy. From here we can conclude that at $n_{av} = 0.4$ stripes and bubbles fully compete for the most stable configuration. So this doping onsets the transition to the bubble phase. The bubble phase remains stable up to $n_{av} \approx 0.8$. Further increase of doping leads to an homogenous phase, with the order parameter uniformly distributed across the plane.

Similarly, the phase transition can be investigated as function of a for fixed doping. For selected values of a and $n_{av} = 0$ we observe in figure 3.4 that stripes remain as the most

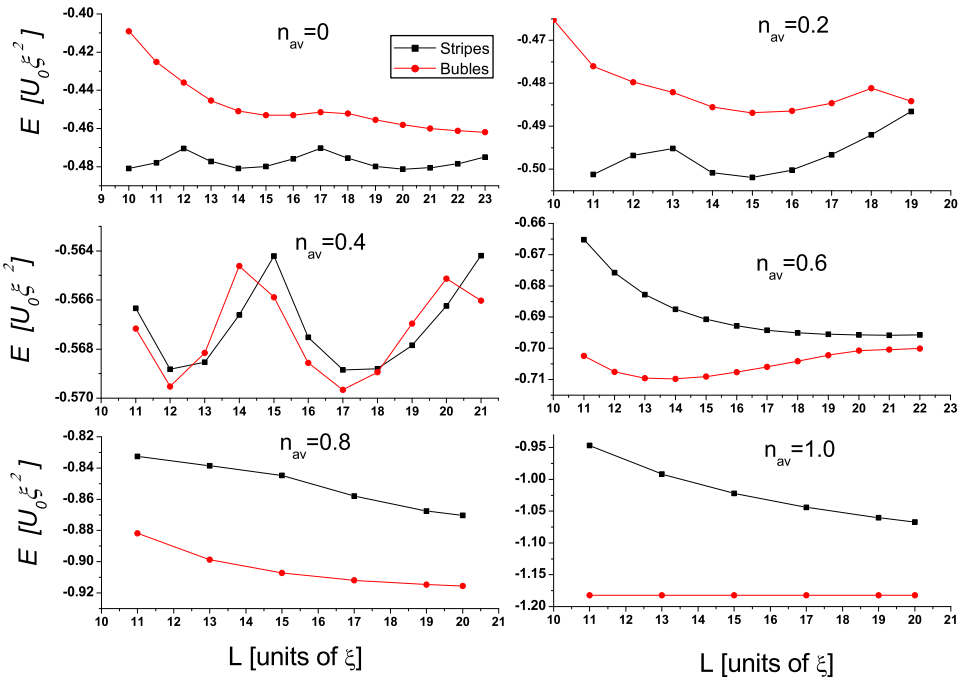

FIGURE 3.3: Stripe-bubble crossovers driven by doping. We set doping from $n_{av} = 0$ to $n_{av} = 1.0$; in all cases $a = 1$. For the lower two dopings, the stripe phase has the lowest energy. At doping $n_{av} = 0.4$, the transition to the bubble phase starts. Bubbles have the most stable phase above $n_{av} = 0.4$. The figure shows that bubbles dominate the regime of $n_{nav} = 0.6$. Further increase of doping, $n_{av} = 1$, leads to the homogenous state. The patterns and the homogeneous phase were assigned from the order parameter distribution (not shown).

stable phase. For this set of parameters the stripes can be orientated diagonally of horizontally (vertically) depending on a. Similarly, bubbles may be arranged symmetrically or with elongated patterns orientated diagonally or along the x or y axis directions, but always being as metastable patterns. Nevertheless, for $a < 0.4$, bubbles become energetically favorable (not shown).

The sizes of stripes are modified with doping. Figure 3.5 shows the variations of the order parameter for a cross section of a single stripe. Here the perfect periodicity of the stripe arrangement is observed. We can conclude from this figure that the stripe width is sensitive to the level of doping: the higher the doping the wider the stripes.

The last set of parameters is for the case of stronger frustration: $a = 1.4$ with $n_{av} = 0.6$. As we can notice in figure 3.6, stripes are still dominating this regime. Bubbles are formed with higher free energies, but they are not the closest metastable phase to stripes. We observe that another type of charge density structure has been developed just below the bubble energy curve. Such structure is formed by two types of charged clusters with rounded shapes. The energy of these new kind of patterns shows a dependence as a function of L. Another important feature is that stripes and bubbles present a

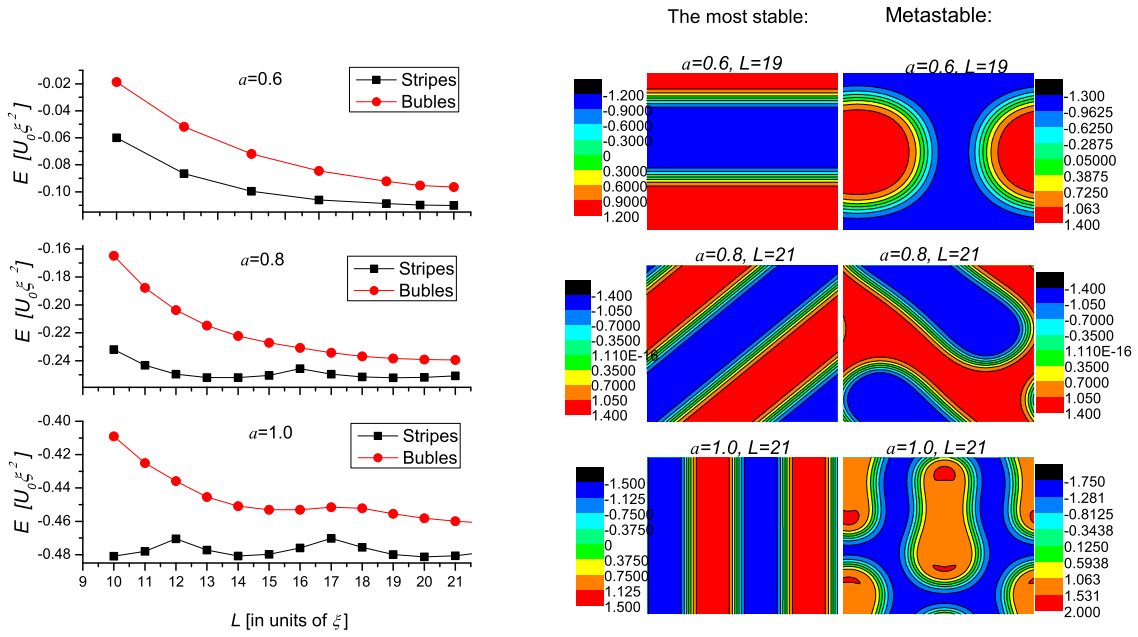

(a) (b)

FIGURE 3.4: (a) Free energy for three values of a when the doping is fixed to $n_{av} = 0$. For this range of a stripes are the most stable phase. (b) Order parameter distribution corresponding to fig (a). The most stable configurations are always stripes.

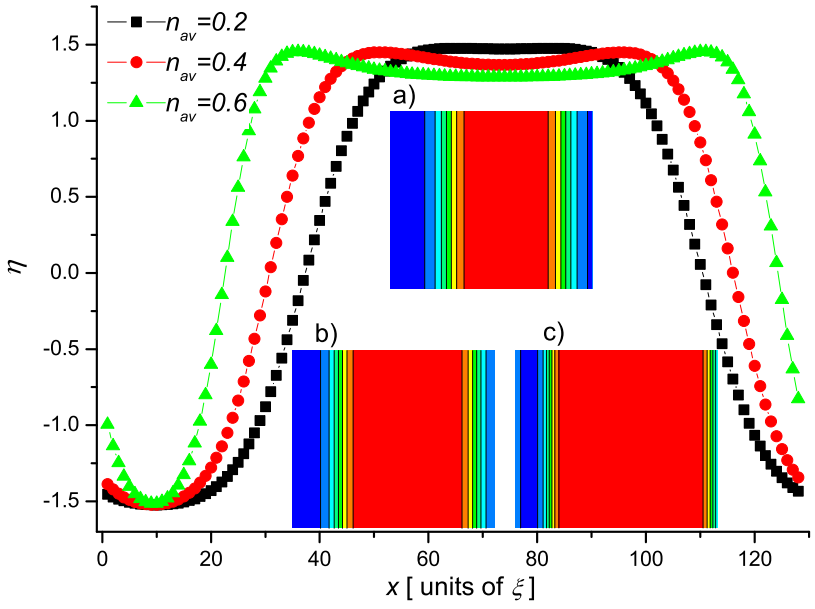

FIGURE 3.5: Spatial dependence of the order parameter perpendicular to stripe. Insets: a) $n_{av} = 0.2$, b) $n_{av} = 0.4$ and c) $n_{av} = 0.6$. The chosen stripes correspond to $L = 10, 12$, and $L = 18$ for a), b) and c) respectively.

shorter period and they are restricted within smaller charged regions. According to our numerical solution for $n_{av} < 0.6$ and $a > 1.4$ complex patterns dominate this range of a.

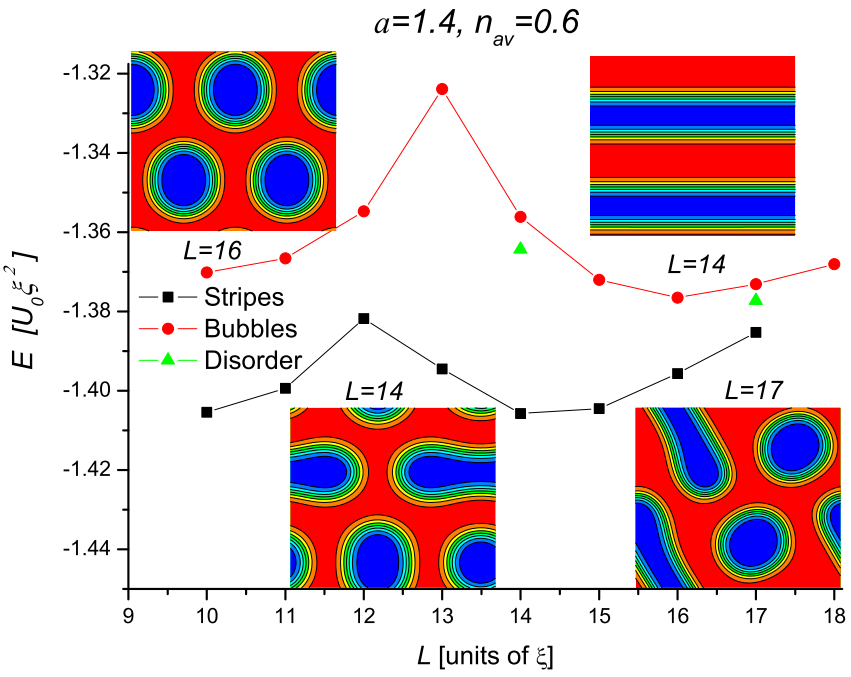

FIGURE 3.6: New type of charged clusters are developed as a is increased. These structures start to compete against stripes and bubbles. We observe that bubbles are no longer the metastable phase closer in energy to stripes. The two insets at the bottom are the emergent patterns given by the order parameter. Their corresponding energies are given by the two green points. Top insets are the lowest energy configuration for stipes and bubbles.

3.5.1 Phase diagram

Before moving on the discussion of the phase diagram a vs n_{av} we explain the symmetry between positive (n_{av}^{+}) and negative doping (n_{av}^{-}). The Figure 3.7 depicts order parameter distributions and energies for $n_{av}^{+} = 0.2$ and $n_{av}^{-} = -0.2$. It is seen that at both doping the same shapes develop, but the order parameter regions, $\eta(\overrightarrow{r})$, are inverted. So n_{av}^{+} is the symmetric image respect to n_{av}^{+}. This symmetry is due to the simple fact that the charge density is coupled with the order parameter linearly therefore simultaneous change $(\rho(\mathbf{r}) - \rho_c) \to -(\rho(\mathbf{r}) - \rho_c)$ and $\eta(\overrightarrow{r}) \longrightarrow -\eta(\overrightarrow{r})$ do not change the free energy.

In our model doping acts as an external field (see Eq. 3.50). Here the strength of the external field is given by the level of doing n_{av} which allows to favor certain values of $\eta(\mathbf{r})$. For instance, values near $\eta(\mathbf{r}) = 1$ (see figure 3.8) are favored by $n_{av} < 0$ in the phase transition described by

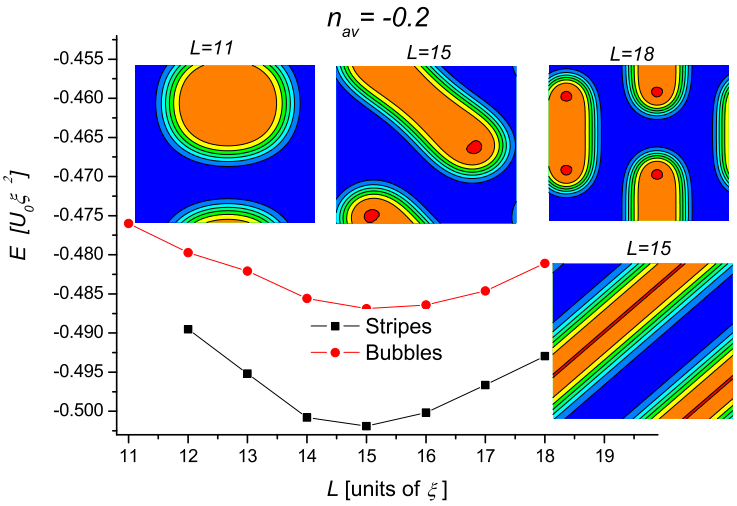

(a) Cluster, made by negative regions of the order parameter(yellow), are surrounded by a positive values of the order parameter (blue).

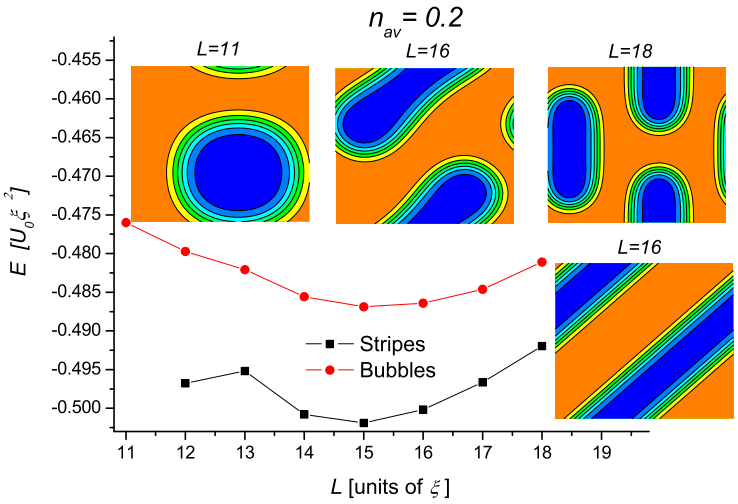

(b) Cluster, made by positive regions of the order parameter (blue), are surrounded by negative values of the order parameter (yellow).

FIGURE 3.7: Symmetry in order parameter distribution between $n_{av} = 0.2$ and $n_{av} = -0.2$ when $a = 0.4$. The energy curves follow practically the same values.

$$F = (\eta(\mathbf{r}) - 1)^2 + n_{av}\eta(\mathbf{r}). \tag{3.53}$$

The phase diagram a vs n_{av} is shown in figure 3.9. In the top and bottom part of the phase diagram, the homogeneous phase dominates. According to our previous discussion, the order parameter found in these two regions are of different nature. The top region is a uniform distribution of the $\eta(\overrightarrow{r})$ originated from doping $n_{av}^{(1)} \geq 0$, while the bottom region belongs to the uniform distribution of $\eta(\overrightarrow{r})$ originated from $n_{av}^{(2)} < 0$; we labeled them as Homogeneous1 and Homogeneous2, respectively.

The second feature observed is that the two dominant type of patterns are within a triangular-like region. The stripe phase is in the inner area and around it we find the bubble phase. From here we can conclude that, for a given a, stripes are formed at lower doping than bubbles. As a and n_{av} are increased, the stripe phase occupies larger zones. The critical point at $n_{av} = 0$ and $a \approx 0.2$ onsets the formation of bubbles. A direct crossover from one type of homogeneous phase to the second type, without crossing the phase segregation region, occurs for $a < 0.2$. However, this threshold value may be due to finite size effects and the exact value of a may be shifted to zero. A second critical point at $n_{av} = 0$ and $a \approx 0.5$ onsets of the stripe phase. The stripe phase is stable up to $a \approx 1.4$.

Nevertheless, stripes are not present beyond $a > 1.4$ as a stable phase. In fact, they are not the only patterns with the lowest energy. Using the same set of parameters, other patterns with the same or nearly same energy are formed. Further increase of a leads to patterns such as those shown in figure 3.10. Here we enter into the "glass" region. In order to define this region we take as criteria the number of equivalent configurations with the same energy found by the CGM. Thus, we designate this phase when the number of minima, with distinctive patterns, is higher than two. Indeed, the computational time involved during the CGM minimization strongly increases if compared with the calculation time in the low frustration regime. Since the free energy has many minimas separated by barriers the number of CGM steps is increased and as a consequence the search of global minimum consumes larger CPU time. This is also reflected in the fact that the minimum energy is sensitive to the initial configuration of the order parameter.

3.5.2 Inhomogeneities subject to disorder

Studies of frustrated phase separation caused by LRCI have shown that it can lead to a quenched disorder of charged structures[40]. Indeed, some studies have discussed the

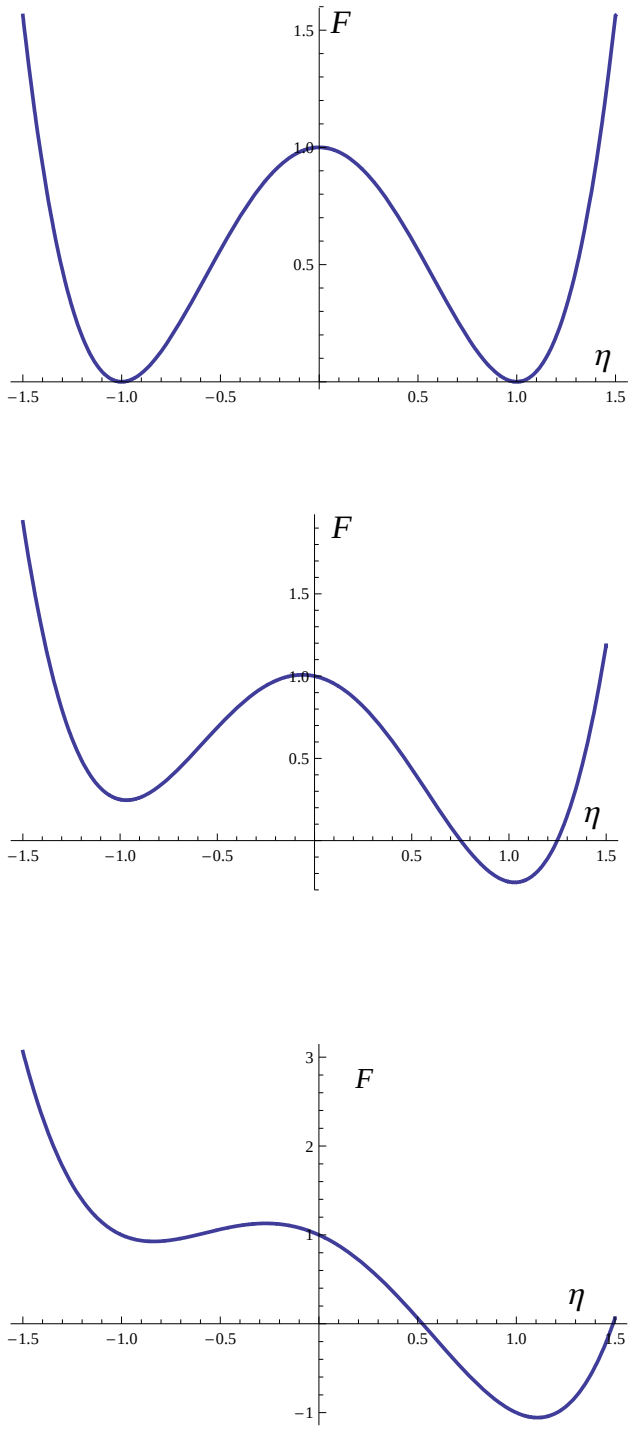

FIGURE 3.8: Free energy of a weak first order phase transition, $F = (\eta(\mathbf{r})-1)^2+n_{av}\eta(\mathbf{r})$ at fixed temperature $T < T_c$. The chosen fields are: $n_{av} = 0$ (top panel), $n_{av} = -0.25$ (middle panel) and $n_{av} = -0.75$ (bottom panel).

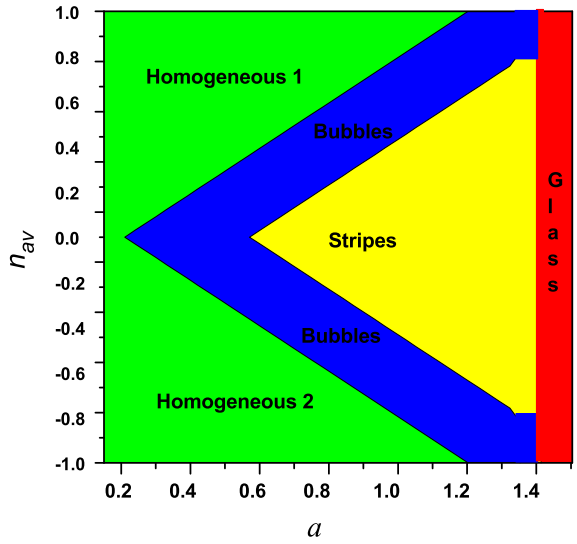

FIGURE 3.9: Schematic representation of the phase diagram a vs n_{av}. The phase separation can take the shape of bubble-like (blue region) or stripe-like (yellow region). Both patterns exist within two different homogeneous phases (green). At high degree of frustration, $a > 1.4$, a glass phase appears (red region).

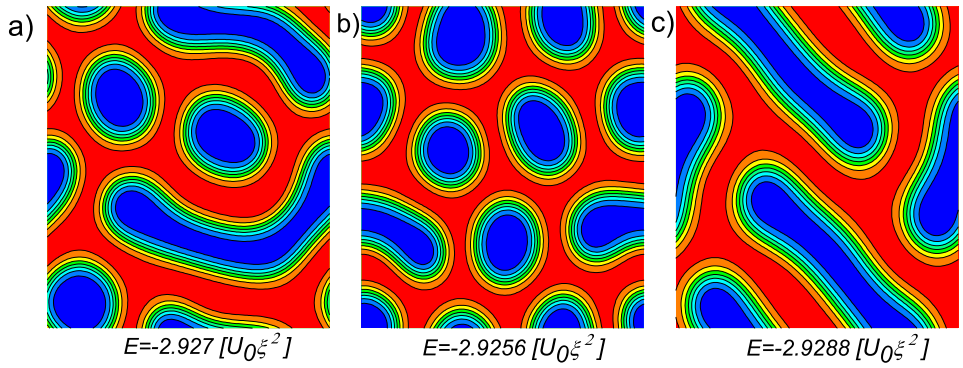

FIGURE 3.10: High values of a lead to the strongly frustrated regime. It is characterized by the emergence of complex domains whose energies are nearly the same. The figure shows three of such domains for $a = 1.8$, $n_{av} = 0.2$.

proximity of a glass phase and the stripe phase in doped antiferromagnets [41]. The addition of extrinsic disorder can modify further the nature of phase separation. Structural defects (point defects, dislocations) or impurities may be considered as the origin of such perturbations. These random variations enter into the microscopic variable σ defined in section 2.2. As a consequence the order parameter, $\eta(\mathbf{r})$, can be randomly modified across the plane. The usual way of introducing them is through a statistical distribution of local interactions which naturally leads to the so-called quenched disorder. It is widely used in the context of spin glasses, where magnetic impurities modify the exchange integrals. For instance in the Ising model, the interaction takes the form $\sum_{ij} J_{i,j} S_i S_j$, where the coupling J follows a specific statistical distribution for the problem in turn. However, perturbations on σ can introduce charge fluctuation, where the distribution of electronic densities follow the perturbation (poor or rich region of electrons). This may allow us to use the disorder as a control parameter to shift the subtle balance between two competitive states. For example a metal-insulator transition.

On the other hand, material scientists often face the problem of growing crystal structures. It is difficult to obtain a material free of defects during the process of synthesization. Therefore, it is of great importance to know the robustness of the inhomogeneities under the above conditions. It is desirable to have some insight when we are close or far from the "clean limit". This is the term coined when a material is perfectly periodic. Here we explore the consequences of having random charge distributions across the plane. We test the model by means of two set of parameters: $a = 0.8$, $n_{av} = 0$ and $a = 0.8$, $n_{av} = 0.8$.

Within the framework of Landau transitions the free energy density which describes the inhomogeneous phase subject to random variations of $\eta(\overrightarrow{r})$ is

$$F = F_{pt} + F_{coupl} + F_{grad} + F_{el} + F_r, \tag{3.54}$$

where $F_r = W_r(\overrightarrow{r})\eta(\overrightarrow{r})$. W_r plays a role of random charge density. For instance it can follow the random distribution of impurities. It is defined within a box of width of W_d. Therefore, the last term represents the energy deviations created by impurities. Following exactly the same procedure as presented in section 3.5, we obtain

$$F = (\eta^2(\overrightarrow{r}) - 1)^2 + C\nabla\eta^2(\vec{r}) - \lambda(\overline{\rho} - 1)\eta(\overrightarrow{r}) - \frac{\lambda^2}{8\pi^2 K d}\int \frac{\nabla\eta(\overrightarrow{r})\nabla\eta(\overrightarrow{r'})}{|\overrightarrow{r} - \overrightarrow{r}'|}dr' + W_r(r)\eta(\overrightarrow{r}) \tag{3.55}$$

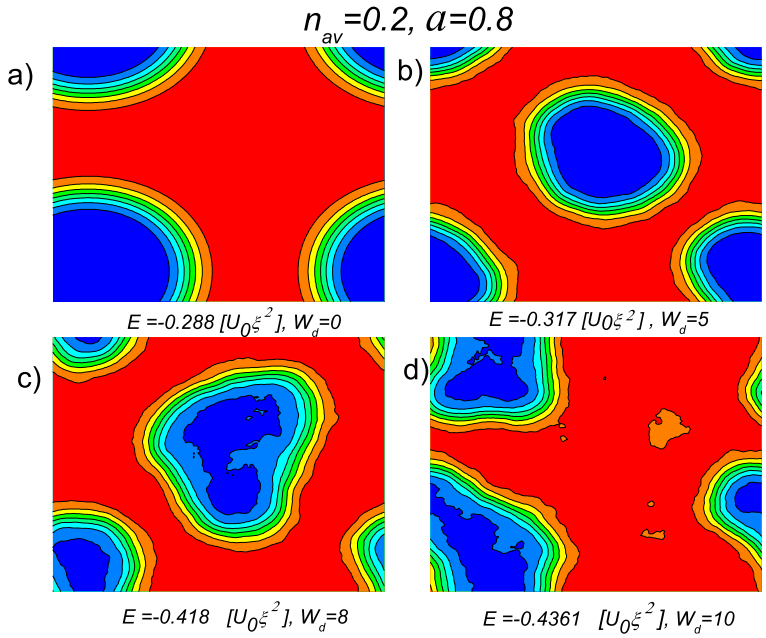

FIGURE 3.11: Bubbles subject to the random variation of charge density for $a = 0.8$ and $n_{av} = 0.2$. The level of randomness is measures by the parameter W_d.

The results of the the minimization by the CGM is shown in figures 3.11. The set of parameter was chosen as $a = 0.8$ and $n_{av} = 0.2$. We investigate how the bubbles behave as the level of randomness is increased. For values $W_d < 8$, the original shape of bubbles is preserved. This is a rather surprising result, given the fact that W_d is one order of magnitude larger than a. By contrast in the model presented in section 4.5.2 with quadratic coupling, we observe that for the similar a at $W_d = 1.5$ the bubble phase disappears. From here we can infer that the linear coupling is less sensitive to random distribution of charges.

Now we select a point in the phase diagram where stripes are the stable structure. Figure 3.12 shows the response of stripes as the disorder is increased. The analysis suggests that also the stripe phase is rather insensitive to the disorder. However, perhaps a more fundamental result is observed in the way the stripes are modified. Panels c) and d) in figure 3.11 show two modified stripes. We observe that the edges of stripes are in some regions closer, respect to each other, than in perfect aligned stripes (see for example 3.4c). This could of be great importance if the stipes represent metallic regions. The fact that stripes may induce alternative ways of charge conductivity has been predicted in percolative theories or in the context of quantum tunneling. Some models consider simultaneously two component: inner and intra stripes charge transport. Moreover, it has been discussed in literature whether thermal or quantum fluctuations are essential

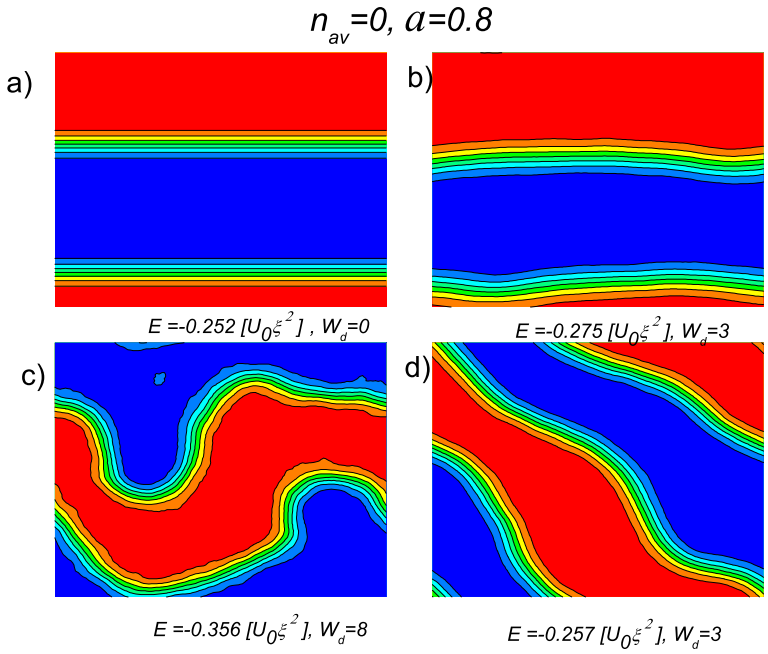

FIGURE 3.12: Stripes subject to the random events for $a = 0.8$ and $n_{av} = 0$. The level of randomness is measured by the parameter W_d.

in the conductivity of a phase separated system. In that sense, according to our results, structural disorder may facilitate charge transport across stripes, thereby conductivity could be either triggered or enhanced.

Further studies needs to be done in order to clarify whether the disorder can shift the most stable pattern (stripes shifted to bubbles or vice versa). Additional calculations are also required to establish whether such shape remain the same, or they are split into a larger number of smaller domains. For instance, this could explain the increase in the number of bubbles observed in figure 3.10b.

3.6 Conclusion

In this chapter we considered the problem of Coulomb frustrated first order phase transition separation with the scalar order parameter. We have shown that the Coulomb frustration leads to the formation of the charge modulated state between two homogeneous phases. As a function of doping we observe a sequence of crossovers from stripe phase to bubbles phase, before the homogeneous phase is achieved again. In addition

we showed that the the strength of the Coulomb interaction determines the charge distribution and characteristic size of the emerging inhomogeneous-phase regions.

Chapter 4

Coulomb frustrated first order phase transition. Non-scalar order parameter

4.1 Introduction

We continue the techniques given in chapter three. The first main modification we introduce, if compared with previous chapter, is the form the local charge density is coupled to the order parameter. In this chapter we use a quadratic coupling of the order parameter to the local charge density. This type of coupling will allow us to deal with the systems with degeneracy. In the second part of the thesis we will investigate a system where such type of coupling is realized. There, lattice instabilities arise due to the degeneracy of electronic levels.

4.2 Free energy

Upon doping and as the temperature is lowered the creation of a spatial charge segregation and mixture of different phases is expected. In order to describe the charged regions we propose the following total free energy density:

$$F = F_1 + F_{coupl} + F_{grad} + F_{Coul}, \tag{4.1}$$

where

$$F_1 = [(\tau' - 1) + (\eta^2(\vec{r}) - 1)^2]\eta^2(\overrightarrow{r}), \tag{4.2}$$

$$F_{grad} = C[\nabla\eta(\overrightarrow{r})]^2, \tag{4.3}$$

$$F_{Coul} = \frac{K}{2}[\rho(\vec{r}) - \bar{\rho}] \int \frac{\rho(\vec{r'}) - \bar{\rho}}{|\vec{r} - \vec{r'}|} d\vec{r'}, \tag{4.4}$$

$$F_{coupl} = -\lambda\eta^2(\overrightarrow{r})\rho(\overrightarrow{r}), \tag{4.5}$$

F_1 includes a negative fourth order term and a positive sixth order term to model a first order phase transition. Indeed it is the same potential we introduced in section 2.3.2 and represented by figures 2.2 and 2.3. Here $\tau' = (T - T_c)/(T_t - T_c)$ is the dimensionless temperature. At $\tau' = 3/4$ ($T = T_0 + (T_t - T_c)/3$)) a nontrivial minimum just appears ($\eta \neq 0$). At $\tau' = 1$ ($T = T_t$) the ordinary first order transition occurs, Below $\tau' = 1$ the trivial solution $\eta = 0$ corresponds to the a metastable state. At $\tau' = 0$ ($T = T_c$), the trivial solution becomes unstable. The second and third term are the gradient contribution and the Coulomb energy, respectively. We assume an isotropic layer, so the stiffness constant $C > 0$ is taken as a scalar. The last term describes the local coupling of the order parameter to the charge density, $\rho(r)$. Here the charge plays the role of the local temperature. K is the strength of the Coulomb repulsion and λ is the coupling constant between the order parameter and the charge density. We have taken into account the global neutrality through:

$$\bar{\rho} = \frac{1}{V} \int \rho(\overrightarrow{r}) d\overrightarrow{r}, \tag{4.6}$$

V is the volume where the charge is distributed. Here ρ is the 3D charge density and $\overline{\rho}$ is the 3D average charge density. Similar free energy densities have been discussed in martensitic transformations, where disorder or shear strains are the driving forces to new phases with mesoscopic modulations.

In order to obtain the optimal charge configurations, we need to find the minimum in the free energy, $F(\eta(\overrightarrow{r}), \rho(\overrightarrow{r}))$, when $\rho(\overrightarrow{r})$ and $\eta(\overrightarrow{r})$ are allowed to change. We use an analytical minimization for $\rho(\overrightarrow{r})$ and once we have $F(\eta(\overrightarrow{r}))$ a numerical minimization for $\eta(\overrightarrow{r})$. In the next section we show the treatment of the LRC potential as a full 3D problem. Afterward we focus on the 2D case. In this way the reader can make a clearer

distinction between both cases. The fact that charges are restricted to a layer will lead to crucial differences in the free energy $F(\eta(\overrightarrow{r}))$.

4.2.1 3D case

Minimizing with respect to ρ,

$$\frac{\delta \int F d\overrightarrow{r}}{\delta \rho} = -\lambda \eta^2(\vec{r}) + K \int \frac{(\rho(\vec{r}') - \bar{\rho})}{|\vec{r} - \vec{r}'|} d\overrightarrow{r}' = 0. \tag{4.7}$$

From here we get,

$$\eta^2(\vec{r}) = \frac{K}{\lambda} \int \frac{(\rho(\vec{r}') - \bar{\rho})}{|\vec{r} - \vec{r}'|} d\overrightarrow{r}'. \tag{4.8}$$

Applying the Laplace operator on both sides and using the 3D well known identity,

$$\nabla^2 \frac{1}{|\vec{r} - \vec{r'}|} = -4\pi\delta(\vec{r} - \vec{r}'), \tag{4.9}$$

we obtain,

$$-\lambda \nabla^2 \eta^2(\vec{r}) = 4K\pi(\rho(\vec{r}) - \bar{\rho}), \tag{4.10}$$

$$\rho(\vec{r}) = \overline{\rho} - \frac{\lambda}{4\pi K} \nabla^2 \eta^2(\vec{r}). \tag{4.11}$$

Therefore the coupling term can be written as,

$$F_{coupl} = -\lambda \eta^2(\overrightarrow{r}) \rho(\overrightarrow{r}) = -\lambda \overline{\rho} \eta^2(\vec{r}) + \frac{\lambda^2}{4\pi K} \eta^2(\overrightarrow{r}) \nabla^2 \eta^2(\vec{r}). \tag{4.12}$$

While for the LRCI we get,

$$F_{Coul} = \frac{K}{2}[\rho(\vec{r}) - \bar{\rho}] \int \frac{\rho(\vec{r'}) - \bar{\rho}}{|\vec{r} - \vec{r'}|} d\vec{r'} = -\frac{\lambda^2}{8K\pi} \eta^2(\vec{r}) \nabla^2 \eta^2(\vec{r}). \tag{4.13}$$

Thus the sum of the two interactions is

$$F_{coupl} + F_{Coul} = \frac{\lambda^2}{8K\pi}\eta^2(\vec{r})\nabla^2\eta^2(\vec{r}) - \lambda\overline{\rho}\eta^2(\vec{r}). \tag{4.14}$$

Next, we focus on the first term of the right part of equation 4.14. Since we are interested in the free energy, we take the integral $\int \eta^2(\vec{r})\nabla^2\eta^2(\vec{r})d\overrightarrow{r}$. So,

$$\eta^2(\overrightarrow{r})\nabla^2\eta^2(\vec{r}) = \nabla[\eta^2(\overrightarrow{r}) \cdot \nabla\eta^2(\overrightarrow{r})] - \nabla\eta^2(\overrightarrow{r})\nabla\eta^2(\overrightarrow{r}). \tag{4.15}$$

Taking into account

$$\int \nabla[\eta^2(\overrightarrow{r}) \cdot \nabla(\eta^2(\overrightarrow{r}))]d\overrightarrow{r} = \oint_s \vec{n}\eta^2\vec{\nabla}\eta(\vec{r})ds = 0, \tag{4.16}$$

we obtain,

$$\frac{\lambda^2}{8K\pi}\int \eta^2(\overrightarrow{r})\nabla^2\eta^2(\vec{r})d\overrightarrow{r} = -\frac{\lambda^2}{8K\pi}\int (\nabla^2\eta^2(\vec{r}))^2 d^3r. \tag{4.17}$$

In this way the free energy density is

$$F = F_1 + F_{grad} - \lambda\overline{\rho}\eta^2(\vec{r}) - \frac{\lambda^2}{8K\pi}(\nabla\eta^2(\vec{r}))^2. \tag{4.18}$$

From Eq. 4.18, we observe that the last term has negative contributions to the gradient term, which may lead to the instability of the homogeneous state.

4.3 2D case

4.3.1 Analytical treatment in the momentum-space

Just as the first step in the 3D case, minimization with respect to ρ leads to

$$\eta^2(\vec{r}) = \frac{K}{\lambda}\int \frac{(\rho(\vec{r'}) - \bar{\rho})}{|\vec{r} - \vec{r'}|}d\vec{r'}. \tag{4.19}$$

However, in contrast to 4.9, we have to consider that charges and the order parameter are defined on a plane. We chose $z = 0$ as the position of the plane along the vertical axis, and d the thickness of the plane. Hence the equivalent expression of 4.10 for the 2D case is

$$-\lambda\nabla^2_{3D}\eta^2(\vec{r}) = 4\pi K(\rho(\vec{r}) - \overline{\rho})\delta(z)d. \tag{4.20}$$

where we use the fact that the charge density is distributed on a plane of a finite thickness d.

By applying the Fourier transformation we solve the problem in k space. The next relation in momentum space holds for $\eta^2(\overrightarrow{r})$,

$$\eta^2(\overrightarrow{r}) = \frac{1}{(2\pi)^3}\int [\eta^2]_k e^{-i\overrightarrow{k}\cdot\overrightarrow{r}} d\overrightarrow{k}. \tag{4.21}$$

We should note that $[\eta^2]_k \neq [\eta(\overrightarrow{k})]^2$.

We need to take into account that in Eq. (4.20) the charge density $\rho(\vec{r})$ has a 2D dependence ($\rho(\vec{r}) \equiv \rho(x, y)$) and z dependence is due to $\delta(z)$. Then, since the Fourier transform for these delta function is $\int dz e^{ik_z}\delta(z) = 1$, after Fourier transforming Eq. (4.20) becomes,

$$\lambda(k^2 + k_z^2)[\eta^2]_k = 4\pi K d(\rho(\vec{k}) - \bar{\rho}), \tag{4.22}$$

where the momentum was decomposed into a z component given by k_z and in-plane component given by $\overrightarrow{k}$. Next, we obtain the solution of the order parameter on the plane, $\eta^2(\overrightarrow{k})_{z=0}$,

$$[\eta^2]_{k,z=0} = \frac{2\pi dK}{\lambda}\int \frac{\rho(\overrightarrow{k}) - \overline{\rho}}{k^2 + k_z^2} dk_z. \tag{4.23}$$

where we used the fact that the integral in z direction is $1/2\pi$.

Since

$$\int \frac{dk_z}{k^2 + k_z^2} = \frac{\pi}{|k|}. \tag{4.24}$$

We have

$$[\eta^2]_{k,z=0} = \frac{2\pi Kd}{\lambda}\frac{[\rho(\overrightarrow{k}) - \overline{\rho}]}{k}. \tag{4.25}$$

Or equivalently,

$$\rho(\vec{k}) - \bar{\rho} = \frac{\lambda k}{2\pi K d}[\eta^2]_k. \tag{4.26}$$

The sum of $F_{Coul} + F_{coupl}$ from the free energy density and the arranging of terms yields:

$$F_{Coul} + F_{coupl} = \frac{K}{2}[\rho(\vec{r}) - \bar{\rho}] \int \frac{\rho(\vec{r'}) - \bar{\rho}}{|\vec{r} - \vec{r'}|} d\vec{r'} - \lambda\eta^2(\overrightarrow{r})(\rho(\overrightarrow{r}) - \overline{\rho}) - \lambda\eta^2(\overrightarrow{r})\overline{\rho}. \tag{4.27}$$

Using 4.19 and integrating over $\vec{r}$ we have,

$$\Delta F = -\frac{\lambda^2}{8\pi^2 K d} \int \eta^2(\overrightarrow{r})(\rho(\overrightarrow{r}) - \overline{\rho}) d\vec{r}, \tag{4.28}$$

where $\Delta F = \int (F_{coupl} + F_{Coul} + \lambda\eta^2(\overrightarrow{r})\overline{\rho}) dr$.

Fourier transforming ρ(r) $- \overline{\rho}$ and $\eta^2(\overrightarrow{r})$,

$$\Delta F = \frac{1}{(2\pi)^4} \int e^{(\overrightarrow{k} + \overrightarrow{k}')\cdot\overrightarrow{r}} [\eta^2]_{k'} (\rho(\overrightarrow{k}) - \rho) d\vec{r} d\vec{k} d\vec{k'}. \tag{4.29}$$

By means of the following relation,

$$\int e^{-i(\overrightarrow{k} + \overrightarrow{k'})\cdot\overrightarrow{r}} d\vec{r} = (2\pi)^2 \delta(\overrightarrow{k} + \overrightarrow{k}')\cdot \Rightarrow \overrightarrow{k}' = -\overrightarrow{k}, \tag{4.30}$$

and after substituting 4.26 we get,

$$\Delta F = -\frac{\lambda^2}{8\pi^2 K d} \frac{1}{(2\pi)^2} \int [\eta^2]_k k [\eta^2]_{-k} d\vec{k}. \tag{4.31}$$

Next, since

$$|k| = \frac{\overrightarrow{k} \cdot \overrightarrow{k}}{|k|}, \tag{4.32}$$

then we can write

$$\eta^2(\overrightarrow{k}) k \eta^2(-\overrightarrow{k}) = \frac{(\overrightarrow{k}[\eta^2]_k) \cdot (\overrightarrow{k}[\eta^2]_{-k})}{|k|}, \tag{4.33}$$

We notice that if,

$$-i\int_{-\infty}^{\infty}\nabla\eta^2(\overrightarrow{r})e^{-i\overrightarrow{k}\cdot\overrightarrow{r}}d\vec{r}' = \overrightarrow{k}[\eta^2]_{-k}, \tag{4.34}$$

and

$$i\int_{-\infty}^{\infty}\nabla\eta^2(\overrightarrow{r})e^{i\overrightarrow{k}\cdot\overrightarrow{r}}d\vec{r}' = \overrightarrow{k}[\eta^2]_{k}, \tag{4.35}$$

equation 4.33 is:

$$[\eta^2]_k k[\eta^2]_{-k} = \int\int\frac{\nabla\eta^2(\overrightarrow{r})\cdot\nabla\eta^2(\overrightarrow{r})e^{-i(\overrightarrow{r}-\overrightarrow{r}')\cdot\overrightarrow{k}}}{|k|}d\vec{r}d\vec{r}'. \tag{4.36}$$

Therefore $\int\Delta F d\overrightarrow{r}$ is,

$$\int\Delta F d\overrightarrow{r} = -\frac{\lambda^2}{8\pi^2 Kd}\frac{1}{(2\pi)^2}\int\int\int\frac{\nabla\eta^2(\overrightarrow{r}')\cdot\nabla\eta^2(\overrightarrow{r})e^{-i(\overrightarrow{r}-\overrightarrow{r}')\cdot\overrightarrow{k}}}{|k|}d\vec{k}d\vec{r}d\vec{r}'. \tag{4.37}$$

If we define $\overrightarrow{R} = \overrightarrow{r} - \overrightarrow{r}'$ and we use the following relation:

$$\int\frac{e^{i\overrightarrow{R}\cdot\overrightarrow{k}}}{k}d\overrightarrow{k} = \int_0^{\infty}\frac{e^{iRk\cos\theta}kdkd\theta}{k} = 2\pi\int J_0(kR)dk = \frac{2\pi}{|R|}, \tag{4.38}$$

So,

$$\int\Delta F d\overrightarrow{r} = -\frac{\lambda^2}{4\pi Kd}\frac{1}{(2\pi)^2}\int\int\frac{\nabla\eta^2(\overrightarrow{r})\cdot\nabla\eta^2(\overrightarrow{r}')}{|\overrightarrow{r}-\overrightarrow{r}'|}d\vec{r}d\vec{r}'. \tag{4.39}$$

Therefore,

$$\int F d\overrightarrow{r} = \int[F_1 + F_{grad} - \frac{\lambda^2}{16\pi^3 Kd}\int\frac{\nabla\eta^2(\overrightarrow{r})\cdot\nabla\eta^2(\overrightarrow{r}')}{|\overrightarrow{r}-\overrightarrow{r}'|}d\vec{r}' - \lambda\eta^2(\overrightarrow{r})\overline{\rho}]d\overrightarrow{r}. \tag{4.40}$$

Note that the nonlocal gradient term is negative and is similar to Lifshitz invariants leading to instabilities of the homogeneous state. In addition, the appearance of the last term shifts this temperature to

$$\tau = \tau' - \lambda\overline{\rho}. \tag{4.41}$$

We point out that

$$a = \frac{\lambda^2}{16\pi^3 K d}, \tag{4.42}$$

measures the strength of the coupling. Additionally, due to the fact that it is the coefficient of the long range term, it also controls the degree of frustration.

4.3.2 Numerical Solution

In order to minimize the dimensionless free energy $\int F d\vec{r}$, we use the conjugated gradient method CGM (Appendix A). We introduce Nx$N (N = 128)$ discrete points on the square of length L (the length is measured in units of ξ). Since we expect that minimization of the free energy is realized on a periodic structure, we apply periodic boundary conditions. To eliminate the role of the incommensurability, we have studied the energy for different sizes of the system. For fixed length, L, the free energy depends on two parameters: a and τ. Our ultimate goal is to construct the phase diagram a vs τ; this is detailed in the next section. Henceforth we refer in our calculations to the energy E defined by:

$$E = \frac{\int F d\vec{x}}{U_o \xi^2}, \tag{4.43}$$

where $\overrightarrow{r} = \xi \overrightarrow{x}$. Here U_0 is the density of energy between to phases. We start from the higher temperature than $\tau = 1$. Figure 4.1 shows the first three patterns developed as the temperature is reduced from $\tau = 1.3$ to $\tau = 1.1$ with $a = 1$. The first non-uniform distribution of charges takes the shape of rounded clusters at $\tau = 1.3$ and $\tau = 1.2$ where the patterns are in a metastable phase. It is for $\tau = 1.1$, when the phase separation becomes the stable phase; the elongation of the bubbles shape is signaling that at lower τ stripes may develop. The figure also provides complementary information regarding the charge density and the order parameter. It displays how both distributions are linked (see Eq. 4.20). The charge density tends to follow the patterns formed by the order parameter. One important feature observed, particularly for $\tau = 1.2$ and $\tau = 1.1$, is the creation of charged domain walls which separate low and high charge density regions.

In Figure 4.2 we show a periodic free energy behavior as function of L. It is due to the commensurability-incommensurability effect of intrinsic period of superstructures with the size of the sample L. For $10 \leq L \leq 15$, straight stripes cover the range and the first minimum is found at $L = 14$. At $L = 16$, distorted stripes are formed due to incommensurability. At $L = 17$ diagonal stripes with a higher energy occur. The same series of patterns, straight-wiggled-diagonal stripes, are repeated for each energy

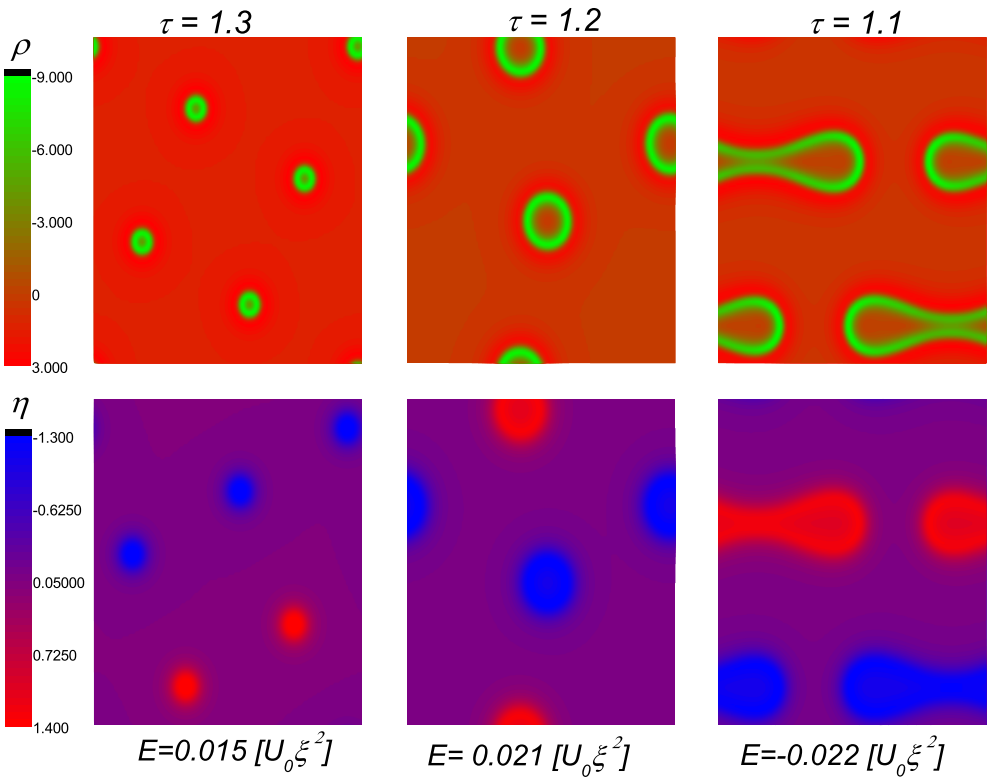

FIGURE 4.1: First charged patterns (top panels) and order parameter distributions (bottom panels) observed between $1.4 < \tau < 1.1$ for $a = 1$. At $\tau = 1.3$ (left panels) and $\tau = 1.2$ (center panels) they are metastable and the disorder phase is stable. At $\tau = 1.1$ (right panels) charge separation is the favorable phase.

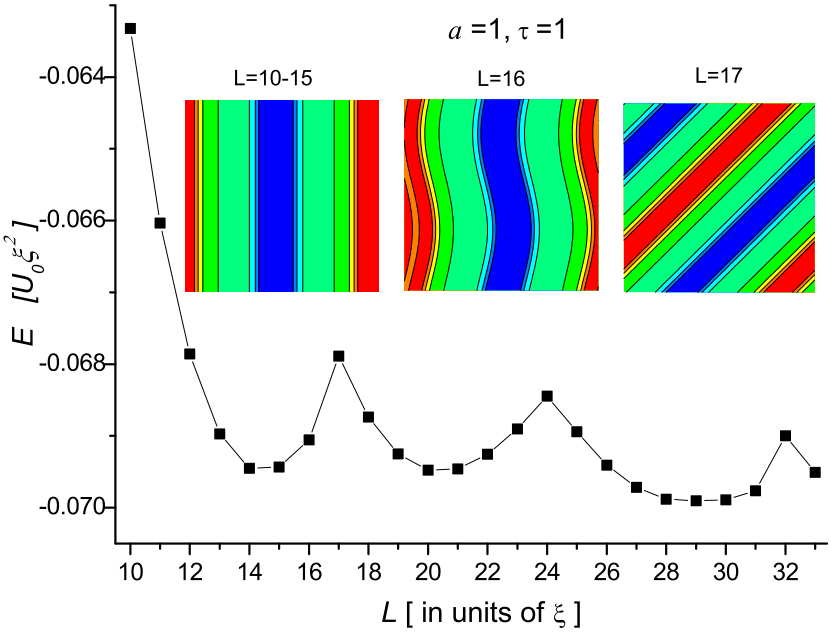

FIGURE 4.2: Free energy obtained by minimization of Eq. (4.40) for different sizes LxL. Parameters were set to $a = 1$ and $\tau = 1$. Spatial variation of $\eta(\vec{r})$ is shown in the insets.

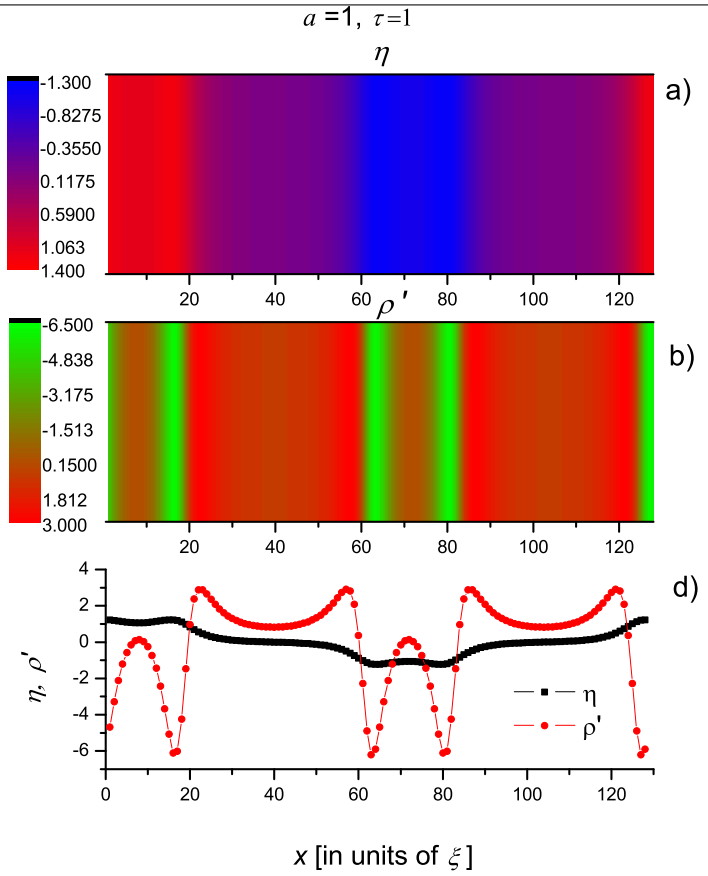

FIGURE 4.3: a) variation of the order parameter $\eta(x, y = const.)$ (black curve in panel c). b) variations of the local charge density defined by $\rho'(\vec{r}) = \rho(x, y = const.) - \overline{\rho}$ (red curve in panel c). The set of parameters used are: $a = 1$, $\tau = 1$ and $L = 14$.

minimum. The second minimum at $L = 20$ corresponds to diagonal stripes. Minimum of the free energy corresponds to the case when the size of the square is commensurate with the stripe period. We have calculated the charge density through Eq. (4.20) and plotted it in Figure 4.3 together with the values of the order parameter. It is clearly seen from this plot, that positive and negative charges are localized near the sharp domain wall. It is important to point out that Eqs. (4.20) and (4.26) satisfy the electroneutrality condition.

The transition from one stable configuration to another depends on the combination of parameters $\tau \approx 1$ and $a \approx 1$. We illustrate the transition bubbles-stripes in figure 4.4 for $a = 1.1$. If we start at very high temperatures, $\tau > 1.1$, the order parameter is uniformly zero and the system is in the disordered phase (not shown in figure). At $\tau = 0.95$ the transition from stripes to bubbles begins. At $\tau = 1.1$ bubble-like structures are fully established as the most stable configuration. The lowest energy is found at $L = 18$. In general, depending on τ, both structures (stripes and bubbles) are found for $a = 1$ and $a = 1.1$. Clearly at $\tau = 0.9$, stripes are no longer the ground state of the system. The

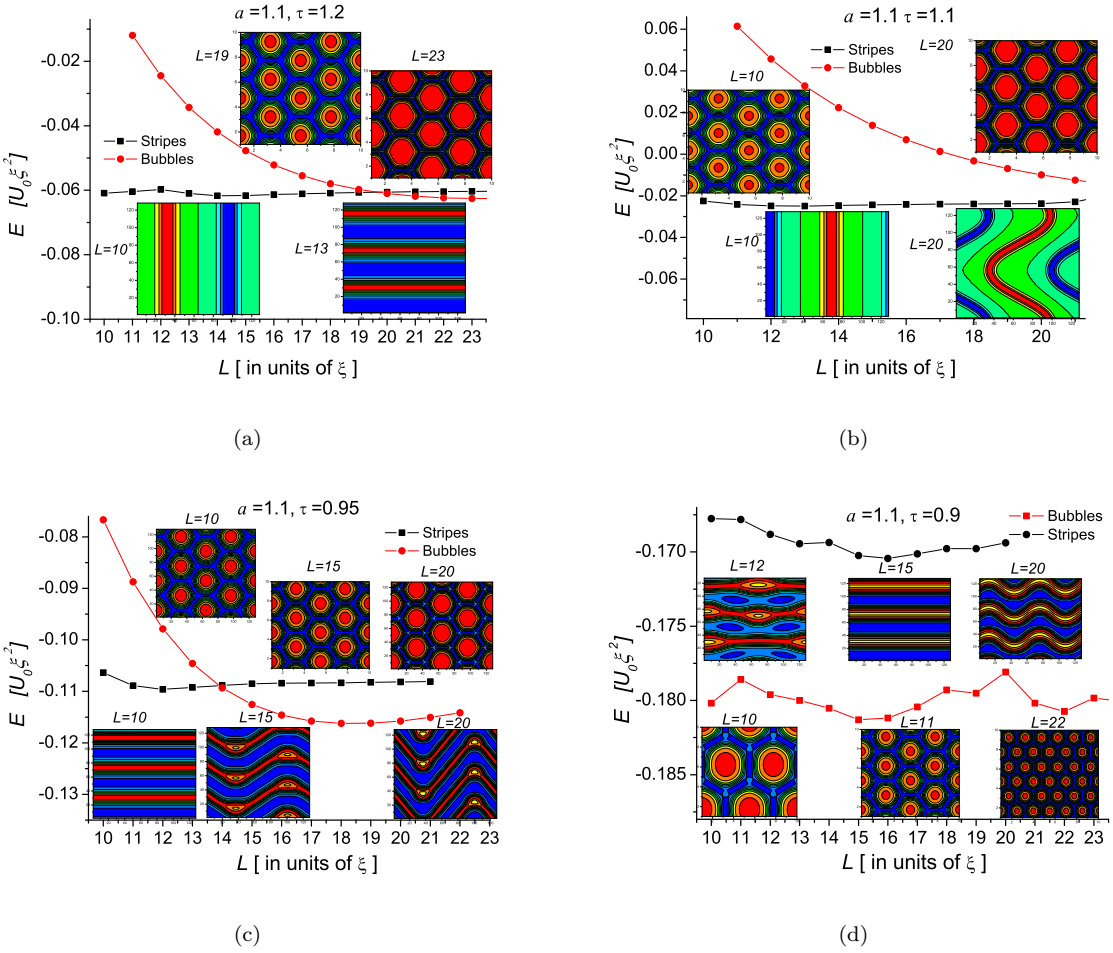

FIGURE 4.4: Stripe-bubble phase transition as function of temperature for $a = 1.1$. (a) At $\tau = 1.2$ stripes present the most stable configuration. In some cases stripes are distorted due to incommensurability effects. (b) At $\tau = 1.1$ the minimum is found at $L \approx 20$ when bubbles are ordered in honeycomb-like structures; stripes become metastable. (c) Stripes remain with higher energy than bubbles. (d) Further decrease of τ makes bubbles a much more stable configuration.

free energy of bubbles is lower than stripes for $a = 1.1$ and $0.7 < \tau < 0.95$. Further decrease of the temperature leads to the homogeneous phase (not shown).

The competition for the most stable configuration is illustrated in figures 4.5 for a weaker degree of Coulomb frustration, $a = 0.8$. It is seen that both patterns might be present for $a = 0.8$ and temperature range $\tau = 0.9 - 1.05$. First two figures indicate that stripes have lower energy than bubbles. Nevertheless, when the effective temperature τ is reduced, the energies of the striped phase and ordered bubbles become close to each other. At $\tau = 1.05$ and $\tau = 1.0$, the one dimensional structures of stripes have lower energy. Starting from $\tau = 0.95$, the two dimensional structures of bubbles dominates. Further decrease of the temperature leads to the homogenous state (not shown in figure). In that case, striped patterns exist, but have higher energy than the uniform state. Therefore

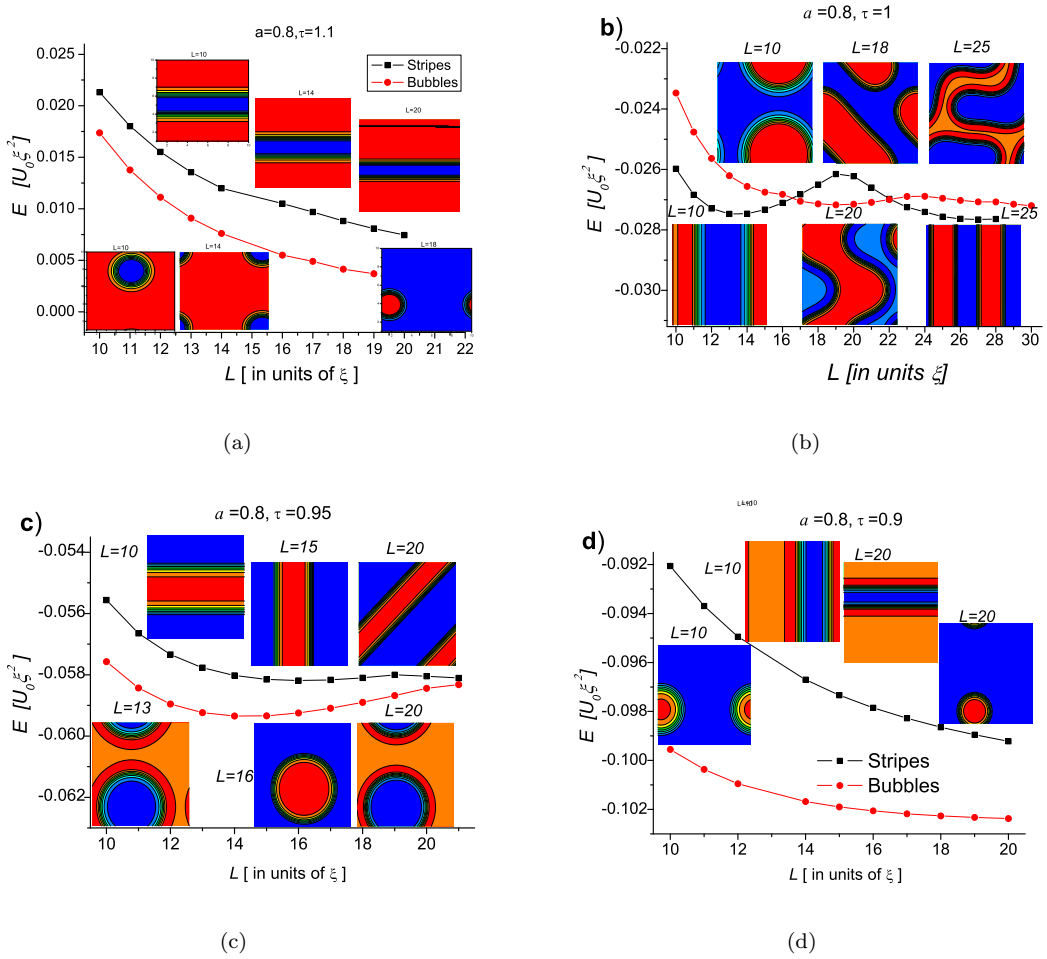

FIGURE 4.5: Stripe-bubble phase transition as function of temperature for $a = 0.8$. In all panels red and black curves are for bubbles and stripes respectively. (a) At $\tau = 1.05$ stripes present the most stable configuration. (b) If temperature is decreased to $\tau = 1$, both patterns get closer in energy. (c) At $\tau = 0.95$, regardless of L, the two dimensional structure of bubbles has fully achieved the lowest energy; stripes are arranged diagonally. (d) At $\tau = 0.90$ bubbles are reduced in size. After the homogeneous phase is achieved, the stripes remain as a metastable phase.

we conclude that a first order phase transition from stripes to ordered bubbles and then to uniform phase takes place as a function of temperature.

4.3.3 Phase diagram

The complete phase diagram is shown in figure 4.6. The general trend is that the stripe phase is close to temperature $\tau = 1$. The bubbles phase appears at temperatures (τ_b)above and below the temperature formation of stripes (τ_s). However, while τ_s tends to remain close to the line $\tau = 1$ for all values of a, τ_b extends to higher temperatures as a is increased. Moreover, in the phase diagram, the bubbles regions are rather symmetric

around the axis defined by the stripes sector. The disordered phase is seen at $\tau > \tau_b$ and it gets closer to the stripe region as a is reduced. Similarly, the homogeneous phase exist for $\tau < \tau_b$ and also gets closer to the stripes region as a is reduced. In fact, as function of τ there is a first order transition which does not cross the inhomogeneous phase. The point defined by $a \approx .35$ and $\tau = 1$, delimits the absence of any phase separation as τ is lowered. Here the effects of LRCI are not strong enough to play an important role during the transition. However this threshold value may be due to size effects and the exact value of a can be shifted.

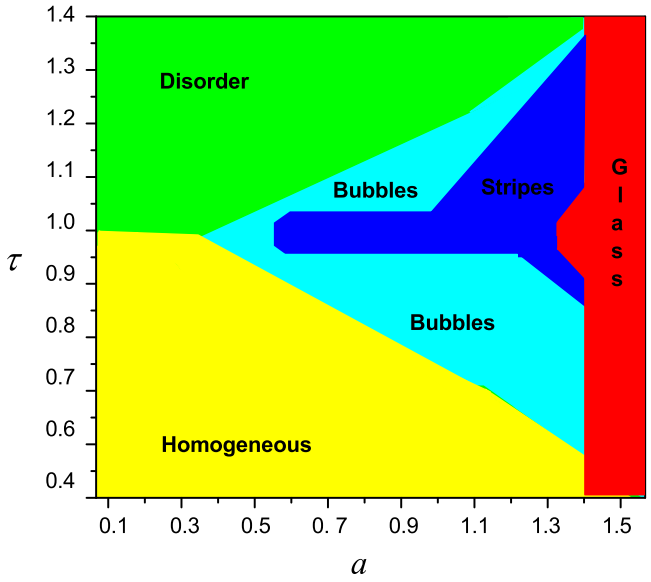

FIGURE 4.6: Phase diagram τ vs a for the model defined by Eq. (4.40). As a function of τ, the transition from the disordered to the homogeneous phase can be achieved in different ways. Besides the direct transition, in the region defined by $a < 0.25$, the transition can also cross a series of inhomogeneous phases. This inhomogeneities can take the form of periodic charge density structures, either with bubble or stripe shapes. At sufficient strong couplings, $a > 1.4$, the system develops a glassy phase.

To demonstrate that the uniform solution has a higher free energy than a nonhomogeneous solution. We make the Fourier transformation of $F_{grad}(\overrightarrow{r})$ as well as the nonlocal gradient term, $F_{nonlocgrad}(\overrightarrow{r})$ defined by the third term in Eq. 4.40,

$$F_{nonlocgrad}(\overrightarrow{r}) = a \int \frac{\nabla\eta^2(\overrightarrow{r}) \cdot \nabla\eta^2(\overrightarrow{r}')}{|\overrightarrow{r} - \overrightarrow{r}'|} dr'. \tag{4.44}$$

Therefore the Fourier transforms is

$$F_{grad}(\overrightarrow{k}) + F_{nonlocgrad}(\overrightarrow{k}) = k^2|\eta(\overrightarrow{k})|^2 - 2ak|[\eta^2]_k|^2, \tag{4.45}$$

where $\eta(\overrightarrow{k})$ and $[\eta^2]_k$ are Fourier components of the order parameter and square of the order parameter, respectively. If we assume that the solution is uniform, i.e., $\eta(\overrightarrow{k}) \neq$ and $\eta^2(\overrightarrow{k}) \neq 0$, small nonuniform corrections to the solution reduce the free energy at small $\overrightarrow{k}$, where the second term dominates. From Eq. 4.45 we can infer that larger values of a lead to finer domains.

In the low symmetry phase the density function becomes

$$\rho(\overrightarrow{r}) = \overline{\rho} + \delta\rho(\vec{r}), \tag{4.46}$$

where $\delta\rho(\vec{r})$ is the density fluctuation necessary to form the low symmetry phase.

Let us first discuss the cases of the low frustration regime. It corresponds to the region which roughly covers $0.3 < a < 0.6$. In the low frustration regime is expected that wave-vector presents smaller values than the intermediate and the high frustration regimes. Therefore we should observe larger periodicity in the patterns. The intermediate and the high frustration regimes correspond to $0.6 < a < 1.3$ and $a > 1.3$ respectively.

In sharp contrast, much larger values in the highly frustrated regime introduce finer regions of charge density and complex patterns. Complex charge domains of reduced area are observed (see Figure 4.7). In addition the periodicity has been lost. Here we have entered into the "glass" region. In order to define this region, we take as criteria the number of equivalent configurations with same energy found by the CGM. We refer to the section 3.5.1 where we introduced this criteria.

In the intermediate frustration regime, though a few minima may be developed in the free energy as function of charge configurations, the CGM is capable to find the optimal charge density arrangement. The characteristic patterns are either stripes or rounded-like shapes (bubbles). Depending on τ and a these patters may vary in orientation and size. As the temperature is reduced different phases are crossed. Starting from the disordered phase at high τ, then entering into the inhomogeneous phase -composed by either stripes or bubbles at lower τ. Finally ending up at the lowest τ in the homogeneous phase. Although the inhomogeneous phase could have been predicted analytically, it is much more challenging to determinate the exact shape of the regions.

4.4 Inhomogeneities subject to disorder

Following the discussion given in section 3.5 we study the stability of the inhomogeneous phase. The total free energy density which describe the inhomogeneous phase subject

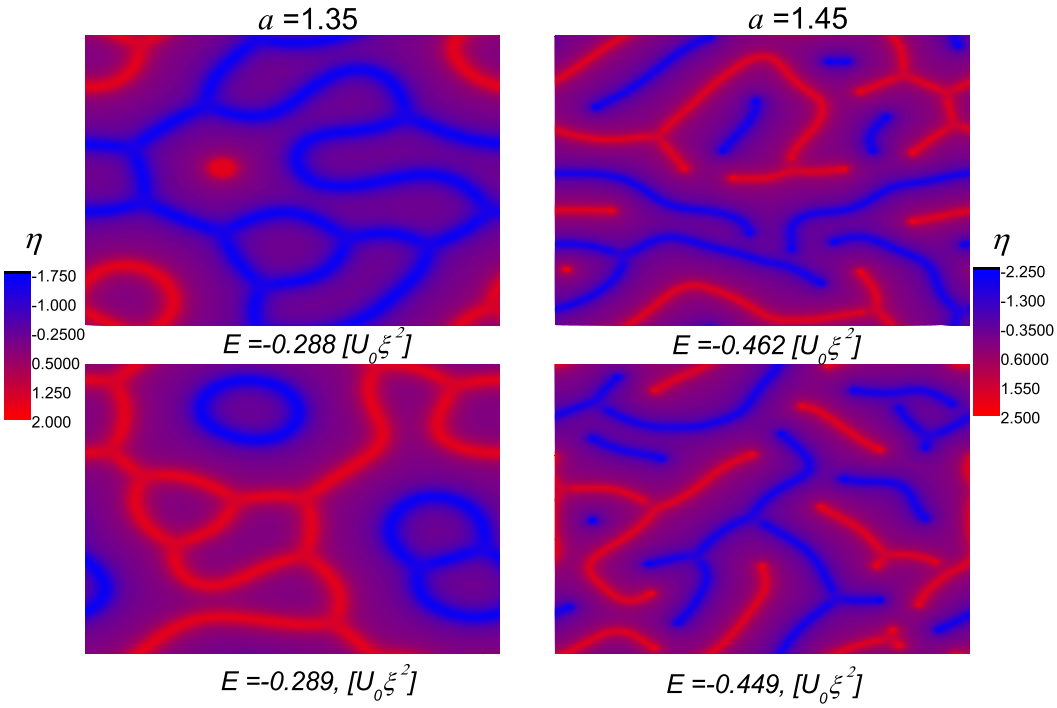

FIGURE 4.7: High values of a lead to the strongly frustrated regime. It is characterized by the emergence of complex domains whose energies are nearly the same. The figure shows order parameter distribution for four of such domains when $a = 1.35$, $L = 18$ (left panels) and $a = 1.45$, $L = 15$ (right panels), both at $\tau = 1$. Filamented structures remain at $a = 1.35$. At $a = 1.45$ the stronger frustration reduce the length of these patterns

to disorder is given by the four terms defined in Eq. 4.8 plus a term which describes the coupling of the order parameter to the local static random charge density:

$$F = F_1 + F_{coupl} + F_{grad} + F_{Coul} + W(\overrightarrow{r})\eta^2(\overrightarrow{r}). \tag{4.47}$$

The last term describes the coupling of the order parameter to local fluctuations. For instance $W(\overrightarrow{r})$ may represent the random distribution of impurities. It is defined within a box of width of W_d.

The results of the minimization by the CGM are shown in Fig. 4.8. The set of parameters was chosen as $a = 0.8$ and $\tau = 1.05$. We investigate how the two typical phase states (bubbles and stripes) behave as the level of randomness is increased. Firstly for values $W_d < 1.5$ configurations whose original shape were bubbles remain with the lowest energies. Stripes energy also remain as patterns with a higher energy. Both type of

configuration fairly maintain a bubble-like or stripe-like shape below $W_d < 1$. At $W_d = 1.5$ a rather drastic changes are observed, particularly to the bubble configurations. W_d leads to a complete melting of bubbles while wavy stripes survive. Since the degree of frustration was set to $a = 0.8 < W_d = 1$, we can safely say that, under this set of parameters, the charge segregation is quite stable against disorder.

4.5 Conclusions

In the presence of Coulomb repulsion the global phase separation becomes unfavorable and the system shows a mesoscopic phase separation. The phenomenological theory of this effect was formulated where the square of the order parameter is coupled with the charge density. We showed that the average charge density plays the role of the local temperature. After eliminating the dependence of the charge density in the free energy, a numerical procedure is used to find the patterns which minimize the free energy. The results indicate a sequence of first order phase transitions as temperature is lowered; from stripes to bubbles and finally to a homogeneous phase at the lowest temperature. The size and shape of the charged regions is determined by the competition between the ordering energy and the Coulomb energy. In particular, it demonstrates that a striped phase exists but is quite subtle; in the absence of disorder it is stable only at some intermediate finite temperature. However, when disorder is introduced we observed remains of the stripe phase. They show higher stability than bubbles when the disorder is taken into account. Among the possible short-range forces relevant for our model, we can mention spin fluctuations and local lattice instabilities such as JahnTeller (JT) distortions. It is precisely the JT interaction which will be subject of extend study in the second part of the thesis.

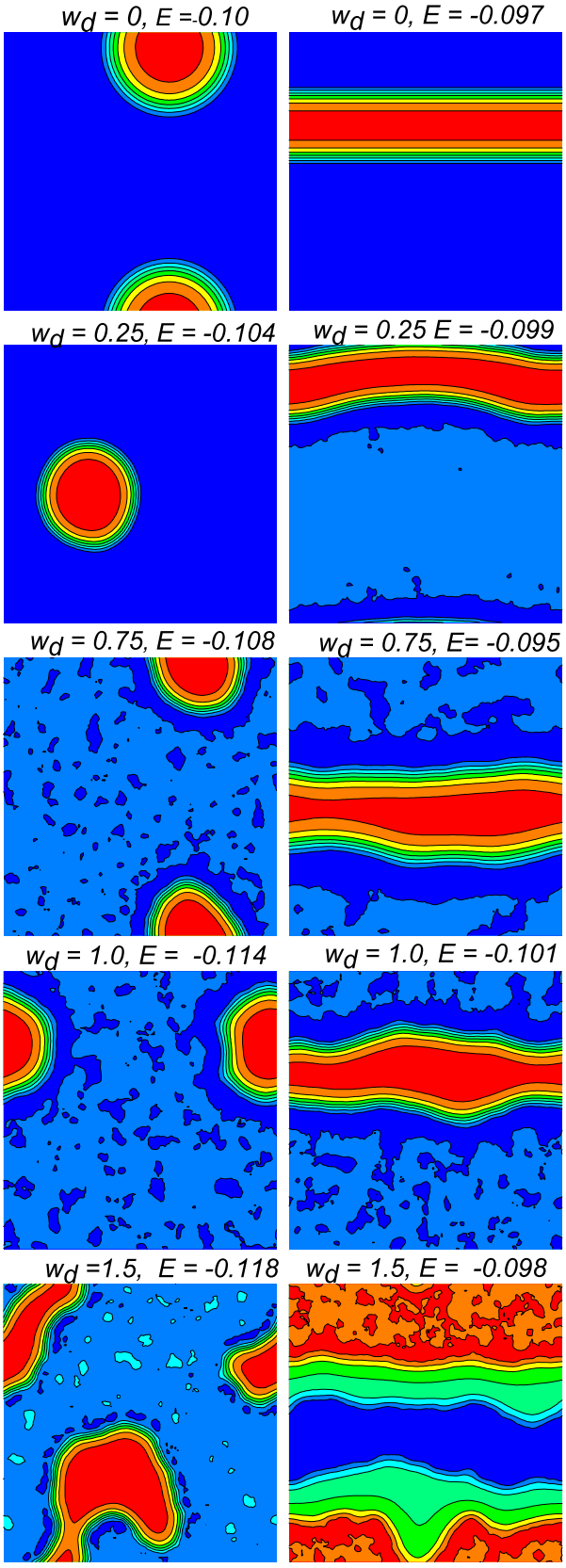

FIGURE 4.8: Bubbles (left column) and stripes (right column), subject to random disorder for $a = 0.8$ and $\tau = 1.05$. The level of disorder is measured by the parameter W_d. Its value is increased from top to bottom. The original shapes are rather conserved as long as $W_d < 1.5$. Both phases start to melt when $W_d = 1.5$ is reached.

Chapter 5

Jahn-Teller polarons in cuprates.

5.1 Introduction

In many cases in the solid state physics or molecular physics, it is a valid approximation to consider the electrons moving much faster than the the nuclei. This assumption turns out to be very convenient because it simplifies the solution of the problem defined by the Hamiltonian of a system under study. It leads to treating the electrons moving effectively in a static field given by the quasi-static state of the ions. The approximation relies on the different time scale of the electrons and the nucleus motion, or equivalently on their mass differences. The approximation is known as the adiabatic or the Born-Oppenheimer approximation. What we next present is the changes required to such approximation in systems with a highly symmetrical arrangement of nuclei and with electronic degeneracy. This is the origin of the JT effect. The chapter opens the second part of the thesis, where this effect will be a fundamental ingredient. In the first section the idea is developed from a molecular point of view. The criterion for the presence or absence of degeneracy will be presented which is, together with the structural symmetry, one of the basic conditions for the JT effect. Afterwards we review how the JT effect has been used in the context of cuprates. Some key experiments that have revealed the inhomogeneous phase will be presented. At the end of the chapter we introduce a model which tries to explain the emergence of JT-domains. This model is of a capital importance since it is the starting point of the second part of the dissertation.

5.2 The Jahn-Teller theorem.

The Hamiltonian in consideration, either for a molecule or a solid, is

$$H = H_r + H_Q + V(r, Q) = 0. \tag{5.1}$$

The corresponding Schrödinger equation is

$$(H - E)\Psi(r, Q) = 0, \tag{5.2}$$

where H_r and H_Q are the electronic and nuclei kinetic energies respectively and $V(r, Q)$ is the electrons-nuclei potential. The coordinates of electrons are r_i, $i = 1, 2, ..., n$ and for convenience we denote the symmetrized coordinates of nuclei as Q_α, $\alpha = 1, 2, ..., N$. $V(r, Q)$ can be expanded in terms of a series of displacements around equilibrium position of nuclei denoted as $Q_{\alpha 0} = 0$,

$$V(r, Q) = V(r, 0) + \sum_\alpha (\frac{\partial V}{\partial Q_\alpha})_0 Q_\alpha + \frac{1}{2} \sum_{\alpha,\beta} (\frac{\partial^2 V}{\partial Q_\alpha \partial Q_\beta})_0 Q_\alpha Q_\beta + ... \tag{5.3}$$

If the displacements are neglected only V(r, 0) is retained leading to the electronic Schödinger equation for the configuration $Q_{\alpha 0} = 0$. Additionally we can take the electronic wave function, ψ, independent of Q. In this way the electronic Schödinger equation is:

$$[H_r + V(r, 0) - \epsilon'_k]\psi_k(r) = 0. \tag{5.4}$$

Here k describes different electronic quantum numbers. In order to evaluate when the displacements around the equilibrium positions becomes important, we start with the expansion of the total wave function Ψ in terms of the electronic wave functions, $\psi_k(\mathbf{r})$. This leads to:

$$\Psi(r, Q) = \sum_k \chi_k(Q)\psi_k(r), \tag{5.5}$$

where χ_k is the function of nuclear coordinates. It is worth to notice that sometimes, the electronic wave function should have a parametric dependence on Q: $\psi \equiv \psi(r; Q)$. This is might be referred as the full adiabatic approximation which leads to more elaborated calculations. But for our purpose we have followed the derivation given in ref. [42] which is more suitable to describe the JT effect. There the derivation starts with the crude adiabatic approximation.

From the last two expressions we obtain,

$$[H_Q + \epsilon_k(Q) - E]\chi_k(Q) + \sum_{m \neq k} W_{km}(Q)\chi_m(Q) = 0. \tag{5.6}$$

The electronic matrix elements W_{km}, known as vibronic interactions, are mixing the electronic wave-function with the changes of position of the nuclei. If we denote the operator

$$W = V(r,Q) - V(r,0) = \sum_{\alpha} (\frac{\partial V}{\partial Q_\alpha})_0 Q_\alpha + \frac{1}{2}\sum_{\alpha,\beta} (\frac{\partial^2 V}{\partial Q_\alpha \partial Q_\beta})_0 Q_\alpha Q_\beta + ... \tag{5.7}$$

then W_{km} is defined as

$$W_{km} = < \psi_k | W | \psi_m > \tag{5.8}$$

and the energy for a given nuclear configuration is

$$\epsilon_k(Q) = \epsilon'_k + W_{kk}(Q). \tag{5.9}$$

The key role of the matrix elements is that they measure how the electrons affect the nuclear displacements and how the nuclear displacements influence electrons.

However, if the vibronic mixing is absent, $W_{km} = 0$, for $k \neq m$, the displaced energy of nuclei within a field of electrons is given by simpler equations,

$$[H_Q + \epsilon_k(Q) - E]\chi_k(Q) = 0, \tag{5.10}$$

and $\epsilon_k(Q)$ becomes what is known as adiabatic potential energy surface (APES). It is the potential energy of the nuclei in the presence of electrons. In other words, the problem can be solved by first computing the electronic wavefunctions. Then they are used for the potential energy of the nuclei. Afterwards, the nuclei wave function, $\chi(Q)$, and its energy is estimated. Finally the total wave function, $\Psi(r,Q)$, is calculated.

As we mentioned, this is valid when there is no degeneracy. In general for two electronic states m and k, the condition is satisfied as long as energy of a quantum of vibration, $\hbar\omega$ is much smaller than the energy difference of the two electronic states [42]:

$$\hbar\omega \ll |\epsilon_m - \epsilon_k|. \tag{5.11}$$

Now we turn to the situation when the condition (5.11) does not hold. Consider the splitting of degenerated levels when the nuclear configuration is changed from the origin $Q_0 = 0$. The energies are obtained by solving Equation (5.4). Let us consider the f-fold degenerated electronic state, $\psi_k(r)$, $k = 1, 2, ...f$ having the same energy, ϵ_k. In order to address this point, it is necessary to calculate the vibronic effect on the energy levels. Thus,

$$\begin{pmatrix} W_{1,1} - \epsilon & W_{1,2} & . & . & . & W_{1,f} \\ W_{2,1} & W_{2,2} - \epsilon & . & . & . & W_{1,f} \\ . & . & . & . & . & . \\ . & . & . & . & . & . \\ . & . & . & . & . & . \\ W_{f,1} & . & . & . & . & W_{f,f} - \epsilon \end{pmatrix} = 0. \tag{5.12}$$

Now we will explicitly use the group theory to label the electronic wave-functions and the vibrational modes. This is the method of choice, particularly when the JT problem is solved. Hence the vibronic terms $W_{ij} =< i|W|j >$ are now defined throughout the operator W

$$W = \sum_{\Gamma,\gamma} (\frac{\partial V}{\partial Q_{\overline{\Gamma},\gamma}})_0 Q_{\overline{\Gamma},\gamma} + \frac{1}{2} \sum_{\Gamma',\gamma',\Gamma'',\gamma''} (\frac{\partial^2 V}{\partial Q_{\overline{\Gamma}',\gamma'} \partial Q_{\overline{\Gamma}'',\gamma''}})_0 Q_{\overline{\Gamma}',\gamma'} Q_{\overline{\Gamma}'',\gamma''} + ... \tag{5.13}$$

Here we represent $\overline{\Gamma}$ as the irreducible representation [1] for the symmetrized displacements under the symmetry operation of the molecular point group [2] (in case of a solid, the lattice point group is used). The irreducible representation, $\overline{\Gamma}$ with f- fold degenerated representations has as $\gamma = 1, 2, ...f$ degeneracy. As an example, the two twofold degenerated state of $\overline{\Gamma} = E$ has $\gamma = \epsilon, \vartheta$. Similarly, in the case of electronic degeneracy in the presence of high symmetric nuclei geometries it is convenient to use the group theory. Henceforth we use $\overline{\Gamma}$ for atom displacements and Γ for electronic states.

For example, keeping only the linear terms in 5.13 we get

$$W_{ij} = \sum_{\overline{\Gamma},\overline{\gamma}} \langle i|(\frac{\partial V}{\partial Q_{\overline{\Gamma},\overline{\gamma}}})_0|j\rangle Q_{\overline{\Gamma},\overline{\gamma}}. \tag{5.14}$$

[1] A representation of a symmetry operation of a group, which cannot be expressed in terms of a representation of lower dimension. When the representation of the group is in matrix form (i.e. a set of matrices that multiply in the same way as the elements of the group), the matrix representation cannot be put into block-diagonal form by constructing a linear combination of the basis functions

[2] Operation that leave the ions of the molecule unchanged. For instances proper rotations around a symmetric axis or reflections across symmetric planes.

The importance of the expression (5.14) is that non-zero values of any of its elements, imply that the secular equation (5.12) contains linear in $Q_{\overline{\Gamma}\overline{\gamma}}$ corrections to ϵ_k. Therefore, the minima of some of ϵ_k would not be at $Q_{\overline{\Gamma}\overline{\gamma}} = 0$. Using the previous notation, this can be stated as: the APES of an f-degenerated electronic state, meaning that states with label $k = 1, 2, ..f$ have the same energy, will have for at least one of its f-folded sheets a minimum out of the metastable point $Q = 0$, (the crossing point of all the sheets). The shift of the APES minima is demonstrated in Fig. 5.1.

Then, we need to analyze the condition when equation 5.14 is non-zero. As previously mentioned, we characterize the electronic states by their irreducible representation Γ of the point group of the molecule. The diagonal terms represents electronic forces at state Γ inducing non-symmetric displacements of the nuclei of $\overline{\Gamma}$ symmetry. From the group theory it is known that Eq. (5.14) is non zero if and only if the symmetric product $[\Gamma x \Gamma]$ contains the representation of the symmetrized displacement $\overline{\Gamma}$. In the case of one dimensional representations $[\Gamma x \Gamma] = A_1$, where A_1 is the total symmetric representation. Here we must make an important distinction. Symmetric deformations of the A_1 type do not cause lifting of the degeneracy of the electronic level. Electronic-vibrational coupling in general could cause symmetric distortion. However, the JT effect takes place due to couplings with non-symmetric vibrations. Such cases emerge when the product of $[\Gamma x \Gamma]$ includes non-symmetric representations. This is the essence of the analysis performed by H. A. Jahn and E. Teller [43].

To summarize; an analysis based on the point symmetry group for a molecule allows to show when non-symmetric displacements are present. In turns this makes the electronic degeneracy unstable. As a consequence, the degeneracy is lifted if the nuclei move to a new position of equilibrium (figure 5.1). The JT theorem is better stated in the original paper of 1937 [43], which reads, *"for a non-linear molecule in an electronically degenerate state distortion must occur to lower the symmetry, remove the degeneracy, and lower the energy".*

5.3 Basic notion of polarons and bipolarons

Before moving on to the formulation of the JT effect in the context of cuprates, we need to review briefly the basic concepts regarding polarons, bi-polarons and their relation to e-ph coupling. It is important to underline that JT distortions we will discuss are directly related to these concepts.

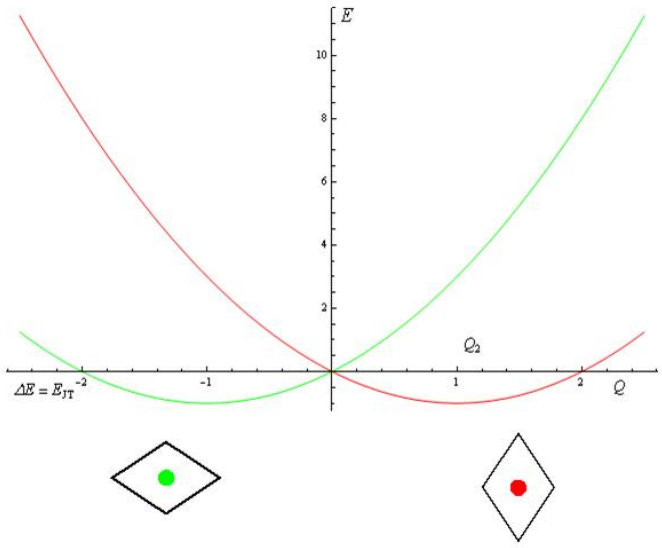

FIGURE 5.1: Adiabatic potential as a function of coordinates which depict the JT-effect. The two lowest energies correspond to the two equivalent lattice configurations at $Q = \pm 1$. The metastable energy corresponds to the symmetric configuration (not shown).

5.3.1 Polaron survey

One consequence of the e-ph coupling, for instance in ionic crystals, is the deformation of the lattice surrounding the electron. Basically this is due to the fact that electrons are charged negatively while the lattice is charged positively. Equivalently we can say that the electrons have polarized the lattice. So, if the electron moves through the crystal with weak electron-phonon coupling, it leaves behind a distorted region. But in the case of strong electron-lattice interaction a self-trapping effect may happen: the electron is localized within the distorted region. This combination of charge and lattice interaction leads to the concept of small polaron. The specific properties of this composite particle is material dependent. The polaron concept is not restricted to ionic materials. The idea about polarons goes back to 1933 when L. D. Landau first suggested the concept. Through the years several authors have contributed to the field and today it is rather an active field. For a recent review we refer to [44].

The parameter that is used very often to measure the strength of the electron-phonon is the dimensionless coupling constant α

$$\alpha = \frac{e^2}{\hbar}\sqrt{\frac{mc}{2\hbar\omega_0}}\left(\frac{1}{\epsilon_\infty} - \frac{1}{\epsilon_0}\right), \tag{5.15}$$

where ϵ_0 and ϵ_∞ are the static and high frequency dielectric constants, respectively, while ω_0 is the phonon frequency and m is the bare electron band mass. Typical values of coupling for semiconductors are $\alpha = 0.068$ in GaAs or $\alpha = 0.29$ in CeTe. In contrast, stronger couplings are found in oxides, such as $SrTiO_3$ with $\alpha = 3.77$.

The classification of polarons depends on the type of material (polar or molecular material). In some cases only large polarons can exist. In molecular materials only small polarons may be formed (Holstein model [45]). Therefore classification of polarons is in accordance with their size (small or large) and in accordance with their coupling with lattice (weak and strong coupling). Large polaron are usually studied by the Fröhlich approach [46]. The JT polarons that we will deal with can be regarded as small polarons.

In ref. [47] the conditions to find strong-coupling large polarons are discussed. The condition to be fulfilled is $\alpha^2 >> 5$ which at least for metal oxides is not realized. A second parameter which allows to relate the polaron with the electron band properties is λ. The dimensionless coupling constant defined as the ratio of the polaron energy and the half the bandwidth (D) is $\lambda = E_p/D$. Within the Holstein treatment, the collapse of a large polaron into small is expected at $\lambda = 0.5$. Similarly, the transition from the adiabatic $t >> \omega_0$ to non-adiabatic $t = \omega_0$ regime is defined by $\lambda_c = 0.5$. Here t is the electron hopping integral.

5.3.2 Electron-phonon interaction

Using the second quantization notation for phonon and electron states, the Hamiltonian representing an electron moving in crystal and interacting with phonons is [48]:

$$\begin{aligned} H &= \sum_{i,j} T(\mathbf{m}-\mathbf{n})\delta_{ss'} c_i^\dagger c_j + \sum_{m,n,s} n_{\mathbf{m},s}\mathbf{u}_\mathbf{n} \cdot \nabla_\mathbf{n} v(\mathbf{m}-\mathbf{n}) + \sum_{\mathbf{m}} \omega_0 (d_\mathbf{m}^\dagger d_\mathbf{m} + \frac{1}{2}) \\ &+ \frac{1}{2}\sum_{i\neq j} V_c(\mathbf{m}-\mathbf{n}) c_i^\dagger c_i c_j^\dagger c_j. \end{aligned} \tag{5.16}$$

where the phonon annihilation (creation) operators d ($d^\dagger$) and the electron annihilation (creation) operators c ($c^\dagger$) are defined in a Wannier representation; while $i = (\mathbf{m}, s)$ includes lattice sites ($\mathbf{m}$) and spin s and $T(\mathbf{m}) = (1/N)\sum_k E_k e^{i\mathbf{k}\cdot\mathbf{m}}$ is the bare hoping integral following a dispersion energy in k. The single ion potential $v(\mathbf{r})$ varies over the distance, which is larger than the radius of the orbits; $n_i = c_i^\dagger c_i$ is the charge density operator. In this section and in section 5.3.2 we set $\hbar = 1$.

In the real space, the lattice displacements are defined by

$$\mathbf{u_m} = \frac{\mathbf{e}}{\sqrt{2M\omega_0}}(d_m^\dagger + d_m), \tag{5.17}$$

where $\mathbf{e}$ is the unit polarization vector. Therefore one can define the electron-phonon interaction, the second term in Eq. (5.16), as

$$\omega_0 \sum_{\mathbf{n},\mathbf{m},s} g(\mathbf{m}-\mathbf{n})(\mathbf{e}\cdot\mathbf{e_{m-n}})n_{\mathbf{m},s}(d_\mathbf{n}^\dagger + d_\mathbf{n}), \tag{5.18}$$

where,

$$g(\mathbf{m}) = \frac{1}{\omega_0\sqrt{2M\omega_0}}\frac{dv(\mathbf{m})}{dm}, \tag{5.19}$$

is the dimensionless force acting between the electron on site $\mathbf{m}$ and the displacement on site $\mathbf{n}$ and $\mathbf{e_{m-n}} = (\mathbf{m}-\mathbf{n})/|\mathbf{m}-\mathbf{n}|$ is the unit vector in the direction from the electron $\mathbf{m}$ to the ion $\mathbf{n}$; M is the ion mass. V_C is the Coulomb interaction.

5.3.3 Bipolaron survey

The criteria given in section 5.3.1 have to be modified for the formation of stable bipolarons. In order to establish these new conditions we need to introduce the concept of bipolaron. It refers to the situation of two charges moving in the same potential well induced by their presence. Similar to the polaron case two type of bipolarons can be defined according to their size. The first type is usually found in ionic crystals and includes strong and intermediate coupled large bipolarons; they are formed by two large polarons. The second type is the small bipolaron and it is found in any solid provided that the electron-phonon interaction is strong enough to attract two small polarons within a common potential well. Generally, on-site bipolarons refer to a situation in which the electrons are at the same lattice site, while the term inter-site bipolaron refers to electrons being at neighboring sites.

The conditions for the stability of two paired polarons are quite subtle. First of all, the two charged polarons need to overcome the Coulomb repulsion. Following the Frohlich approach, the parameter

$$U = \frac{1}{\hbar\omega_o}\frac{e^2}{\epsilon_\infty}\sqrt{\frac{m\omega_0}{\hbar}}, \tag{5.20}$$

measures the strength of the Coulomb repulsion. Here m is the electron mass. Very often the ratio $\eta = \epsilon_\infty/\epsilon_0$ $(0 < \eta < 1)$ is defined and its relation to U is given by,

$$U = \frac{\sqrt{2}\alpha}{1-\eta}, \tag{5.21}$$

where only $U > \sqrt{2}\alpha$ has the physical meaning. The formation of bipolarons is enhanced by larger values of α and smaller values of η. Another crucial factor is the dimensionality. The binding of two charges in 2D systems is favored over 3D systems. This is known for Frohlich interaction, which is not strong enough to compensate the Coulomb repulsion to create a bound state. Similar conclusions were given by Takada [49] from the weak-coupling limit with retarded interactions. The condition $E_{bip} < 2E_p$, (E_{bip} and E_p are the ground state energies for bipolaron and polaron, respectively) is the most common criterium for bipolaron stability. This condition is fulfilled if α is larger than the critical value $\alpha > \alpha_c$. In the context of the cuprates it was suggested [47] that in these materials the conditions for the bipolaron stability are fulfilled. In compounds based on La_2CuO_4 for a 3D Frohlich bipolaron $\alpha_c^{3D} = 6.8$, while for a 2D bipolaron is $\alpha_c^{2D} = 2.9$. This was based on the analysis of the phase diagram U vs α. Moreover, the bipolaron stability is fulfilled within a region defined by two lines: $U = 1.526\alpha^{2D}$ and $U = 1.537\alpha^{2D}$. Each line was inferred by data taken experimentally for ϵ_0 and ϵ_∞ in $YBa_2Cu_3O_7$ and La_2CuO_4. Though such region is narrow and created under the most optimistic values within the level of uncertainty in the error bars (see the discussion followed by J. Devreese in his review [44]).

5.3.4 Strong coupling Fröhlich bipolaron

According to A.S. Alexandrov [48] doped ionic crystals are characterized by poor screening of high-frequency optical phonons and they are more appropriately described by the finite-range Fröhlich charge-lattice coupling. These unscreened type of interaction provides a sufficient condition for the creation of a bipolaron. Moreover, besides the existence of light polarons, bipolarons would behave as superlight small bipolarons, which are much lighter than bipolarons in the Holstein-Hubard model. Next we sketch the condition for paired polarons in the case of strong long range electron-lattice interaction. Alexandrov proposed the next Hamiltonian written in the real space:

$$
\begin{aligned}
H &= \sum_{\mathbf{m}\neq\mathbf{n}} T(\mathbf{n}-\mathbf{m}) c^{\dagger}_{\mathbf{n}} c_{\mathbf{n}} + \frac{1}{2}\sum_{\mathbf{n}\neq\mathbf{n}} c^{\dagger}_{\mathbf{n}} c_{\mathbf{n}} c^{\dagger}_{\mathbf{m}} c_{\mathbf{m}} V_c(\mathbf{m}-\mathbf{n}) + \omega_0 \sum_{\mathbf{m}} (d^{\dagger}_{\mathbf{m}} d_{\mathbf{m}} + \frac{1}{2}) \\
&+ \omega_0 \sum_{\mathbf{m}\neq\mathbf{n}} g(\mathbf{m}-\mathbf{n})(\mathbf{e}\cdot\mathbf{e}_{\mathbf{m}\neq\mathbf{n}}) c^{\dagger}_{\mathbf{m}} c_{\mathbf{m}} (d^{\dagger}_{\mathbf{m}} + d_{\mathbf{m}}),
\end{aligned} \tag{5.22}
$$

where g is defined by Eq. (5.19). The Hamiltonian implicitly presents (infinite) Hubbard U that prohibits double occupancy and removes the need to distinguish the fermionic spin. In the non- or near-adiabatic limit and the strong electron-lattice coupling the kinetic energy is a perturbation. So if the Lang-Firsov canonical transformation[3] is used we obtain:

$$
Ep = \omega_0 \sum_{\mathbf{i}} g^2(\mathbf{i}-\mathbf{j})(\mathbf{e}\cdot\mathbf{e}_{\mathbf{i}-\mathbf{j}})^2. \tag{5.23}
$$

The polaron-polaron interaction is

$$
v(\mathbf{i}-\mathbf{j}) = V_c(\mathbf{i}-\mathbf{j}) - V_{ph}(\mathbf{i}-\mathbf{j}), \tag{5.24}
$$

where

$$
V_{ph}(\mathbf{i}-\mathbf{j}) = 2\omega_0 \sum_{\mathbf{i}} g(\mathbf{i}-\mathbf{j}) g(\mathbf{i}-\mathbf{j}')(\mathbf{e}\cdot\mathbf{e}_{\mathbf{i}-\mathbf{j}})(\mathbf{e}\cdot\mathbf{e}_{\mathbf{i}-\mathbf{j}'}). \tag{5.25}
$$

When V_{ph} exceeds V_c the full interaction becomes negative and polarons form pairs.

The original idea that a considerable mobility of bipolarons could be realized in the cuprates is confirmed in the work of Hague et al. [50]. Two varieties of motion were studied for the case of Fröhlich interactions on staggered geometries by means of a continuous Quantum Monte Carlo (QMC): a "crawling-like" and a "crab-like" motion. This type of result rules out the misconceptions that polarons might not exhibit high mobility because they are strongly bound to distorted lattice regions. Although it is true that, in order to have very short superconductivity coherence lengths in cuprates, a strong e-ph interaction is needed, the presence of the strong Coulomb repulsion helps to counterbalance it. As a result, the bipolaron mass is reduced.

[3] In principle the diagonalization is exact if $T(\mathbf{m}) = 0$. Hence, it is applied a unitary transformation given by $\widetilde{H} = e^{S} H e^{-S}$, where $S = \alpha \sum_{\mathbf{q},i} n_i [u_i(\mathbf{q}) d\mathbf{q} - H.c.]$ and is such that $S^{\dagger} = -S$. This approximation is used when the kinetic energy is smaller than the interaction energy and $\lambda > 1$. As a result, the ion are shifted to a new equilibrium position and the renormalized hopping is $\widehat{\sigma}_{ij} = T(\mathbf{m}-\mathbf{n})\delta_{SS'} \widehat{X}^{\dagger}_i \widehat{X}_j$. Here $\widehat{X} = e^{\sum_{\mathbf{q}} [u_i(\mathbf{q}) d\mathbf{q} - H.c.]}$ relates the transformed electronic operator $\widetilde{c}_i = c_i \widehat{X}_i$. See Lang, I.G. and Firsov Y.A. Zh. Eksp Teor. Fiz. **45**, 378 (1963).

5.4 Superconductivity in the cuprate oxides: The original concept

The strong JT distortion that perovskite oxides exhibit motivated Bednorz and Müller to start a search for materials with higher T_c. Perovskites, like $SrTiO_3$ and $LaAlO_3$ [51], had shown signs of SC, but with a rather low T_c. Such low T_c came as no surprise, since they exhibit low density of states at the Fermi level and, according to the Bardeen-Cooper-Schieffer (BCS) relation, a low critical temperature is expected:

$$k_B T_c = 1.14\hbar\omega_D \, e^{-1/N_F V}. \tag{5.26}$$

The formula relates, T_c with the e-ph pairing potential, V, of electrons near the Fermi energy level with N_F as their density of states. The Debye phonon cutoff is ω_D and represents the phonon involved in the process of pairing.

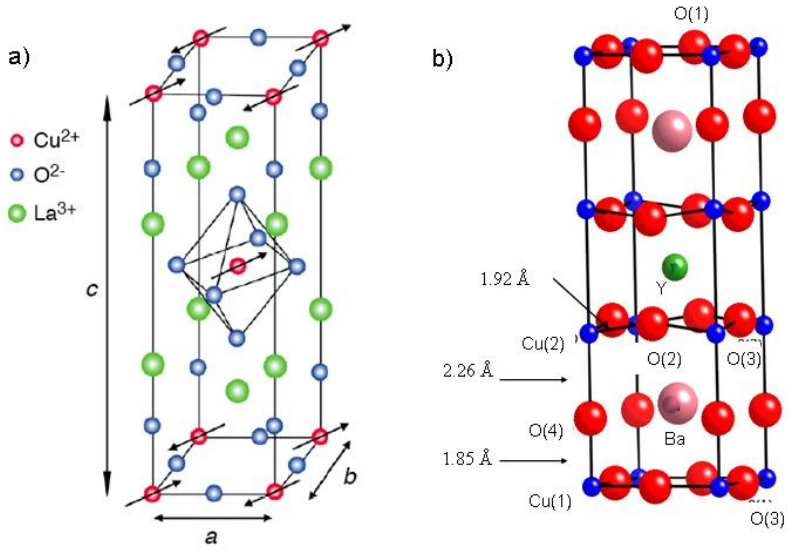

FIGURE 5.2: Two compounds of the family of ceramic oxides that under hole doping develop HTS. a) In La_2CuO_4, lanthanum is substituted by strontium or barium. The ion valences, the AF order, and the JT unit formed by the CuO_6 octahedron are shown. The anti-ferromagnetic order is shown as well (arrows placed at Cu ions). b) $YBa_2Cu_3O_{7-\delta}$ reaches HTS if oxygen is introduced into the Cu-O chains. Here is shown the doped oxygen occupying the upper and bottom chains of unit cell and denoted as O(1) are shown. The lattice constants for the unit cell along the three axis are $a = 3.81$ Å , $b = 3.88$ Å and $c = 11.64$ Å . Average Cu-O distances are indicated as well.

Nevertheless, following Müller and Bednorz, the e-ph interaction given by the strong JT effect in the CuO_6 octahedra (Fig. 5.2a) in combination with a perovskite layer, could be the right condition for increasing T_c. In this way they were guided by the idea of bipolaron superconductivity. Their experiments published in 1986 contained the highest T_c that had ever been reported before, $T_c = 39$ K [52]in a doped La_2CuO_4 system (Fig. 5.2a): $La_{1.85}Ba_{0.15}CuO_4$. The discovery opened a completely new horizon, and the cuprate oxides became some of the most studied materials.

One year later, due to the efforts of M. Wu, P. Shu et al. [53], T_c was increased to 93 K. The new record was achieved by a chemical substitution of Lanthanum by Yttrium, and the newest member in the family of HTS was $YBa_2Cu_3O_{7-\delta}$ (Fig. 5.2b); the optimal chemical composition was $YBa_2Cu_3O_7$. The highest T_c reached [54] was under hydrostatic pressure and belongs to the compound $HgBa_2Ca_2Cu_3O_{8+\delta}$ with $T_c = 168$ K.

5.5 Experimental evidences of polarons, lattice-charge segregation, and the isotope effect: the role of JT distortions

The first measurements of carriers with polaronic nature in the cuprates were reported at the end of 80s. The measurements included the photo-induced absorption and infrared reflectivity in La_2CuO_{4+x} and Nd_2CuO_{4-y} [55–57]. The idea was that with the assistance of absorbed photons polarons gain the ability to hop from one localized site to another. This picture was supported by the related theoretical studies of polarons and bipolarons [58].

At the same time there was an improvement of the methods probing the local lattice structure [59] as well as the dynamics of the local lattice motion [60]. Thus, high energy spectroscopy and EXAFS analysis provided valuable methods in the determination of inter-atomic local distances [61]. This contrasts with the traditional methods like X-ray diffraction that yields an average of the crystalline structure. EXAFS became a primordial tool for studying the local environment of the single CuO_6 octahedron, revealing anomalies in atomic distributions. EXAFS analysis showed that the Cu(1)-O(4) apical distance (Fig. 5.2b) in YBaCuO actually exhibits two distances, giving structural evidence of polarons in cuprates. The polarized X-rays along the *c*-axis were able to resolve two equilibrium distances of 1.822 Å and 1.954 Å for the Cu(1)-O(4), which differ from the average of 1.85 Å[59]. These type of results were relevant for the JT effect. Since EXAFS can measure differences between the CuO apical and CuO planar distances, it

can help to estimate the JT splitting and to determine wether the JT effect has to be treated as a pseudo JT effect. But, due to the time resolution of the technique, it cannot distinguish between dynamical and static JT distortions. Deeper conclusions from the EXAFS data came later on, when it was inferred that distorted domains coexist with undistorted domains at the scale of nanometers [13]. The materials subject of study were $La_{1.85}CuO_{4.1}$ and $La_{1.85}Sr_{0.15}CuO_4$. Here two distances were found on the Cu-O layer as well as c-axis. The double distances are interpreted as the coexistence of two regions of CuO_6 octahedra: one without deformation (16 Å of widths in the $La_2CuO_{4.1}$ and 14.5 Å in $La_{1.85}Sr_{0.15}CuO_4$) and a second region with distorted octahedron (8 Å of width in the $La_{1.85}CuO_{4.1}$ and 9.7 Å in $La_{1.85}Sr_{0.15}CuO_4$). All these results strongly suggest that the copper oxides are not homogenous materials. More intriguing results came when the Cu-O pair distribution showed a broadening within the SC region as the doping was increased and the temperature kept fixed at $T = 10$ K [62]. Similarly, EXAFS data which was collected at optimal doping shows an anomaly as the temperature approaches T_c [63]. Recently, the role of these lattice effects in the physics of the HTS was discussed in [64].

The rich interplay among time, energy and length scales has been successfully studied by a series of experiments using femto-second time domain spectroscopy [65–69]. The technique is suitable to study the process of pair formation. The advantage of the technique resides in its characteristic time scale, which is within the time span that a quasi particle (QP) requires to relax from the high energy state induced by a laser pulse to the low energy. In the results presented in [65, 66], the recombination time of the QP was attributed to the anharmonic life-time of the phonons that take part in the process. The technique also offers the opportunity to infer the length scale within which the process occurs and thereby exposes lattice-charge inhomogeneties [67]. In addition, the coexistence of localized and free electronic states was confirmed. This has particular importance, since it has revived the two-component models that were first proposed right after the discovery of HTS in the cuprates [32]. In references [65, 66] two different time scales of relaxation were reported. One appears at T_c and is associated with the SC gap, with a life-time ranging from 0.1 to 3 ps. The second component, with a shorter life time, is attributed to the (PG)[4] and the emergence of charge separation.

In addition, the improvement of scanning-tunneling microscopy (STM) in the last years allows to measure to the electronic density of states of some copper oxides, showing images with inhomogeneous charge distribution at the nanoscopic scale [71–74].

[4]The PG term refers to the very low electronic density of states existing in the hole doped superconductors. The term was coined in this way because actually is not the superconducting gap. Its formation begins at temperatures $T^* > T_c$. The insulating character of this gap is associated to electrons moving parallel to the Cu-O oxygen bonds, while electrons moving diagonally are free. Early measurements of electronic specific heat [70] gave the first clues of its existence.

The isotope effect remains one of the most direct criteria to discriminate whether the vibrational modes of the ions are the constituent mechanism for superconductivity. In the case of the cuprates special attention has been paid to substitution of O^{16} by O^{18}. The isotope shift detected in conventional superconductors persuaded Bardeen to establish the e-ph mechanism [75]. In contrast, the relevance of phonon interaction in cuprates has long been debated because of the negligible isotope effect on T_c [76–79]. However, advances in experimental techniques in recent years and carefully performed experiments have shown evidence of the isotope effect, but the signatures are not the usual ones as found in metals or alloys. Consequently, ceramic superconductors may also be regarded as unconventional superconductors in the sense that the isotope effect is present, but in a subtle way. Furthermore in the BCS theory the T_c dependence with the mass, M, of the ions involved in the phonon pairing is $T_c \approx M^{-\alpha}$ with $\alpha = 0.5$. It is known that deviations from this value may depend on the type of interatomic potentials. This could be, for instance, a double well minimum potential corresponding to a polaron motion of an ion moving between two equivalent positions or/and anharmonicity [80, 81]. Hence, the JT tunneling between two degenerate or nearly degenerate states may be intimately related to this form of polaron, and therefore deviations from $\alpha = 0.5$ should be expected.

One of the manifestations of the isotope effect is the huge isotope shift observed in the PG regime. Investigation by means of inelastic neutron scattering (INS) in $HoBa_2Cu_4O_8$ showed an isotopic shift in T^*: $\Delta T^* = -50$ K, here $\Delta T^* = T^*(O^{16}) - T^*(O^{18}) = (170 - 220)K = -50K$ [82]. In the case of $La_{1.81}Ho_{0.04}Sr_{0.15}CuO_4$ $T^*(O^{16}) = 110$ K and $T^*(O^{18}) = 70$ K, with a $\Delta T^* = -40$ K of isotopic shift [83]. The isotopic substitution was also performed for $Cu(Cu_{63} \rightarrow Cu_{65})$ showing no isotopic shift and therefore confirming that the displacements involving the oxygen ions are the relevant modes. Thus, the isotope effect that does appear at the PG region is strong evidence that the phonons, inhomogeneities and preformed pairs are linked [84].

Signatures of the isotope effect can be found in the theoretical and experimental studies of Kresin, Khasanov, H. Keller and Bussmann-Holder [85–88]. They showed that in analogy to the isotope effect on the superconducting transition temperature, the isotope effect on SC energy gap increases with decreasing gap magnitude. An equally interesting result was given by the isotopic shift of the magnetic transition temperatures at zero fields (μSR); the experiments were performed for undoped La_2SrCuO_6. Here it was also demonstrated that the lighter polaron carriers (corresponding to O^{16}) have the ability to break the AF order more easily than the heavy polarons composed by O^{18}. All these results fit into the particular interpretations made by Bussmann-Holder, Keller and Müller [89, 90], which are based on a two-component band model with electron-lattice interactions, where the nearest neighbors, the second and the third next-nearest

neighbor-hopping in the CuO layers as well as hopping between layers were considered. The same approach used in [89, 90] was applied for strain analysis. Because the strain changes the relative distance between oxygen and copper ions, one way to mimic the strain is through variation of hopping integrals. It was found that the combination of the nearest and the next-nearest neighbors hopping yields the optimal parameters for an enhancement of T_c. Thus, when the strain is taken into account, T_c reaches a maximum for intermediate values of the nearest and the next nearest neighbor hopping. Based on the isotope and strain effects they concluded that the Q_2 active JT mode has a prominent role in the SC properties. For recent reviews see [88, 91].

5.6 Formulation of the JT effect in the cuprates.

The problem of the JT effect in the solid state physics at dilute concentrations is similar to the local problem. Conceptually, it can be seen as an impurity center embedded in a crystal. In principle various active modes are present and in general each of the JT active modes can be studied individually. In the case of the cuprates or the manganites it is common to deal with the three dimensional character of the oxygens surrounding the Cu ion or the Mn ion. Alternatively one can take the two dimensional character. If the capital letters denote electronic states and the small letters the vibrational modes the CuO_4 or the MnO_4 cluster can be described as a $E\bigotimes(a_1 + b_{1g} + b_{2g})$ problem. E stands for the degenerate electronic state of the D_{4h} symmetry, and they are coupled to the asymmetric vibrational terms b_{1g} and b_{2g}. For instance, the electronic state may represent the Cu wave function with zx or zy symmetries. These states can be coupled to the b_{1g} mode. The b_{1g} displacement describes the simultaneous motion of two opposite oxygens displacing towards the Cu center, while the other two oxygens move away from it. This displacement is commonly called half-breathing mode, in contrast to the breathing mode, which occurs when the four oxygens undergo a totally symmetric displacement. If only the half-breathing mode is the subject of study, the problem is referred to as an $E \bigotimes b_{1g}$ problem and is the simplest model for holes with b_{1g} character moving along the CuO plane.

Conversely, the full CuO_6 octahedral or MnO_6 can be considered; then the JT problem becomes $E\bigotimes(a_1 + e)$ [42]. In contrast to the CuO_4 cluster, both the electronic states and the vibrational mode exhibit double degeneracy. The E term represents the $3z^2 - r^2$ and the $x^2 - y^2$ Cu orbital which form the electronic degeneracy. By this approach, the effect of the elongation along the crystallographic c axis can be added. The difference between the $3z^2 - r^2$ bond energy and the $x^2 - y^2$ bond energy gives the JT split energy, that sets the problem as either a pure JT effect or as a pseudo JT effect. However, as

we will see in the next sections, the fact that this unit is embedded in a crystal makes crucial modifications.

5.7 JT-paring and JT-cooperative phenomena

So far we only discussed isolated JT centers. The problem is more complex when the concentration of JT active centers is increased: The higher the doping, the larger the possibility that the JT centers start to interact and the assumption of two equivalent displacements in a JT center is no longer valid [92]. In other words, the presence of JT neighbors affects the degeneracy. This leads to the cooperative JT effect. In the simplest case this would happen if the centers are close enough and their respective lattice distortions overlap. Another type of cooperative interaction occurs when the JT centers are viewed as sources of virtual phonons that are being exchanged through the medium offered by the lattice.

5.7.1 Early attempts to describe JT polarons and JT-domains

We start saying that from a theoretical point of view the JT polaron concept has been used explicitly in the pseudogap physics of the copper oxides. For example in [93] R. Markiewicz proposed a possible explanation of this crossover region present in the phase diagram of the cuprates. He made the observation that the temperature and doping dependence of the pseudogap could be directly related to an intermediate step, which involves coupled JT centers, during the structural phase transition from a high-temperature tetragonal (HTT) phase to the low-temperature orthorhombic (LTO) phase and a low-temperature tetragonal (LTT) phase. It would be a sort of dynamical JT coupling among different octahedra mediated by planar oxygens.

We should also mention that due to the character of the JT effect one might intuitively anticipate that lattice instabilities would break the lattice symmetry locally and form domains. But any attempt to formulate a microscopic origin of JT paring should be able to reconcile different aspects, like the existence of mesoscopic JT domains, predict specific charge transport properties in the normal state and explain the superconductivity itself. The possibility of an attractive potential created by the anharmonic tunneling of JT distortions was already suggested in 1988 by Johnson [94, 95], and multi-JT interacting centers as a mechanism of JT nano structuring in 1997 by Moskvin [96]. A proposal which includes some of these elements is the one introduced by Bersuker and Goodenough [97]. Another work that includes the JT effect and stripes is found in the work of R. Markiewicz [98].

In the early 90s Shou and Goodenough explained their thermoelectric power measurements, made in a wide range of doping and temperature, through polaron interactions. The system under scrutiny was $La_{2-x}Sr_xCuO_4$, which facilitates the interpretation of the type of experiments they performed, because the material is single-layered [99]. The experiments provided data that approximated the size of the deformed region around the Cu ion. These clues lead Bersuker and Goodenough [97] to establish a more elaborate model, which utilizes the JT effect as a primordial mechanism to predict the heterogeneity, make an estimation of the polaron mobility, predict the temperature dependence of the resistivity and give some insights for achieving high T_c. They proposed to deal with the polaron domains within the pseudo JT scheme as a $(A_{1g} + B_{1g}) \bigotimes (a'_{1g} + a_{1g} + b_{1g})$ problem.

Within this scheme the energy of pairing is the difference between the energy of two interacting multimode JT polarons and the energy of two non-interacting single JT polarons. The symmetry of the JT interaction is crucial for paring; the relative position of the two holes gives rise to a pairwise potential which can be either attractive (pairing) or repulsive. The vibrational mode b_{1g} is responsible for this type of dependence; thus, while two b_{1g} distortions in the opposite direction lead to paring, two parallel distortions lead to antipairing. If several JT centers are allowed to interact, the model leads to cluster formation, with six polaron centers arranged in an antiferrodistortive fashion. More interesting is the fact that the clusters acquire a stripe shape. The model also predicts the most stable stripe configuration on the CuO_2 sheet. The authors concluded their work with an analysis of the motion of polarons occupying the edge of the formed cluster. The type of movement that the polaron develops is a crawling movement with a mobility of 1-10 cm^2/Vs.

5.7.2 JT paring model for describing inhomogeneities in the cupprates

A step forward in evaluation and implications of the JT effect is found in a series of publications by Mihailovič and Kabanov. The theory incorporates JT polaron interactions through the length of their lattice distortions. A JT Hamiltonian formulated either in real space [100] or equivalently in k space [101] embodies these ideas. The model incorporates the dispersion on the phonon mode. This contrasts with models that set $k = 0$ for the interaction. The model's aim is to achieve an inhomogeneous state that leads to SC. Some similarities are found with the model proposed in [97], in the sense that both consider an anisotropic interaction of the JT-strain type.

In order to discriminate all possible JT couplings, the model uses a group theory analysis of the electronic and vibration symmetries. The $La_{2-x}Sr_xCuO$ in [100] and $YBa_3CuO_{7-\delta}$

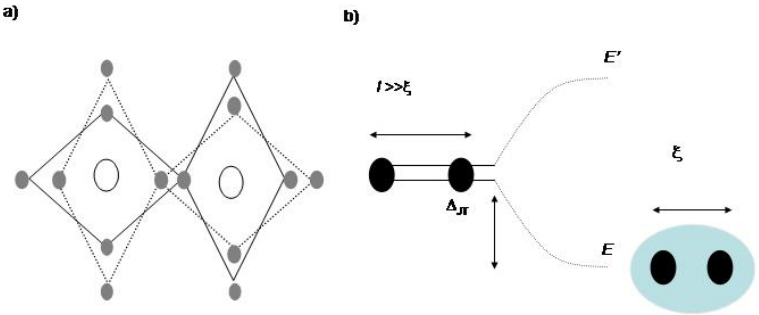

FIGURE 5.3: Schematic representation of: a) an inter-site JT-polaron and its two equivalent ways of pairing (white and grey circles represent copper and oxygen sites respectively); b) two electrons in a doubly degenerated energy level and separated one from each other by distance l. The pair of electrons lowers their energy by Δ_{JT}, when they interact through lattice instability of JT type. Here ξ represents the coherence length of a pair, while E' and E are two energies.

in [101] are the two chosen materials to exemplify the concepts. For the former material the analysis is done in k space. Here, in order to define the effective range of coupling and the shifting from the $k = 0$ point, Mihailovič and Kabanov paid attention to magnitude of the phonon anomalies which occur at finite k. So pairs should have a peak of coupling near $k_0 = (\pi, 0, 0)$ effectively extended over $\gamma = \Delta k$. It also gives the width of the distribution of inter-carrier distances within the interacting pair. This is related to the average size of the deformation around each particle in the real space γ^{-1}. Hence an interaction which causes an anomaly at this point in k-space will lead to a distortion of the lattice whose symmetry is reduced from tetragonal symmetry (D_{4h}) within a volume of size $l = \pi/k_0$. The interaction at k_0 thus creates mesoscopic areas (or objects), whose symmetry is reduced (ultimately C_{2v} once larger objects corresponding to a new phase are formed), while the undistorted surroundings have a higher symmetry (D_{4h}).

The Hamiltonian in real space formulation is given in [101] as

$$H_{JT} = H_1 + H_2 + H_3 + H_4, \tag{5.27}$$

given by the next four terms:

$$H_1 = \sum_{\mathbf{n},\mathbf{l},s} \sigma_{0,\mathbf{l}}(n_x^2 + n_y^2) g_0(\mathbf{n})(b^\dagger_{\mathbf{l}+\mathbf{n}} + b_{\mathbf{l}+\mathbf{n}}), \tag{5.28}$$

$$H_2 = \sum_{\mathbf{n},\mathbf{l},s} \sigma_{3,\mathbf{l}}(n_x^2 - n_y^2) g_3(\mathbf{n})(b^\dagger_{\mathbf{l}+\mathbf{n}} + b_{\mathbf{l}+\mathbf{n}}), \tag{5.29}$$

$$H_3 = \sum_{\mathbf{n},\mathbf{l},s} g_2(\mathbf{n})\sigma_{1,\mathbf{l}}(n_x n_y)(b^\dagger_{\mathbf{l}+\mathbf{n}} + b_{\mathbf{l}+\mathbf{n}}), \tag{5.30}$$

$$H_4 = \sum_{\mathbf{n},\mathbf{l},s} S_z \sigma_{2,\mathbf{l}}(n_x^2 + n_y^2) g_2(\mathbf{n})(b^\dagger_{\mathbf{l}+\mathbf{n}} + b_{\mathbf{l}+\mathbf{n}}), \tag{5.31}$$

where

$$g_i(\mathbf{n}) = g_i \frac{\exp[(-a/l)\sqrt{n_x^2 + n_y^2}]}{n_x^2 + n_y^2}, \tag{5.32}$$

g_i are the coupling constants and a is the lattice constant. The function $g_i(\mathbf{n})$ describes the spatial dependence of the effective interaction. $\mathbf{l} = (l_x, l_y)$ represents lattice sites and $\mathbf{n} = (n_x, n_y)$ with $|n_x|, |n_y| \geq 1$; b and $b^\dagger$ represent phonon operators. l is the range of the charge-lattice interaction. S_z is the component of the local spin. The Pauli matrices (σ_i, $i = 1, 2, 3$) assure the splitting of the degenerated electronic states. The first term couples to symmetric distortion throughout the 2D unit matrix σ_0. The next two terms describe coupling between electrons in degenerate electronic states and the lattice of xy and $x^2 - y^2$ symmetry respectively. The last term represents spin coupling of the z-component of spin S_z to the electronic states. In this way non-degenerate electronic levels coupling to phonons and spins can only give rise to a symmetric (s-wave) deformation, while coupling to doubly degenerate electronic states (of E_g symmetry in the high symmetry group) can give rise also to an anisotropic d-wave like interaction in addition to the symmetric one. Because the interaction is between electrons in degenerate states and phonons and spins, the latter may be viewed as a finite-k or mesoscopic Jahn-Teller effect.

The Hamiltonian defined by equation 5.27 can lead to formation of bound inter-site pairs in a region with a coherence length of ξ (figure 5.3). In principle, as doping is increased clusters or even stripes can be formed. However, such type of regions need to be the stabilized by the countereffects of the kinetic energy and the LRCI. The latter is precisely the next element introduced in the model.

5.7.2.1 The 2D Jah-Teller-Coulomb model as a lattice gas model

In the Hamiltonian proposed by Mihailovič and Kabanov, the JT analysis was made throughout equation 5.27 at selected points Σ of the BZ. The real space JT-paring Hamiltonian that only considers b_{1g} symmetry is given by:

$$H_{JT-pol} = \omega_0 \sum_{\mathbf{i}} b^\dagger_{\mathbf{i}} b_{\mathbf{i}} - g \sum_{\mathbf{i},\mathbf{r}} f(r)\sigma_{3,\mathbf{i}+\mathbf{r}}(r_x^2 - r_y^2)(b^\dagger_{\mathbf{i}+\mathbf{r}} + b_{\mathbf{i}+\mathbf{r}})n_{\mathbf{i}}, \tag{5.33}$$

where $\sigma_{3,\mathbf{i}}$ is the Pauli matrix describing the electronic doublet at site $\mathbf{i}$, $f(r) = (r_x^2 - r_x^2)f_0(r)$. g is the strength of the e-ph coupling with the phonon with frequency ω and $f_0(r)$ is the effective spatial variation of the interaction. The interaction is assumed to be short ranged with the characteristic interaction radius r_0, $f_0(r) \approx \exp(-r/r_0)$.

In order to deal with this Hamiltonian as a lattice gas model of polarons, we need to introduce a harmonic phonon field, $\omega \sum_{\mathbf{i}} \Theta^2_{\mathbf{i}}/\sqrt{2}$. With the field defined as $\Theta_{\mathbf{i}} = b_{\mathbf{i}} + b^\dagger_{\mathbf{i}}$, the minimum energy will correspond to the distortion:

$$\Theta_{\mathbf{i}} = -\frac{\sqrt{2}g}{\omega} \sum_{\mathbf{r}} f(r)\sigma_{3,\mathbf{i}+\mathbf{r}}, \tag{5.34}$$

Now we substitute (5.34) into (5.33) and using pseudospin notation for a lattice gas model we obtain the final form of the short range term,

$$V_l(\mathbf{i}-\mathbf{j}) = V_{JT}(\mathbf{i}-\mathbf{j})S^z_{\mathbf{i}} S^z_{\mathbf{j}}, \tag{5.35}$$

with,

$$V_{JT}(\mathbf{m}) = \frac{g^2}{\omega} \sum_{\mathbf{i}} f(\mathbf{i})f(\mathbf{m}+\mathbf{i}), \tag{5.36}$$

Here $\mathbf{m} = \mathbf{i} - \mathbf{j}$ is a lattice vector. We have denoted as S^z the two components of the electronic doublet and an empty site, where $S^z = -1, 1$ represents the two-fold degenerated state and $S^z = 0$ an empty site. The configurations are depicted in Figure 5.4

The extension of the lattice interaction can be chosen by m, For example if $m = |\mathbf{i}-\mathbf{j}| = a$, with a as the lattice constant, the interaction is fixed to the nearest neighbors. The LRC for two charged particles is defined by

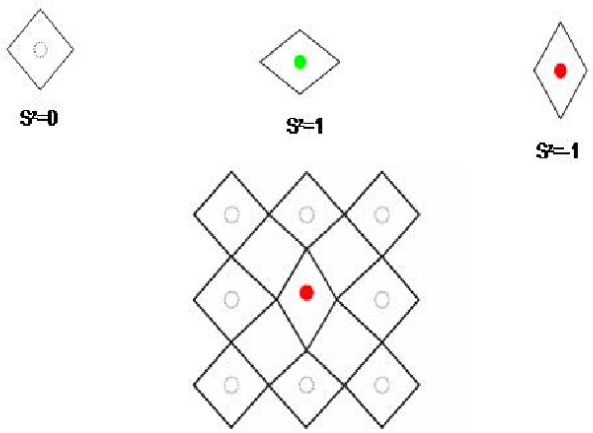

FIGURE 5.4: Three top figures: Pseudospin configurations representing two equivalent JT distortions of the CuO_6 plaquete ($S^z = 1$, $S^z = -1$) and the undistorted plaquette ($S^z = 0$). The distortions are mapped onto the CuO_2 plane as a rhombic distortion of the CuO_2 unit. Bottom figure: Breaking of the CuO_2 lattice symmetry due to a local distortion created by a single polaron with pseudospin configuration $S^z = 1$.

$$V_{e-e}(\mathbf{i}-\mathbf{j}) = V_C(\mathbf{i}-\mathbf{j})Q_{\mathbf{i}}Q_{\mathbf{j}}. \tag{5.37}$$

Where $Q_{\mathbf{i}} = (S^z_{\mathbf{i}})^2$ highlights the fact that electrostatic interaction only depends on charge occupation, while the part V_c of the Coulomb potential is given by

$$V_C(\mathbf{i}-\mathbf{j}) = \frac{e^2}{\epsilon_0 a|\mathbf{i}-\mathbf{j}|}. \tag{5.38}$$

Here ϵ_0 is the static dielectric constant. Then the full *JTC* model in the pseudospin representation is:

$$H^{LG}_{JTC} = \sum_{\mathbf{i}}^{occ.}\sum_{\mathbf{j}}^{occ.}(-V_{JT}(\mathbf{i}-\mathbf{j})S^z_{\mathbf{i}}S^z_{\mathbf{j}} + V_C(\mathbf{i}-\mathbf{j})Q_{\mathbf{i}}Q_{\mathbf{j}}). \tag{5.39}$$

Indexes $\mathbf{i}$ and $\mathbf{j}$ run across all sites.

Chapter 6

Monte Carlo simulations I: Patterns and DOS

6.1 Introduction

In order to find the arrangement of JT-polarons with the lowest free energy, as given by 5.39, and its single particle DOS, we use the Monte Carlo method. Here we explain how concepts of probabilistic theory merge with statistical physics to create this reliable method. We start reviewing two concepts related with theory of probability: Markovian chain and importance sampling. Later we will sketch the improvement which can be achieved by simulated annealing. Afterwards, we make connection with the way we compute the average energy and DOS as well as detailed discussion to the their physical interpretation.

The importance of the cooperative JT effect for our purposes is that it gives rise to inhomogeneity when it is counterbalanced by long range repulsive forces. The viewpoint presented here is that above a certain temperature T* a gas of weakly interacting polarons exists and below this temperature polarons form bound charge agglomerations. In this manner, the gap opening in the DOS is related to the *PG* energy. This gap coincides with the emergence of inhomogeneities. The proposal is that upon doping the charges self-organize due to forces exerted by the electron-phonon interactions of the JT type.

6.2 Elements for Monte Carlo simulations.

6.2.1 Monte Carlo Integrator

Let us first review the way Monte Carlo approximates the value of an integral $\int f(\mathbf{x})d\mathbf{x}$ [1]:

$$\frac{1}{\Omega}\int f(\mathbf{x})d\mathbf{x} \approx \overline{f} = \frac{1}{N}\sum_{i}^{N} f(\mathbf{x}_i), \tag{6.1}$$

where Ω is the integration volume and $\overline{f}$ represents the average value. The right side of the equation takes N sample numbers, $\mathbf{x}_i$, equally distributed. In order to have a better approximation to $\overline{f}$, by means of the sum, we try to take N as large as possible. But this method is not ideal, since the variance defined by

$$\mathrm{Var}f = \frac{1}{\Omega}\int [f(\mathbf{x})]^2 d\mathbf{x} - [\Omega^{-1}\int f(\mathbf{x})d\mathbf{x}]^2 \approx \frac{N}{N-1}(\overline{f^2} - \overline{f}^2), \tag{6.2}$$

is large. This is due to the fact that the function is often strongly peaked in a small region of the phase space. This is also reflected in the error of the Monte Carlo simulation which is defined by

$$\Delta = \sqrt{\frac{Varf}{N}} \approx \sqrt{\frac{\overline{f^2} - \overline{f}^2}{N-1}}. \tag{6.3}$$

This crude method is improved if the concept of importance sampling is included. The sample points are now taking from a probability distribution $p(x)$: $\int p(\mathbf{x})d\mathbf{x} = 1$. Using these points the sampling is done according to:

$$< f >= \frac{1}{\Omega}\int f(\mathbf{x})d\mathbf{x} = \frac{1}{\Omega}\int \frac{f(\mathbf{x})}{p(\mathbf{x})}p(\mathbf{x})d\mathbf{x} \approx \frac{1}{N}\sum_{i}^{N}\frac{f(\mathbf{x}_i)}{p(\mathbf{x}_i)}. \tag{6.4}$$

and the Monte Carlo error is

$$\Delta = \sqrt{\frac{Varf/p}{N}}. \tag{6.5}$$

[1] The next derivations follow the lecture notes of Matthias Troyer in [102].

A very important consideration is to choose p with a suitable form. Whenever possible, p should have a similar form as f. In this way f/p is nearly constant and the variance small.

A natural choice for the weighting function p is often given in the case of phase space integrals or sums, where an observable O is averaged over all configurations in $\mathbf{x}$ space where the probability of the configuration is $p(\mathbf{x})$. The phase space average $\langle O \rangle$ is:

$$\langle O \rangle = \frac{\int O(\mathbf{x}) p(\mathbf{x}) d\mathbf{x}}{\int p(\mathbf{x}) d\mathbf{x}}. \tag{6.6}$$

Here we want to make importance sampling with distribution $p(\mathbf{x})$.

6.2.2 Markov chain and the Metropolis algorithm

Historically, Stainslaw Ulam proposed first a probabilistic phase space solution for the type of problem posed by Eq (6.6) [103]. Later on, the method was improved by Metropolis *et al.* with smart sampling [104, 105].

In general problems with arbitrary distributions p, it is not possible to create a p-distributed configurations directly. Instead a Markov process can be used.

A Markovian chain is a process that connects a series of configurations $\mathbf{x}_i : \mathbf{x}_0 \rightarrow \mathbf{x}_1 \rightarrow \mathbf{x}_2, ...\mathbf{x}_{N-1}$ by a probability rate [102]. A transition matrix probability allows a state $\mathbf{x}$ to go to another states $\mathbf{y}$ in one step. It is denoted as $W_{\mathbf{xy}}$. As the sum of probabilities to move from state x to any other state is one, the column of the matrix W are normalized: $\sum_{\mathbf{y}} W_{\mathbf{xy}} = 1$. A consequence is that the Markov process conserves the probability. Another consequence is that the largest eigenvalue of the transition matrix is 1 and the corresponding eigenvector with only positive entries is the equilibrium distribution which is reached after a large number of Markov steps.

In order to obtain a distribution of probabilities $p_{\mathbf{x}}$ two important condition must be fulfilled:

- Ergodicity. Any configuration $\mathbf{x}$ can be accessed from any other state $\mathbf{y}$ after a finite number of Markov steps. This means that for all $\mathbf{x}$ and $\mathbf{y}$ there exists a positive integer $n < \infty$ such that: $(W^n)_{\mathbf{xy}} \neq 0$.
- Detailed balance. This actually is some sort of flow equation which tells us how the probability of one state $\mathbf{x}$ is transferred to another state $\mathbf{y}$ at each step on

the Markovian chain. The probability distribution $p^n_{\mathbf{x}}$ changes at each step of the Markov process:

$$\sum_{\mathbf{x}} p^n_{\mathbf{x}} W_{\mathbf{xy}} = p^{n+1}_{\mathbf{y}} \tag{6.7}$$

but converges to the equilibrium $p_{\mathbf{x}}$. This equilibrium distribution $p_{\mathbf{x}}$ is an eigenvector with eigenvalue and the equilibrium condition

$$\sum_{\mathbf{x}} p_{\mathbf{x}} W_{\mathbf{xy}} = p_y. \tag{6.8}$$

must be fulfilled. It is easy to see that the detailed [102] balance condition

$$\frac{W_{\mathbf{xy}}}{W_{\mathbf{yx}}} = \frac{p_{\mathbf{y}}}{p_{\mathbf{x}}}. \tag{6.9}$$

is sufficient.

In our notation for the lattice gas model the Markovian chain is a set of pseudo-spin configurations $\{S^z_i\}_j$. Each $\{S^z_i\}_j$ is linked to the previous configuration in a Markovian sense.

We now construct W explicitly. Let $W^0_{\mathbf{xy}}$ be the probability of proposing a transition from $\mathbf{x}$ to $\mathbf{y}$ and $a_{\mathbf{xy}}$ the probability of accepting it. $1-a_{\mathbf{xy}}$ corresponds to the probability of rejecting the move, With $W^0_{\mathbf{xy}}$ and $a_{\mathbf{xy}}$ we build $W_{\mathbf{xy}}$ with:

$$W_{\mathbf{xy}} = \begin{cases} W^0_{\mathbf{xy}} a_{\mathbf{xy}} & \text{if } \mathbf{y} \neq \mathbf{x}; \\ W^0_{\mathbf{xx}} + \sum_{z \neq x} W^0_{\mathbf{xz}} (1 - a_{\mathbf{xz}}) & \text{if } \mathbf{y} = \mathbf{x}. \end{cases}$$

Let us assume,

$$a_{\mathbf{xy}} = F(\frac{W^0_{\mathbf{yx}} p_y}{W^0_{\mathbf{xy}} p_x}). \tag{6.10}$$

Since

$$a_{\mathbf{yx}} = F(\frac{W^0_{\mathbf{xy}} p_{\mathbf{x}}}{W^0_{\mathbf{yx}} p_{\mathbf{y}}}) = F(\frac{1}{\frac{W^0_{\mathbf{yx}} p_{\mathbf{y}}}{W^0_{\mathbf{xy}} p_{\mathbf{x}}}}). \tag{6.11}$$

The detailed balance condition reduces to:

$$\frac{F(R)}{F(1/R)} = R, \text{ where } R = \frac{W^0_{\mathbf{yx}} p_{\mathbf{y}}}{W^0_{\mathbf{xy}} p_{\mathbf{x}}}. \tag{6.12}$$

There are many possible choices. The Metropolis algorithm is based on the choice:

$$F(R) = \min(R, 1). \tag{6.13}$$

The observable $\langle O \rangle$ may now be estimated with:

$$\langle O \rangle \approx \frac{1}{N} \sum_{i}^{N} O(\mathbf{x}_i). \tag{6.14}$$

In our case, we are interested in averages of the form,

$$< A > \approx \frac{1}{Z} \sum_{j} A_j e^{-E_j/k_B T}, \tag{6.15}$$

where A_i is the value of A in the pseudo spin configuration $\{S_i^z\}_j$ and energy $E_j = \exp(-\beta H(\{S_i^z\}_j))$. Here H is the Hamiltonian given by equation 5.39 and $Z = \sum_j \exp(-E_j/k_B T)$ is the standard definition of the partition function. Therefore when generating points in configuration space, they should follow the probability $P_j = e^{-E_j/k_B T}/Z$. Next we follow the Metropolis scheme.

At this points we have introduced all the ingredients for the our MC simulations. The way it is related with Hamiltonian in equation 5.39 and its pseudo spin notation, can be summarized as follows. Choose randomly a state $\{S_i^z\}_j$ and create a set of states as a Markovian chain. Apply the Metropolis algorithm to generate the Markovian chain. Averaging is performed after some MC steps. This is due to the fact that the initial states are far from energy equilibrium.

A trial move consists in a random selection of a single occupied site and the attempt to move onto random unoccupied site. Pseudospin must be considered as well, for that reason a random nonzero pseudospin must be selected for the unoccupied state.

The pseudo-code for the Metropolis algorithm is:

1. Create at random an initial state.
2. Choose randomly a site $\mathbf{i}$ with the pseudo spin $S^z_{\mathbf{i}} \neq 0$.
3. Perform a trial move to a random site $\mathbf{j}$ with $S^z_{\mathbf{j}} = 0$.
4. Calculate the energy change ΔE.
5. Generate a random number r such that $0 < r < 1$.
6. If $r < \exp(-\Delta E/k_B T)$, accept the move, otherwise keep the previous state.
7. Go to (2).

6.2.3 Simulated annealing

Last we briefly explain how we can improve the evaluation of averages by implementing the so called simulated annealing method. In its original formulation made by Kirkpatrick et al. [106], the simulated annealing algorithm was used to find a global minimal configuration of a given system.

In our case we are not interested in finding the global minimum. Rather we are searching for a "good" set of states for "reliable" averages. By means of the simulating annealing procedure, we use fast convergence at higher T to obtain better starting configurations $\{S^z_i\}_j$ at low T. This also enables fast convergence as T is reduced. In addition, this method allows us to follow the behavior of the system as a function of T.

6.3 Monte Carlo solution

In this section we calculate the thermodynamic properties of the inhomogeneous phase within the JTC model as well as the single particle DOS. We treat the 2D JTC model, introduced in 5.7.2.1, by the statistical tools given in the last section. As a result, the DOS will allow us to better characterize and estimate the behavior of the charged particles when they form clusters. For instance, it will complement the analysis of electrical conductivity presented in the next chapter. Therefore, we investigate characteristic patterns and DOS by computing MC averages of the lattice gas model.

Let us first define the total energy in terms of the site occupation. The total energy is proportional to the product of number of particles $n_{\mathbf{i},\sigma}$ at site $\mathbf{i}$ interacting with $n_{\mathbf{j},\sigma'}$ particles at site $\mathbf{j}$, depending on the pseudospin configuration ($\sigma \in \{-1, 1\}, \alpha =$

$1, \beta = -1$). From equations (5.36) and (5.37) we can define in terms of $V_{\sigma,\sigma'}(\mathbf{i}-\mathbf{j}) = -V_{JT}(\mathbf{i}-\mathbf{j})\sigma\sigma' + V_C(\mathbf{i}-\mathbf{j})\sigma^2\sigma'^2$, where $\sigma, \sigma' \in \{-1, 1\}$, the many body Hamiltonian:

$$H_{JTC} = \frac{1}{2}\sum_{\mathbf{i}\neq\mathbf{j}}\sum_{\sigma,\sigma'} V_{\sigma,\sigma'}(\mathbf{i}-\mathbf{j}) n_{\mathbf{i},\sigma} n_{\mathbf{j},\sigma'}. \tag{6.16}$$

Particles take either σ or β pseudospin values. We also introduced the lattice-pseudspin occupation number, $n_{\mathbf{i},\sigma} \in \{1, 0\}$, where $n_{\mathbf{i}} = 1$ if a particle is at site $\mathbf{i}$ with the pseudospin α and $n_{\mathbf{i},\sigma} = 1$ if a particle is at site $\mathbf{i}$ with the pseudospin β; otherwise $n_{\mathbf{i},\sigma} = 0$.

Then, the single particle energy,

$$\epsilon_{\mathbf{i},\sigma} = \frac{\delta H_{JTC}}{\delta n_{\mathbf{i},\sigma}} \tag{6.17}$$

is written as,

$$\epsilon_{\mathbf{i},\sigma} = \sum_{\mathbf{j}\neq\mathbf{i}}\sum_{\sigma'} V_{\sigma,\sigma'}(\mathbf{i}-\mathbf{j}) n_{\mathbf{j},\sigma'}. \tag{6.18}$$

In this way, the DOS for particles is calculated from the following formalism. Particles with a σ pseudo-spin configuration present a DOS given by

$$N_{p,\sigma}(\epsilon) = \sum_{\mathbf{j}}^{n_{j,\sigma}\neq 0} \delta(\epsilon - \epsilon_{\mathbf{j},\sigma}), \tag{6.19}$$

where index $\mathbf{j}$ runs across all particles with the pseudospin σ.

Therefore, the total DOS for occupied states is the sum of the DOS of the two possible pseudospin values:

$$N_p(\epsilon) = N_{p,\alpha}(\epsilon) + N_{p,\beta}(\epsilon). \tag{6.20}$$

Similarly we can define the DOS for holes, if we let to run the site index across unoccupied states. Henceforth we denote those equivalent DOS as $N_h(\epsilon)$, $N_{h,\alpha}(\epsilon)$ and $N_{h,\beta}(\epsilon)$. Finally the total DOS is defined as

$$N(\epsilon) = N_h(\epsilon) + N_p(\epsilon). \tag{6.21}$$

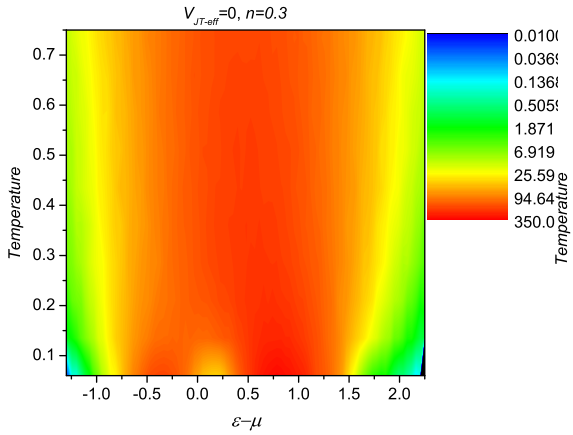

FIGURE 6.1: DOS for $V_{JT-eff} = 0$ as the temperature is lowered from $T = 0.9$ to $T = 0.07$ for doping $n = 0.3$. A single gap is formed at $\epsilon - \mu \approx 0$.

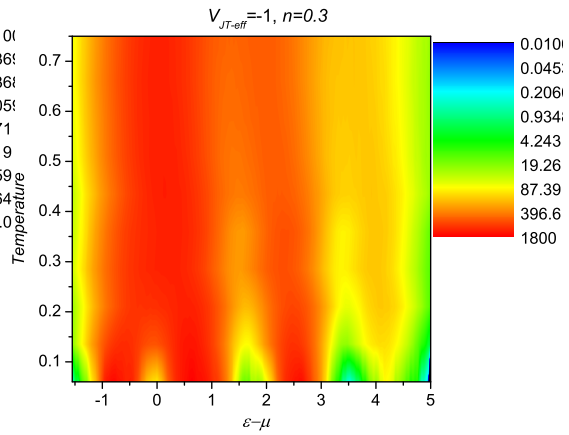

FIGURE 6.2: DOS for $V_{JT-eff} = -1$ as the temperature is lowered from $T = 0.9$ to $T = 0.07$ for doping $n = 0.3$. Three gaps are formed at $\epsilon - \mu \approx 0, 1.6$ and 3.5.

To investigate the relation between the average energy, DOS and charge distribution, we first performed MC simulations for $V_{JT-eff} = -1$ and $V_{JT-eff} = 0$. The former case corresponds to a competition between JT interaction and the LRC repulsion; while in the latter case the particles are interacting only by the LRC potential. Here $V_{JT-eff} = \frac{V_{JT}(\mathbf{m})}{V_C(\mathbf{m})}$, with $|m| = a$, is the interaction to nearest neighbors (JT polarons at distance a) given by Eq. (5.36), and $V_C = e^2/\epsilon_0 a$ as given by (5.38). We set $V_{JT}(\mathbf{m}) = 0$ for $|m| > a$. The comparative results are shown in Figures 6.1-6.4. The energies are measured with respect to the chemical potential, μ. The first two plots (6.1 and 6.2) show the DOS as the temperature is lowered. Suppression of DOS in form of gaps is observed at low T. For $V_{JT-eff} = -1$, gaps appear at higher temperatures ($T \approx 0.45$) than the single gap for $V_{JT-eff} = 0$ ($T \approx 0.15$). In Figures 6.3 and 6.4 snapshots and a detailed description of DOS are shown for two temperatures: $T = 1.0$ and $T = 0.07$. We observe that the emergence of charged clusters coincides with the opening of multiple gaps when $V_{JT-eff} = -1$. These charged domains are formed by two type of ferrodistortive configurations compatible with the coupling $V_{eff-JT} = -1$ (the energy of JT coupled polarons is the lowest when their distortions have the same lattice direction). The only gap observed for $V_{JT-eff} = 0$ is related to the Coulomb gap [107]. In general the patterns and DOS depend on the doping, as we will shortly see. For a convergence analysis see Appendix C.

In Fig. 6.5 the total DOS, $N(\epsilon)$, is plotted for $V_{JT-eff} = 0, -0.5, -1, -1.5$. Here we observe the following features. For $V_{JT-eff} = 0$ the width of the gap at half doping is the largest. It is attributed to the commensurate effect.

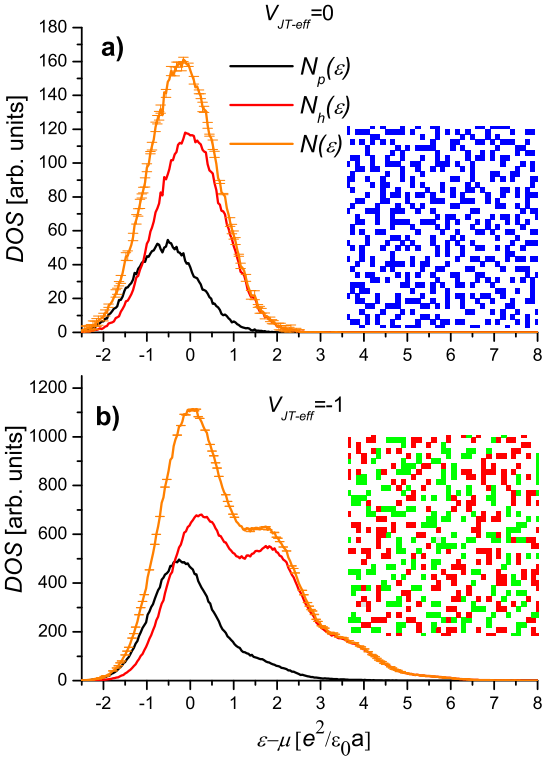

FIGURE 6.3: DOS and snapshots of charge distribution (insets) at $T = 1$ and $n = 0.3$. a) $V_{JT-eff} = 0$ and b) $V_{JT-eff} = -1$. a) Charged particles (blue dots) interact only by LRCI. b) The JT coupling and the LRCI are present. The two types of charged particles are marked according to the pseudo-spin notation of the lattice gas model: red ($\sigma = \alpha$) and green ($\sigma = \beta$). Both couplings, $V_{JT-eff} = 0$ and $V_{JT-eff} = -1$ present random distribution of charges and one maximum peak in the DOS.

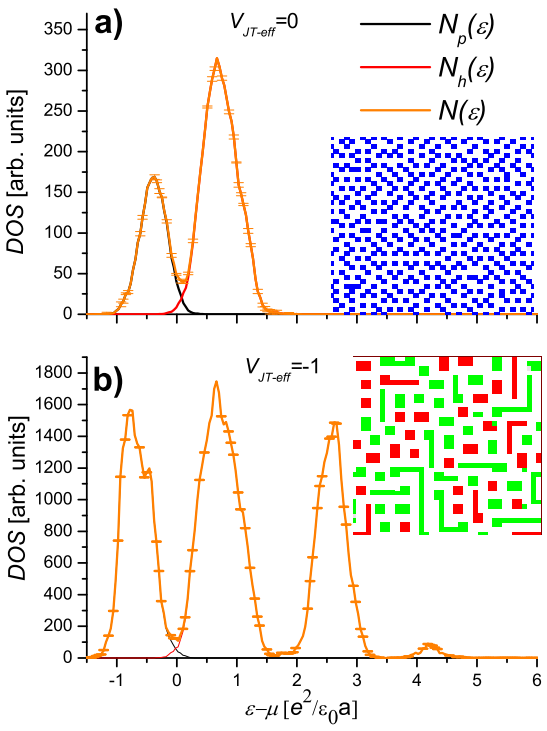

FIGURE 6.4: a) DOS and snapshots of charge distribution (insets) at $T = 0.07$ and $n = 0.3$. Plots in panels a) and b) obey the same interaction and notation as in panels a) and b) of Fig. 6.3, respectively. a) The system has a homogenous distribution of particles. The formation of a single gap is attributed to the LRCI. b) Competitive JT and LRC forces lead to multiple gaps as well as JT clusters. The clusters correspond to two equivalent JT-polarons domains. Red and green regions represent the two $\sigma = \alpha, \beta$ JT-clusters.

In order to track the origin of the gaps we follow the next arguments. Firstly, the Coulomb gap is inherently present because charges always interact by the LRC potential, regardless of their positions. In contrast, according to how we define the JT potential, gaps associated with lattice interactions, originate only from the particles that are the nearest neighbours (NN). Moreover a single particle placed next to a second can lower or increase the energy by V_{JT}, depending on the pseudospin, so it can contribute to DOS at two different energies. In order to identify them, we first analyze the two σ components for hole states together with their charge distribution in Fig. 6.6. At low n, in addition to the Coulomb gap, one expects at least two gaps as result of the JT interaction. As n increases the cluster sizes grow. At the same time the clusters start to bend or split in

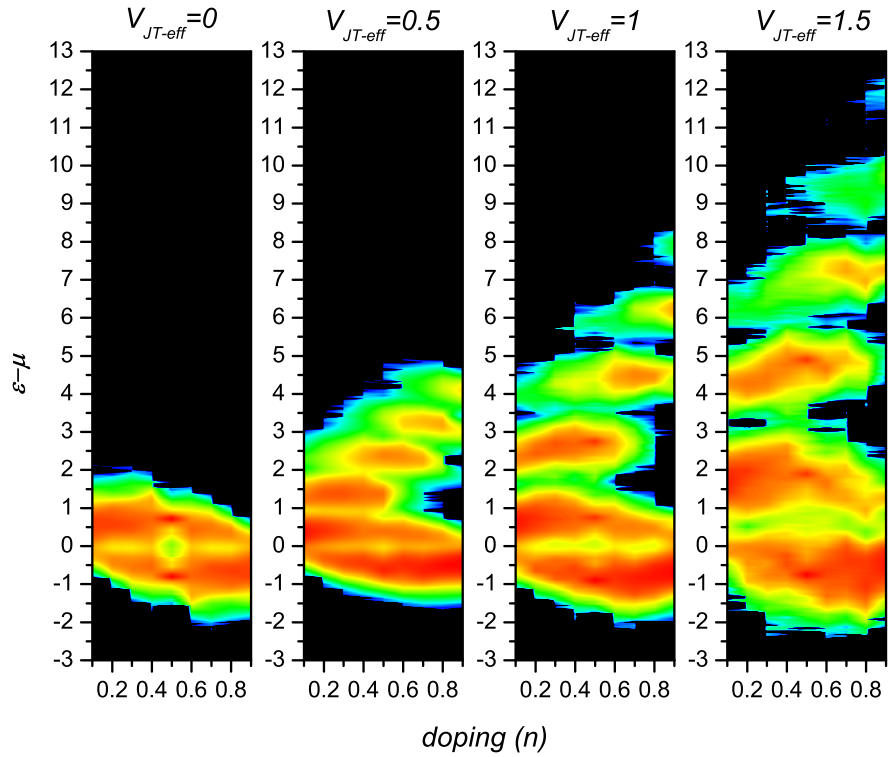

FIGURE 6.5: DOS for a wide range of n as the strength of the JT coupling is increased. The intensity follows a blue-red color variation. For a given JT coupling, the number of gaps and their position in the energy scale depends on n. At high or low n the lowest energy gap closes for $V_{JT-eff} < 1.5$.

order to minimize the LRC energy. These intersticial hole regions create the conditions for double bounded (anti-bounded) particles. Thus, adding a particle ($\epsilon - \mu > 0$) near a bent cluster will increase or reduce the energy by $2V_{JT}$ (it is in contact with two JT polarons). Further increase of n leads to larger number of JT centers to interact. At this range of doping three interacting JT centers may contribute to DOS at $\pm 3V_{JT}$. On the top of that, some domains might be only one-lattice site apart, leading to a similar condition. Here adding a partcile will contribute to DOS at three energy level: $-2V_{JT}$, $2V_{JT}$ or 0 if it is placed between two domains with opposite ferrodistortive order.

Above $n = 0.5$, the system undergoes to an orbital ordering and the equivalency of $\sigma = \alpha, \beta$ is suppressed. Let us now focus in the developing of the orbital ordering in Fig. 6.7. For that purpose we select $n = 0.1$ and $n = 0.9$. At the highest temperatures disorder is observed at both dopings. The same figure also shows that occupied and unoccupied states overlap. Though for $n = 0.9$ the DOS is more extended. At $T \approx 2$ the onset of the orbital ordering is seen for $n = 0.9$ ($\sigma = \alpha$ corresponds to red regions in

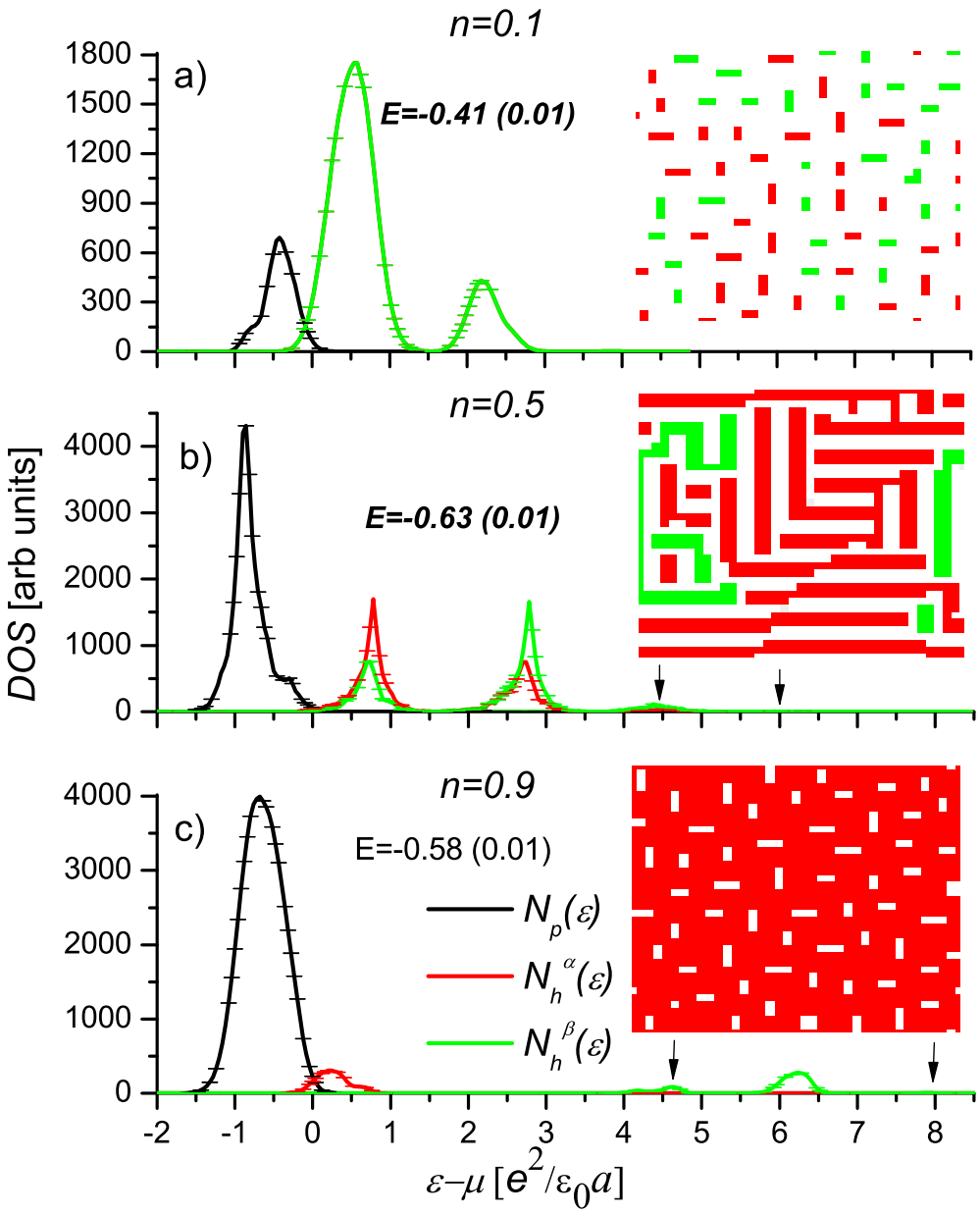

FIGURE 6.6: Contribution to DOS by $\sigma = \alpha, \beta$, pattern formations and average energy (E) for three concentrations with $V_{JT-eff} = -1$. At low n, the equal contribution to DOS from holes with $\sigma = \alpha, \beta$ states is seen in the perfect overlap of their DOS. At $n = 0.5$ stripes give place to five peaks (the small ones are marked with arrows); the commensurate effect is observed as sharp peaks. At $n = 0.9$ the system is in orbital order ($\sigma = \alpha$) and the degeneracy is lifted.

charge distribution and red curves in the DOS). With further decrease of the temperature to $T \approx 1$ the overlap of α and β in the unoccupied states vanishes. It is consistent with the fact that orbital ordering is almost completed. The widest gaps are regarded as the energy difference of JT-polarons having the the opposite orbital state. In principle the number of JT interactions can be three of four, which is the number of polaron neighbours. Similarly, for $n = 0.1$ the Figure 6.7e shows that charges remain disordered and with a complete overlap of their DOS (the hole curves overlap the particle peak). At the lowest temperature phase separation is achieved for $n = 0.1$ and $n = 0.9$. In addition for $n = 0.9$ the system has completed the orbital ordering. So upon doping the collective JT and LRC interactions are manifested in the presence of peaks. This is precisely what the figure 6.5 shows with all the different gap and peaks in the DOS.

The above analysis does not provide an accurate identification of the Coulomb gap since both interactions, JT and LRC, were set at similar magnitude. Because the lattice interactions contributes only for NN particles it would be desirable to separate the contribution of NN empty sites to the hole DOS. For this purpose we now perform a decomposition of the hole DOS. The DOS for NN states, $N_{JTC}(\epsilon)$, uses the following single hole energy:

$$N_{JTC}(\epsilon) = \sum_{\mathbf{i},\sigma}^{unocc} \delta(\epsilon - \epsilon_{\mathbf{i},\sigma}), \tag{6.22}$$

where $\mathbf{i}$ runs over all unoccupied states for which $\min(|\mathbf{i} - \mathbf{j}|) = a$ with $\mathbf{j}$ running over all occupied states.

$$N_{C}(\epsilon) = \sum_{\mathbf{i},\sigma}^{unocc} \delta(\epsilon - \epsilon_{\mathbf{i},\sigma}), \tag{6.23}$$

where $\min(|\mathbf{i} - \mathbf{j}|) > a$ with $\mathbf{j}$ running over all occupied states.

In Fig. 6.8 we show the results for N_{JTC} and N_C. The JT coupling leads to splitting of $N_{JTC}(\epsilon)$ and $N_C(\epsilon)$. This is observed in the shifted peaks of Fig. 6.8b and 6.8c. On other hand, since the number of NN increases as n is increased, the pure Coulomb peak fades away.

Before turning to more detailed analysis of how the JT coupling modifies the DOS, we prove the equivalency between V_{JT} and $-V_{JT}$ couplings. This is depicted in figure 6.9. The equivalency in the DOS is clearly shown for the case $V_{JT-eff} = 1$ and

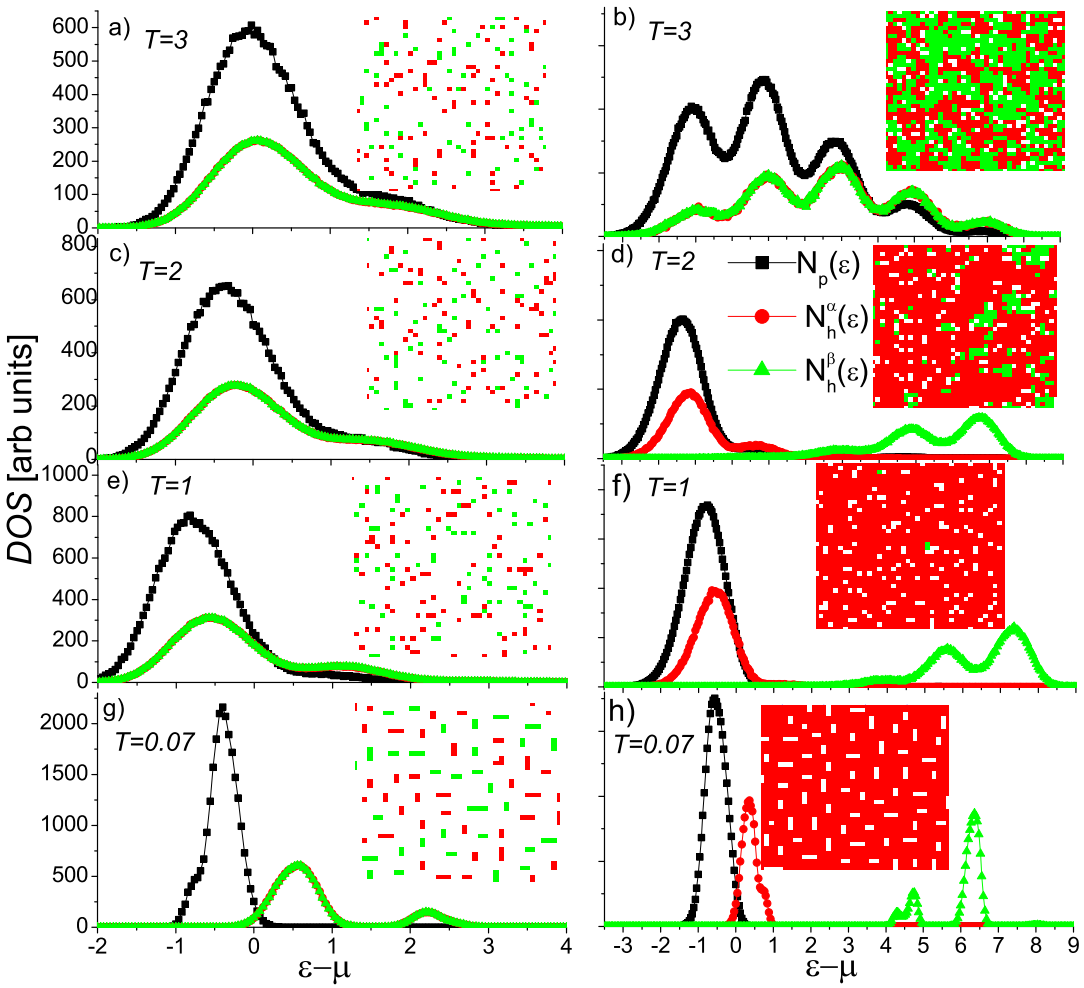

FIGURE 6.7: Developing of DOS and charge ordering (insets) as the temperature, T, is lowered for $n = 0.1$ (left panels) and $n = 0.9$ (right panels). Suppression of DOS is either due to cluster formation or suppression of one orbital state. Red regions in charge distribution and red curves in the DOS correspond to $\sigma = \alpha$, which is the low-T orbital polarization.

$V_{JT-eff} = -1$. The major difference is the way JT-polarons arrange. They are arranged in ferrodistortive domains for $V_{JT-eff} = -1$ and anti-ferrodistortive domains for $V_{JT-eff} = 1$.

Lastly, we illustrate the level of complexity which can emerge in our model above half-filling where the orbital ordering is triggered. We have also seen variation in shape of the patterns as function of V_{JT-eff}. Now we study the case where in addition to the nearest neighbor interaction, we extend it to the next nearest neighbors. We will use a ferrodistortive coupling for the former and an antiferrodistirtive for the latter.

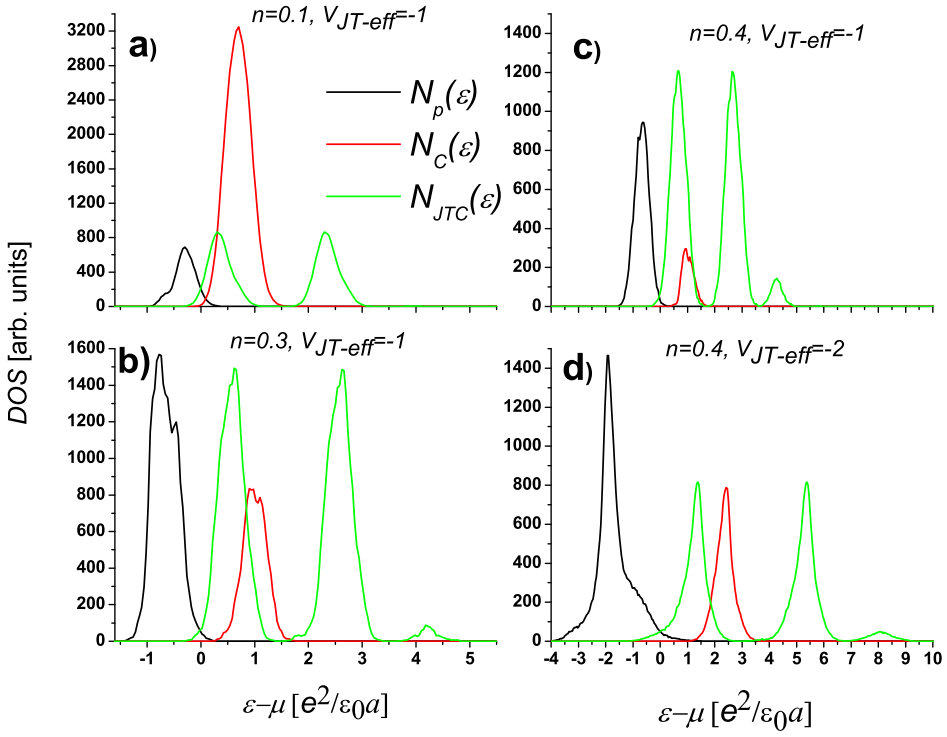

FIGURE 6.8: Decomposition of DOS into NN and non-NN states, denoted as $N_{JTC}(\epsilon)$ and $N_C(\epsilon)$ respectively. In a), b) and c) $V_{JT-eff} = -1$ and is observed that the first gap is made up by a pure Coulomb gap and the first energy order JT gap. In d) the Coulomb and the JT peaks are shifted. The sequence on panels a), b) and c) follows the disappearance of the pure Coulomb gap.

Henceforth we denote them as $V_{JT-eff}(\mathbf{m}) = -1$, $|m| = a$, and $V_{JT-eff}(\mathbf{m}) = 1$, $|\mathbf{m}| = \sqrt{2}a$ respectively. We are interested in the final configuration if some holes are introduced. We address this issue by using 80 percent doping or equivalently $n = 0.2$ of hole doping. Result of the MC simulations for two temperatures ($T = 1$ and $T = 0.07$) are given in Fig. 6.10. Two aspects define this set of parameters. 1) Orbital ordering precedes the charge ordering. 2) At low temperatures two distinctive type of stripes emerge. One is composed of holes aligned diagonally, while the second is made out of two orbital states orientated vertically. The two coexisting orders create a distinctive DOS. Interesting by itself is the fact that within the DOS of occupied sites three gaps have developed. Moreover, the DOS for unoccupied and occupied states are almost symmetric. These are new features not seen in the previous cases.

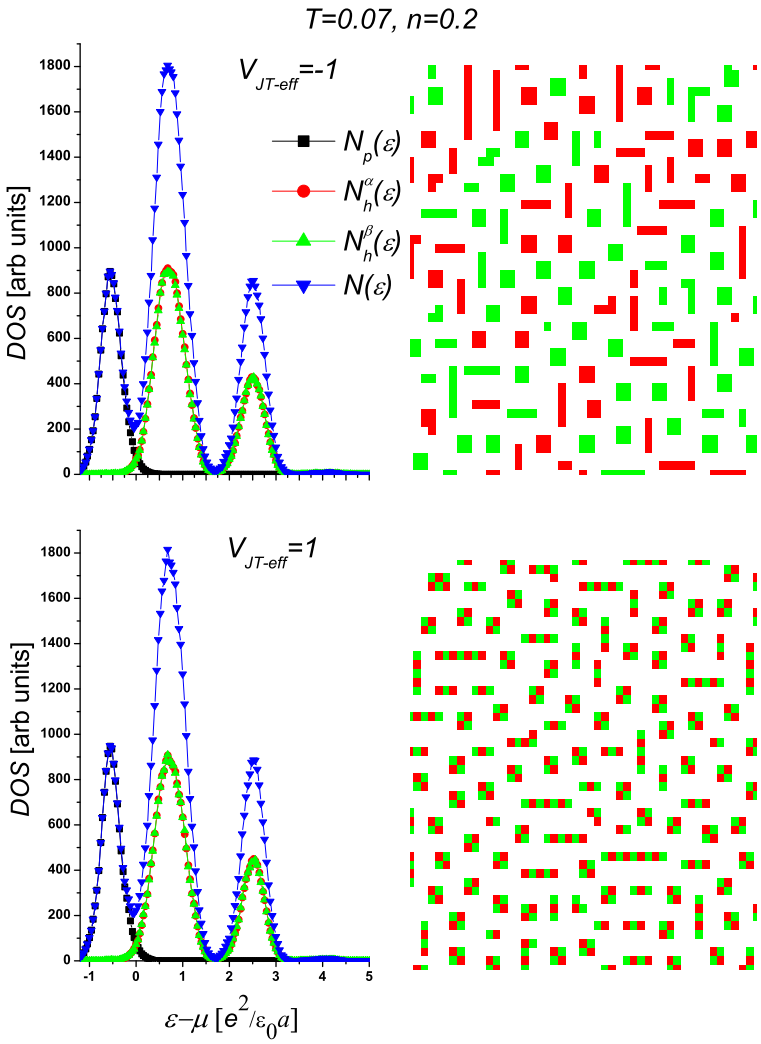

FIGURE 6.9: Two charge-lattice-orbital arrangements when particles are coupled by $V_{JT-eff} = -1$ (upper panel) and $V_{JT-eff} = 1$ (bottom panel). Both present identical DOS, even the type of domain are equal in shape and size. The major difference is found in internal orbital ordering inside the charge domains. While in the former ordering is ferrodistortive, in the latter is anti-ferrodistortive.

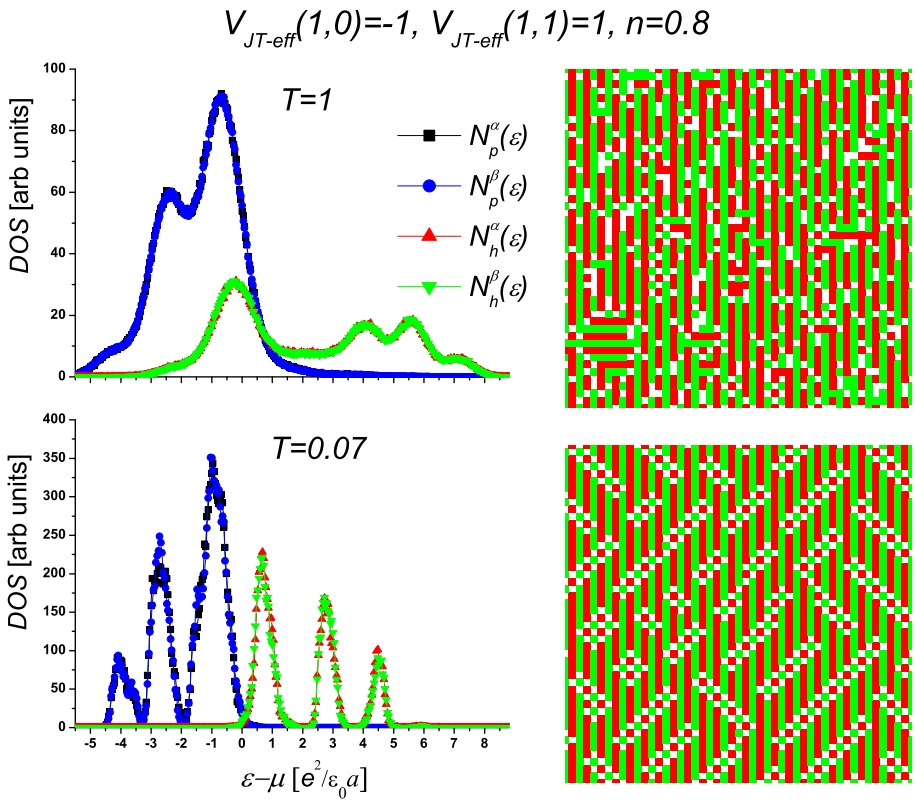

FIGURE 6.10: Charge-orbital phase transition for a coupling defined by $V_{JT-eff}(1,0) = -1$ and $V_{JT-eff}(1,1) = 1$. Doping was set to $n = 0.8$. At intermediate temperatures, $T = 1$, the leading ordering is orbital (upper panel). Subsequent lowering of the temperature, $T = 0.07$, gives place to hole-charge ordering. So at the same time there are an alternation of vertical regions made by the two orbital states and hole-striped domains arranged in a diagonal fashion.

6.4 Conclusions

In this chapter we showed that the particle self organization opens a series of gaps in DOS. According to our simulations, more than one gap can appear with increasing doping at low temperature. The lowest energy gap includes the energy of pair breaking of a single bipolaron, while higher order gaps correspond to two, three or four frustated bonds, as the number of particles in a cluster is increased. This is supported by the increasing size of stripes with doping which give as a result larger population of the nearest neighbor sites. The lowest energy gap is expected to have a strong influence on the electrical conductivity (see also next chapter) and its position is always near the Fermi level. We could identify that this gap also has some Efros-Shklovskii gap character, which is a typical Coulomb effect present in systems with localized electrons [82]. We sugest that the gap is related to the pseudogap observed in the high-T_c materials.

Chapter 7

Monte Carlo simulations II: polaron and bipolaron conductivity

7.1 Introduction

Another important property to investigate in the JTC model are the contributions of polaron and bi-polarons to the electrical conductivity. We are interested in their behavior as a function of temperature and doping. For this purpose we calculate single polaron and bi-polaron conductivity following a variable range hopping (VRH) scheme. In the previous two chapters we defined the JT-pairing as one element for driving phase separation. Likewise, we assumed the same mechanism for creating bipolarons. The concept of coupling of two fold degenerated electronic levels to local lattice modes at finite wave vector, as defined by the Hamiltonian in Eq. (5.40), remains. We have already discussed in chapter five the possible relevance of these effects to the properties of the cuprates. We return to this point in section (7.2) and more specifically in section (7.5) where we briefly review how the VRH has been used in the cuprates and manganites. We dedicate section 7.3 in this chapter to the formulation of the VRH. In particular the steps made by Mott which lead to his extensively used formula. In this way, the reader would be in a better position to understand the results we present.

We start by making some general remarks regarding the VRH. In Mott's original hypothesis [108], a particle is localized due to the interference of its wave-function created by the random distribution of atoms (in the Anderson sense). In a further step, Mott considered non-interacting particles and a constant DOS at the Fermi level, E_f. In our case, we have proven that short and long range potentials lead to multiple gaps. One

of them always opens at the chemical potential μ. In this sense, the approach we will present in this chapter is closer to the study of charged gases by Efros and Shklovskii [107]. They found that the Coulomb interaction creates a suppression of DOS at the Fermi level (exciton gap). So the procedure we present can be regarded an extension on the applicability of the VRH to systems with two different spatial ranges of interaction.

7.2 Jahn-Teller polarons as charge carriers

The first numerical results from a strictly quantum mechanical calculation for JT polarons and bipolarons were given a few years ago. Applying a quantum Monte Carlo algorithm, P. Kornilovitch [109] calculated the energy of the ground state, the DOS and the effective mass of a single JT polaron, and compared them with the computed values of a Holstein polaron. The two types of polarons showed similar behavior, except at the intermediate and strong coupling, where the JT polaron was lighter and developed a peaked DOS. In 2000, Y. Takada published an analytical paper in which he proved that JT polarons should be lighter due to the fact that the vertex corrections are less effective in JT polarons than in Holstein polarons [110]. However, one year after Takada's publication an analytical work carried out by H. Barentzen [111] showed that such differences in the two types of polarons may not be as pronounced as it was predicted in [110]. Similarly, for the one-dimensional case a comparative study of JT polarons and Holstein polarons was made by Shawish, Bonča et al. [112]. They used an advanced algorithm to compute the optical conductivity, the effective mass and the spatial extension. In addition, they included the strong Hubbard term for electrons placed either in the same orbital or different orbital. The results in the strong coupling regime showed that the JT interaction reduce the effective mass of the polarons and bi-polarons, while at weak coupling the two types of polarons display no differences. The same tendency as a function of coupling was observed in the radial extension of the polarons.

Due to the nature of the numerical techniques applied in some of these studies, the results are valid at $T = 0$. Since we will use a semi-classical approach we cannot access such regime. Nevertheless, we have the advantage to investigate a wider range of temperature and doping.

7.3 The variable range hopping

The VRH theory has its origin in the problem of conductivity in non-crystalline materials [113]. Since periodicity is absent in the atom arrangements of such systems the canonical

band theory cannot be applied. In crystalline materials a finite DOS at the Fermi level implies that conductivity, σ, tends to a finite value as T goes to zero. In contrast in a non-crystalline material, though presenting a degenerated electron gas and a finite DOS at the Fermi level, do not have a finite σ. This class of systems required a new approach.

Historically, Mott's work helped to establish the basis of a consistent model. The clues for the unusual behavior of conductivity came from experiments performed in doped semiconductors. Back then the problem was known as the impurity band conductivity. In general the experiments showed an unusual temperature dependence of $\sigma = \sigma' \exp(-\epsilon/kT)$, where σ' depends strongly on the concentration and ϵ is characteristic activation energy. At high concentrations the material presented the metallic behavior and ϵ was zero. Mott pointed out that it is possible to define a critical energy, E_c (mobility edge), which divides electrons that are strongly localized from those which are delocalized.

The VRH regime is dominated by electron hopping activated by phonons [113]. Let us denote as R the hopping distance between two atomic sites, and $\epsilon = \epsilon_i - \epsilon_j$ the energy difference between the two energy states. The energy is of the order of the bandwidth, $\epsilon \approx 1/R_0^3 N(E_F)$, where R_0 is the average distance between neighbors. Then, 1) the hopping is enhanced by the overlap of the atomic wave functions separating the sites and 2) the energy enters as a Boltzamn distribution in the hopping probability: $e^{-\epsilon/k_B T}$. The probability of hopping in both directions of the applied electric field E is:

$$P = \omega_{ph} e^{-2\alpha R - (\epsilon \pm eRE)/k_B T}, \tag{7.1}$$

and the current is

$$j = 2eRk_B T N(E_F)\omega_{ph} e^{-2\alpha R - \epsilon/k_B T} \sinh(eRE/k_B T). \tag{7.2}$$

If $eRE \ll kT$, then

$$\sigma = j/E = 2e^2 R^2 \omega_{ph} N(E_F) e^{-2\alpha R - \epsilon/k_B T}. \tag{7.3}$$

Following Mott, the optimal distance for charge hopping must be found by the minimization of the expression in exponent of Eq. 7.3. This optimized R is the distance that particles hop at a given T. As a consequences there are $4\pi(R/a)^3/3$ available sites. Hopping will be favorable for those states which have the lowest activation energies. For the given sites this happens at:

$$\epsilon = \frac{3}{4\pi R^3 N(E_F)}. \tag{7.4}$$

The averaged distance is given by the ratio:

$$\overline{R} = \frac{\int^R r^3 dr}{\int^R r^2 dr} = \frac{3R}{4}. \tag{7.5}$$

In this way the the probability of hopping is modified to

$$P = \omega_{ph} e^{-2\alpha\overline{R} - \epsilon/k_B T}. \tag{7.6}$$

Since we are searching for the maximum value of expression 7.3, we focus in the exponential argument,

$$\frac{3\alpha R}{2} = \frac{9}{4\pi N(E_F) R^3 k_B T}, \tag{7.7}$$

which is obtained after some substitutions. Minimizing over R, we obtain the optimal value

$$R = \sqrt[4]{\frac{3}{2\pi\alpha N(E_F) k_B T}}. \tag{7.8}$$

with the hopping distance 2/4 of this. From here we obtain the well known formula for VRH conductivity:

$$\sigma = e^2 N(E_F) \overline{R}^2 \omega_{ph} e^{-B/T^{1/4}}, \tag{7.9}$$

where $B = B_0(\alpha^3/k_B N(E_f))^{1/4}$ and $B_0 = 2(3/2\pi)^{1/4} = 1.66$. Typical values for B_0 are within the range from 1.7 to 2.5.

7.4 Correlated hopping in the variable range hopping scheme

Inclusion of the long range Coulomb interaction leads to the opening of the Efros-Shkolvskii Coulomb gap and a modified temperature dependence of the conductivity compared to the VRH model [114]. There have been increasing debates about the role

of multi-electron hopping conductivity. Tielsen and Schreiber have performed extensive calculations and came to conclusion that the many-electron hopping processes become dominant at low temperatures [115], which was also supported by simulations [116]. Later, these results were challenged by Tsigankov and Efros [117] who argued that a different choice of hopping rates leads to a substantial suppression of the two-particle contribution. More recently [118] it was shown that if one assumes more general hopping rates, the many-particle contribution to the conductivity may remain important at low temperatures. Thus the many-particle contribution to the conductivity of doped semiconductors and insulators, particularly at low temperatures remains controversial and limits our understanding of the transport not only in doped polar semiconductors, but also doped cuprates (including high-temperature superconductors) [66], doped manganites [9] and many other materials [119] where the electron-phonon interaction is intermediate or strong.

7.5 Variable range hopping in manganites and cuprates

Two type of materials which are good candidates for our formalism are cuprates and 2D manganites. In the past the VRH conductivity has been applied to both systems. In the former material at very low doping [120–124] while in the latter at intermediate doping [125–127]. The justification of the low dimensionality of our simulations is found in the planar nature of such materials.

In the cuprates, ever since earlier measurements [120, 121], the VRH scheme was proposed as a possible explanation of the anomalous conductivity at dilute concentration. Later on, the connection between doped holes following VRH and weakened of AF correlation was pointed out in [122]. The applicability of the VRH for engineering electronic devices, based on non-superconducting $YBa_2Cu_3O_{7-\delta}$, was envisioned in [123, 124]; in this new field effect transistors, the VRH plays an important role for describing localized charges.

In manganites proposals that relate the colossal magneto resistance and the VRH conductivity are found since the middle of the 90's. For instance measurement of resistivity in ref. [125] shows a typical VRH dependence upon substitution of rare-earth trivalent cations, **L** (Y, Dy, Yb, Gd), into $La_{1-y-x}\mathbf{L}_xCa_yMnO_3$. Similarly, the relevance of the JT effect in the semiconducting-like behavior was highlighted in mixed-valance manganites:$(La_{0.7}Ca_0.3)MnO_3$ [126] and at half-doping in the bilayer manganite $LaSr_2Mn_2O_7$ [127].

7.6 Monte Carlo solution

Although the VRH scheme usually is used with extrinsic disorder, we need to clarify this issue. In this regard, even in the case of absence of extrinsic disorder, the long range Coulomb interaction by itself may give the condition of disorder in electron liquids. This in turn leads to localization. The applicability of this theory is also justified by the glassy ground state demonstrated by previous simulations. Therefore we start with localized states. Moreover, we assume the mobility of JT polarons by means of a diffusive mechanism.

The single particle hopping rate between an occupied site $\mathbf{i}$ with pseudospin α to an empty site $\mathbf{j}$ with the resulting pseudospin β is given by:[109]

$$\gamma^{sp}_{\mathbf{i}\alpha,\mathbf{j}\beta} = \gamma_0 e^{-\alpha r_{\mathbf{ij}}} \begin{cases} e^{-\frac{\Delta_{i\alpha,j\beta}}{T}} ; \Delta_{i\alpha,j\beta} > 0 \\ 1 \qquad\quad : \Delta_{i\alpha,j\beta} \leq 0 \end{cases}, \tag{7.10}$$

where $\Delta_{\mathbf{i}\alpha,\mathbf{j}\beta} = \Delta H(\mathbf{i}\alpha \rightarrow \mathbf{j}\beta) - E x_{\mathbf{ij}}$ is the dimensionless many body energy difference between the final and initial states in the presence of an external electric field, E, applied along the x-axis. T is the temperature and $\gamma_0 \exp(-\alpha r_{\mathbf{ij}})$ the transition probability with $r_{\mathbf{ij}} = |\mathbf{j} - \mathbf{i}|$ and $x_{\mathbf{ij}} = j_x - i_x$. For a given system configuration,$\{S^z_{\mathbf{m}}\}$, the total dimensionless instantaneous current is the sum over all possible hops:

$$i^{sp} = \sum_{\mathbf{i}\alpha} {\sum_{\mathbf{j}\beta}}' x_{\mathbf{ij}} \gamma^{sp}_{\mathbf{i}\alpha,\mathbf{j}\beta}, \tag{7.11}$$

where the first sum runs over all occupied states with $S^z_{\mathbf{j}} \neq 0$ and the second over all empty sites with $S^z_{\mathbf{j}} = 0$ with both possible final pseudospin states, $\beta = \pm 1$. Since only the hops with $\Delta_{\mathbf{i}\alpha,\mathbf{j}\beta} > 0$ contribute to the net current the formula simplifies in the limit of the vanishing electric field to,

$$i^{sp} = N_{eff} \mu_{sp} E \approx \gamma_0 \frac{E}{T} \sum_{\mathbf{i}\alpha} {\sum_{\mathbf{j}\beta}}' x^2_{\mathbf{ij}} e^{-\alpha r_{\mathbf{ij}}} e^{-\frac{\Delta H(\mathbf{i}\alpha \rightarrow \mathbf{j}\beta)}{T}}, \tag{7.12}$$

where N_{eff} is the total number of particles/holes [1] and μ_{sp} the dimensionless single polaron mobility. The second sum runs only over the final states with $\Delta H(\mathbf{i}\alpha \rightarrow \mathbf{j}\beta) > 0$.

[1] For fillings where more than half of the sites are occupied we use the hole-polaron mobility for convenience so N_{eff} represents the number of holes in the system.

A bipolaron hop is a second order process [117] where a bipolaron $\langle \mathbf{i}\alpha, \mathbf{i}'\alpha' \rangle$ hops to $\langle \mathbf{j}\beta, \mathbf{j}'\beta' \rangle$ via the virtual dissociated states $\langle \mathbf{j}\beta, \mathbf{i}'\alpha' \rangle$ and $\langle \mathbf{i}\alpha, \mathbf{j}'\beta' \rangle$. The probability for such process is given by [117] :

$$\gamma^{bp}_{\langle \mathbf{i}\alpha,\mathbf{i}'\alpha' \rangle \langle \mathbf{j}\beta\mathbf{j}'\beta' \rangle} = \gamma_0^{bip} e^{-\alpha(r_{\mathbf{ij}}+r_{\mathbf{i}'\mathbf{j}'})} \begin{cases} e^{-\frac{\Delta \langle \mathbf{i}\alpha,\mathbf{i}'\alpha' \rangle \langle \mathbf{j}\beta,\mathbf{j}'\beta' \rangle}{T}} ; \Delta_{\langle \mathbf{i}\alpha,\mathbf{i}'\alpha' \rangle \langle \mathbf{j}\beta,\mathbf{j}'\beta' \rangle} > 0 \\ 1 \qquad\quad : \Delta_{\langle \mathbf{i}\alpha,\mathbf{i}'\alpha' \rangle \langle \mathbf{j}\beta,\mathbf{j}'\beta' \rangle} \leq 0 \end{cases}, \tag{7.13}$$

where $\langle \mathbf{i}\alpha, \mathbf{i}'\alpha' \rangle$ denotes the nearest neighbors and,

$$\Delta_{\langle \mathbf{i}\alpha,\mathbf{i}'\alpha' \rangle \langle \mathbf{j}\beta,\mathbf{j}'\beta' \rangle} = \Delta H(\langle \mathbf{i}\alpha, \mathbf{i}'\alpha' \rangle \rightarrow \langle \mathbf{j}\beta, \mathbf{j}'\beta' \rangle) - E(x_{\mathbf{ij}} + x_{\mathbf{i}'\mathbf{j}'}). \tag{7.14}$$

Tsigankov and Efros [117] argued that the hopping probability is suppressed when the distance between particles within the hopping pair is large, which reduces the bi-particle conductivity by orders of magnitude. This is not an issue in our case since the size of our bipolarons is restricted to one lattice constant.

The total bipolaron instantaneous current for a given system configuration in the limit of vanishing electric field is therefore similar to the single polaron case,

$$i^{bp} = N_{eff} \mu_{bp} E \approx \gamma_0^{bp} \frac{E}{T} \sum_{\langle \mathbf{i}\alpha,\mathbf{i}'\alpha' \rangle} {\sum_{\langle \mathbf{j}\beta\mathbf{j}'\beta' \rangle}}' (x^2_{\mathbf{ij}} + x^2_{\mathbf{i}'\mathbf{j}'})^2 e^{-\alpha(r_{\mathbf{ij}}+r'_{\mathbf{ij}})} e^{-\frac{\Delta H(\langle \mathbf{i}\alpha,\mathbf{i}'\alpha' \rightarrow \mathbf{j}\beta,\mathbf{j}'\beta' \rangle)}{T}} \tag{7.15}$$

Here again the first sum runs over all occupied bipolarons and the second over all possible unoccupied bipolaron states with $\Delta H = (\langle \mathbf{i}\alpha, \mathbf{i}'\alpha' \rangle \rightarrow \langle \mathbf{j}\beta, \mathbf{j}'\beta' \rangle) > 0$. For the sake of comparison with the single-polaron mobility equation 7.16 also defines the effective dimensionless bipolaron mobility μ_{bp} per single particle/hole. For a convergence analysis of polarons and bipolaron conductivity, see Appendix D.

We calculate the polaron and bipolaron mobilities at any given T by averaging over Markov chains of the system configurations obtained by means of MC simulations. We used periodic boundary conditions on a system size LxL = 30x30 after carefully checking for any size effects. The shape of the $V_{JT}(\mathbf{i})$ was taken to be nonzero only for $|\mathbf{i}| = 1$ and was therefore specified by a single parameter $V_{JT}(1,0) = V_{JT-eff}$. To minimize further the computation time we limit the maximum hopping distance. After a careful check for convergence we set $\alpha = 1$ and selected the maximum hopping distance, $r_c = 8$ (see Appendix C). In Fig. 7.1 we plot calculated temperature dependence of mobilities at different dopings, where $n < 0.5$ represents particle and $n > 0.5$ hole doping regions.

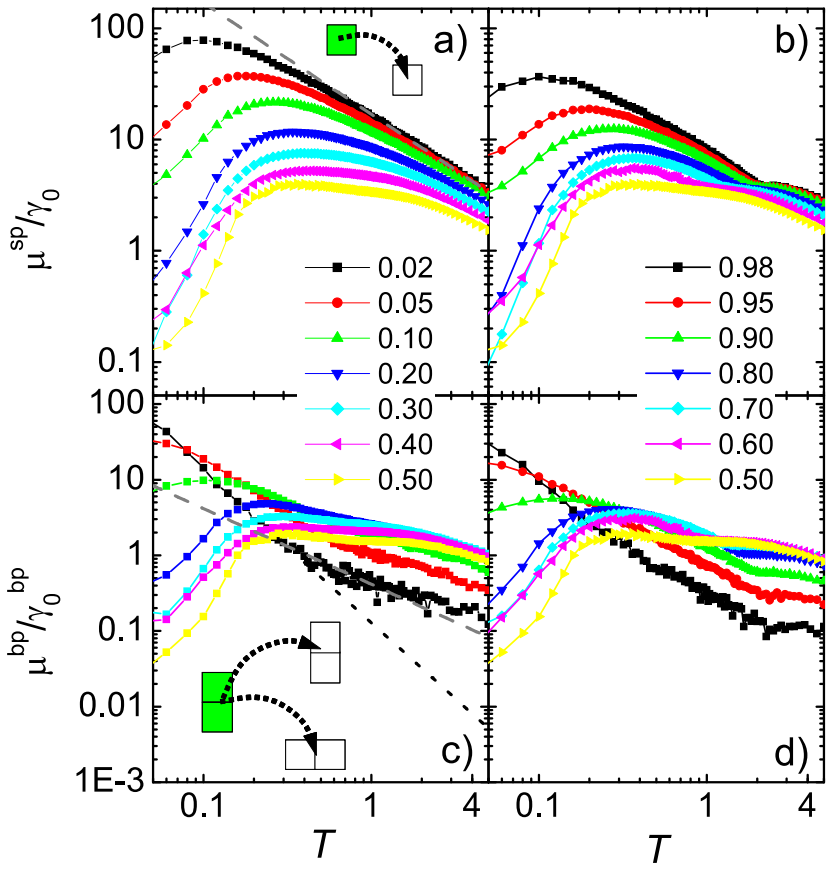

FIGURE 7.1: Temperature dependence of the single polaron mobility, μ^{sp}, (a) and (b) and the effective bipolaron mobility, μ^{bp}, (c) and (d) at $V_{JT-eff} = -1$. In the insets the corresponding hopping processes are shown schematically.

At high T the second exponent in the sums (7.10) and (7.15) shows a negligible temperature dependence so the dominant contribution to temperature dependence of both mobilities comes from the $1/T$ prefactor. When the temperature is decreased we first observe the suppression of mobilities due to the orbital (pseudospin) ordering (see chapter six) in the hole doping region, $n \geq 0.5$, which is most pronounced in the single polaron mobility. The suppression is due to the high energy cost of the hops with the pseudospin flip in the orbital ordered system which makes half of the final states almost inaccessible.

With further decrease of temperature, the behavior of the mobility at low particle and low hole doping becomes almost identical: The single polaron mobility shows a maximum at any doping at the temperature T_M^{sp} , which is doping dependent. In contrast, the maximum is absent for bipolaron mobility at low particle/hole doping. The bipolaron mobility even starts to increase faster than $1/T$ at low temperatures exceeding the single polaron mobility at low particle/hole doping and sufficiently strong attractive JT interaction, $V_{JT} \leq -1$ (see Fig. 7.2). This is the most important result of our

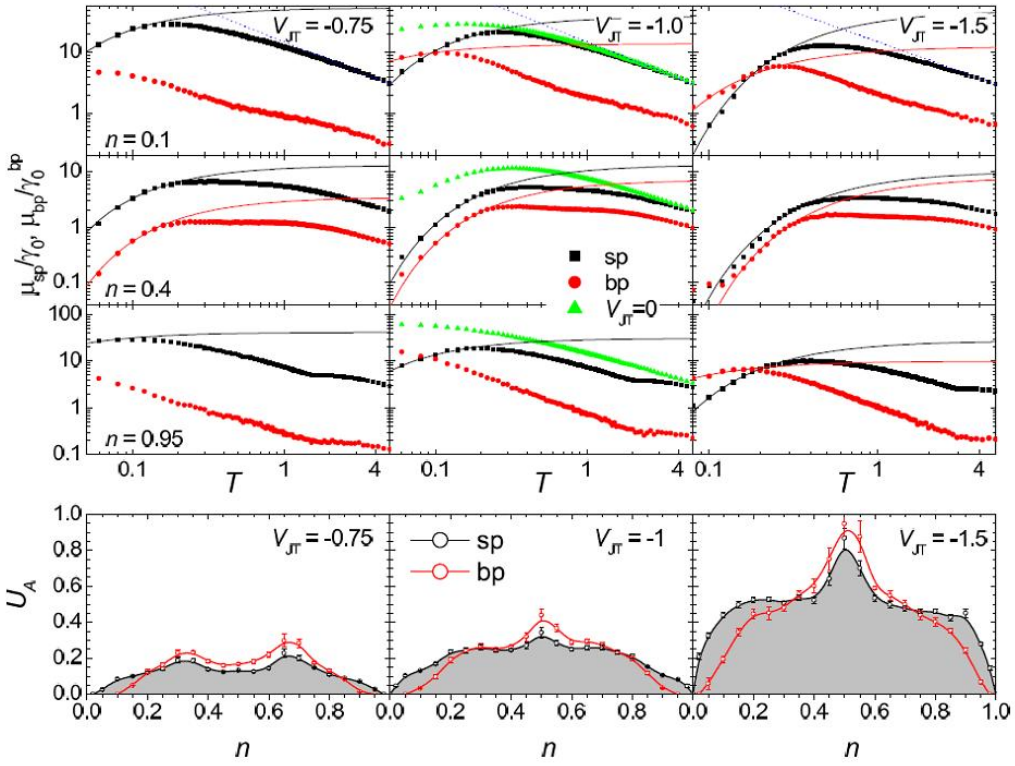

FIGURE 7.2: Polaron and bipolaron mobilities at three dopings: $n = 0.1, 0.4, 0.95$ (top to bottom rows) and three JT couplings: $V_{JT} = -0.75, -1.0, -1.5$ (left to right columns). For comparison the single-charge mobility in the absence of the JT interaction is also shown. Thin full lines are low-T Arrhenius fits and dotted lines show T^{-1} slope. Panels at the bottom show the activation energy, U_A, as a function of doping

calculations. The explanation of this effect follows from the the fact that all particles in the cluster are paired, therefore formation of the clusters with odd number of particles is highly energetically unfavorable. With increased doping and strength of the attractive JT interaction also μ_{bp} starts to show an inflection point at the temperature, T_M^{bp} , which is always lower in the bipolaron case. Below T_M^{sp} (T_M^{bp}) both mobilities show an Arrhenius temperature dependence. The activation energies clearly show a smaller energy barrier for bipolaron hopping in comparison to single polaron hopping.

In our simulation μ_{bp}/γ_0^{bp} exceeds μ_{sp}/γ_0 at small doping and low temperature. This however does not imply that the bipolaron mobility cannot dominate the charge transport even at the intermediate dopings and for weaker JT attractions. If the binding energy of a bipolaron is larger than the phonon frequency, the single phonon processes which break the bipolaron are forbidden. The prefacer γ_0 in the single particle hopping probability (2) will be therefore strongly suppressed because more then one phonon is necessary to conserve energy. On the other hand, the bipolaron hopping processes do not require real bipolaron breaking. As our simulations show (see bottom panels in Fig. 7.2), the bipolaron hopping processes can have a lower energy barrier even with

a moderate JT attraction and can be assisted by a single phonon leading to $\gamma_0^{bp} > \gamma_0$. This results in a further suppression of the single polaron with respect to the bipolaron transport.

7.7 Conclusions

In this chapter we computed the transport properties of polarons and bipolarons in the charge segregated state of doped classical strongly correlated systems in the hopping regime, we analyzed the electrical conductivity of a quasi-2D system with charge segregated polarons in a textured state driven by the Coulomb interaction. We have shown that at high temperature mobility of carriers increases with decreasing temperature as T^{-1}. Single-polaron mobility shows a maximum at the characteristic temperature where clusters start to form. Below this temperature, the single-polaron conductivity is exponentially suppressed because the single-polaron hopping requires dissociation of the polaron from a cluster. On the other hand, the bipolaron transport shows a weaker suppression, which starts at a lower temperature, and thus becomes the dominant transport channel at low temperatures. The conductivity we obtained at dilute concentrations, may be related with the anomalous conductivity behavior observed in cuprates in the underdoped regime. We can infer from our results that at this doping the conductivity has contributions from $2e$ charged objects.

Chapter 8

Conclusions.

The phenomenological theory of Coulomb frustrated first order phase transition was formulated for a layered system. Two cases were studied with different couplings of charge density and order parameter. By eliminating the charge degrees of freedom we derived the free energy as a function of the order parameter. This energy expression includes a nonlocal gradient term which tunes the phase separation. Using numerical minimization of the free energy we found that it allows a few competing patterns. Charged clusters with stripe-like or bubbles-like shapes dominate different regions of the phase diagram at the intermediate Coulomb frustrated regime. In the case of a quadratic coupling we demonstrated that as the temperature decreases the transition to the ordered phase goes through the series of first order phase transitions. Similarly for the linear coupling, as the doping is modified, we observed either stripes or bubble domains. High degrees of frustration leads to a glassy phase where several patterns represent local minima at equivalent energies. Each of these phases is characterized by a different ordering of the charged clusters. In addition we investigated the role of disorder. Here we showed the crossover region where the inhomogeneous phase is not stable against this random perturbation.

Although the phenomenological approach avoids any microscopic interpretation, it can describe phase transitions in a wide class of microscopic models where Coulomb repulsion is explicitly considered. In particular, the quadratic coupling can be realized in two-fold degenerated systems, such as those where the JT effect is present. Thus, based on JT pairing we complement this model with a fine-grained approach. In this way we developed a 2D lattice gas model which includes 3D long-range Coulomb interactions. The results obtained from this model confirm that the charge segregation and more specifically the stripe phase, can be explained on the basis of these two competing forces. By means of Monte Carlo simulations we calculated single particle DOS. We observed

a suppression of DOS in a gap which separates occupied and unoccupied states. Gaps coincide with the onset of clustering and orbital ordering. The origin of these gaps is found in the Coulomb and the JT interactions. Moreover, we could observe the existence gaps whose origin is related to the energy to break each of the four possible bonds created during the cluster formation.

In addition we computed polaron and bipolaron transport properties. Here we applied a hopping scheme for particles moving among charged regions. We showed that bipolarons present lower mobility than single particles at high temperatures. But once clusters and single bipolarons are formed at low temperatures, bipolarons mobility exceeds the single polaron mobility at dilute carrier concentrations. Along the the thesis we tried to bring our results into the context of the cuprates. We think they could be relevant for some of the phenomena observed, particularly in the pseudogap region.

Acknowledgements

First and foremost, I would like acknowledge to my advisors Assist. Prof. dr. Viktor Kabanov and Asst. Prof. dr. Tomaž Mertelj for their guidance throughout the course of this thesis. I am grateful to count with their experience and knowledge from which I learned a lot. Besides, I am thankful to Prof. Dragan Mihailovič for giving me an opportunity to be a part of his group at Complex Matter Department as well as for stimulating conversations.

I am indebted to many of my colleagues and staff at the Complex Matter Department at Jožef Stefan Institute. Special thanks goes to dr. Primož Kušar for his valuable tips in programming and coding in C++. For his help with the reading and comments of the thesis, the due thanks goes to Mathieu Lu-Dac. My sincere thanks to Smiljana Golja, Martina Knavs and Tamara Matevc, they made available their support in a number of ways.

This thesis would not have been possible without financial support of the Mexican agency CONACYT, the Slovenian agencies Ad-futura and CEMEPIUS as well as budget coming from the Complex Matter Department.

I owe me deepest gratitude to my friend dr. Jose Mustre de Leon for introducing me to the fascinating world of research and also for his constant encouragement.

I would like also to show my gratitude to my friend Ferguson Lyndy Willis from whom I learned not only to have a curious attitude beyond physics, but more importantly to understand the joy of the daily facts.

Pero sobre todo, agredesco a mi madre, hermanos y sobrinos quienes le dieron sentido a mi trabajo. A ellos dedico esta tesis. Tambien a mi primo Enrique Argoytia y a mi amigo Sergio Rodriguez; fueron ellos los que realmente iniciaron este tesis.

Appendix A

Conjugated gradient method

The function for which we try to find a minimum is $F(\mathbf{x})$. An unconstrained optimization procedure starts by choosing a starting point; i.e. an initial guess $\mathbf{x}_0$ for the values of the parameters. A substantial amount of computing time can be saved, and the possibility of actually finding a minimum increased, by choosing with some care $\mathbf{x}_0$.

Once the initial point is chosen, we must make two decisions before the next point can be generated: (i) we must first pick a direction along which the next point is to be chosen, and (ii) we must decide on a step size to be taken in that chosen direction. We then have the following iterative picture

$$\mathbf{x}_{k+1} = \mathbf{x}_k + \lambda_k \mathbf{d}_k, \quad k = 0, 1, ..., \tag{A.1}$$

where $\mathbf{d}_i$ is the direction and λ_i is the step size. The different optimization methods differ in the choice of $\mathbf{d}_i$ and $\lambda_i \mathbf{d}_i$. Roughly speaking, we can classify these methods into three categories: 1) methods using only F, 2) methods making use of first derivative of F, 3) methods which also requires knowledge of the second derivatives. The two last categories are often also classified as gradient methods. In choosing a method accuracy and especially computing time are of the essence. Category (1) will not be considered here; it is generally accepted that one should make use of first-order derivatives if they are available and not too elaborate to calculate. Category (3) will generally generate points that are sufficiently close to the minimum point in the least number of steps, but that does not necessarily mean that it is the most efficient. The computational costs of computing and handling the second derivatives can be so substantial, that the evaluation of the first derivative alone at several points would take less computing time. Methods of category (2) would then be a preferable choice.

As mentioned above the choice of a local minimizer will depend upon whether it is possible to generate first or second derivatives efficiently, and how noisy the function is. All the local minimizers below assume that the function is locally relatively smooth - any noise will confuse the derivative estimates and may confound the algorithm. Most of the local minimizers below rely on approximating the function about the current point, **a**, using a Taylor series expansion

$$F(\mathbf{a}+\mathbf{x}) = f(\mathbf{a}) + \sum_i \frac{\partial F}{\partial a_i}|x_i + \frac{1}{2}\sum \frac{\partial^2 F}{\partial a_i \partial a_j}|x_i x_j + ... \tag{A.2}$$

Then,

$$F(\mathbf{a}+\mathbf{x}) \approx c - \mathbf{b}\cdot\mathbf{x} + \frac{1}{2}\mathbf{x}^T\mathbf{Q}\mathbf{x}, \tag{A.3}$$

where $c = f(\mathbf{a})$, $b = -\nabla F$, $Q_{i,j} = \frac{\partial^2 F}{\partial a_i \partial a_j}$. Q is called Hessian matrix of the function at **a**

At the minimum, the gradient is zero, so $\mathbf{b} = \mathbf{0}$ and,

$$F(\mathbf{a}+\mathbf{x}) \approx c + \frac{1}{2}\mathbf{x}^T\mathbf{Q}\mathbf{x}, \tag{A.4}$$

where Q is the Hessian evaluated at the minimum point: $\mathbf{a}_{min}$.

The method of steepest descent is the simplest of the gradient methods. The choice of direction is where F decreases most quickly, which is in the direction opposite to $\nabla F(\mathbf{x}_i)$. The search starts at an arbitrary point $\mathbf{x}_i$ and then slide down the gradient, until we are close enough to the solution. In other words, the iterative procedure is

$$\mathbf{x}_{k+1} = \mathbf{x}_k - \lambda_k \nabla F(\mathbf{x}_k) = \mathbf{x}_k - \lambda_k \mathbf{g}(x_k), \tag{A.5}$$

where $\mathbf{g}(\mathbf{x}_k)$ is the gradient at one given point. We want to move to the point where the function F takes on a minimum value, which is where the directional derivative is zero. The directional derivative is given by

$$\frac{\partial F(\mathbf{x}_{k+1})}{\partial \lambda_{k+1}} = \nabla F(\mathbf{x}_{k+1})^T \cdot \frac{\partial \mathbf{x}_{k+1}}{\partial \lambda_k} = \nabla F(\mathbf{x}_{k+1})^T \cdot \mathbf{g}(\mathbf{x}_k). \tag{A.6}$$

Setting this expression to zero, we see that λ_{k+1} should be chosen so that $\nabla F(\mathbf{x}_{k+1})$ and $\mathbf{g}(\mathbf{x}_k)$ are orthogonal. The next step is then taken in the direction of the negative

gradient at this new point and we get a zig-zag pattern. This iteration continues until the extremum has been determined within a chosen accuracy ϵ. What we have here is actually a minimization problem along a line, This is usually solved by doing a linear search (also referred to as a line search); i.e. searching for a minimum point along a line.

The method of conjugate gradients is an attempt to accelerate convergence by using vectors, $\mathbf{d}_i$ and $\mathbf{d}_j$, which are orthogonal with respect to $\mathbf{Q}$

$$\mathbf{d}_i^T \mathbf{Q} \mathbf{d}_j = 0. \tag{A.7}$$

This can be looked upon as a generalization of orthogonality, for which Q is the unity matrix. The idea is to let each search direction $\mathbf{d}_i$ be dependent on all the other directions searched to locate the minimum of through equation. A set of such search directions is referred to as a conjugate set, and it will take a positive definite n-dimensional quadratic function as given in (A.4) to its minimum point in, at most, n exact linear searches.

The best way to visualize the working of conjugate directions is by comparing the space we are working in with a stretched' space. An example of this stretching of space is illustrated in Figure A.1: (a) demonstrates the shape of the contours of a quadratic function in real space, which are elliptical. Any pair of vectors that appear perpendicular in this space, would be orthogonal. (b) shows the same drawing in a space that is stretched along the eigenvector axes so that the elliptical contours from (a) become circular. The search for a minimum of the quadratic functions starts at $\mathbf{x}_0$ in Figure A.1(a), and takes a step in the direction $\mathbf{d}_0$ and stops at point $\mathbf{x}_1$. This is a minimum point along that direction, determined the same way as for the steepest decent method in the previous section. The essential difference between the steepest descent and the conjugate directions lies in the choice of the next search direction from this minimum point. While the steepest descent method would search in the direction $\mathbf{r}_1$ in Figure A.1 (a), the conjugate direction method would chose $\mathbf{d}_1$. In this stretched space, the direction $\mathbf{d}_1$ appears to be a tangent to the now circular contours at the point $\mathbf{x}_1$. Since the next search direction $\mathbf{d}_1$ is constrained to be $\mathbf{Q}$-orthogonal to the previous, they will appear perpendicular in this modified space. Hence, $\mathbf{d}_1$ will take us directly to the minimum point of the quadratic function $F(\mathbf{x})$.

Let us now show how this is related to the Taylor expansion in Eq A.2. Having performed a line minimization along a direction $\mathbf{d}_i$ we would like to choose a new direction $\mathbf{d}_j$ so that minimizing along $\mathbf{d}_j$ will not interfere with the minimization along $\mathbf{d}_i$. We can determine such a direction by using the Taylor approximation at $\mathbf{a}$. The gradient of F near $\mathbf{a}$ is given by

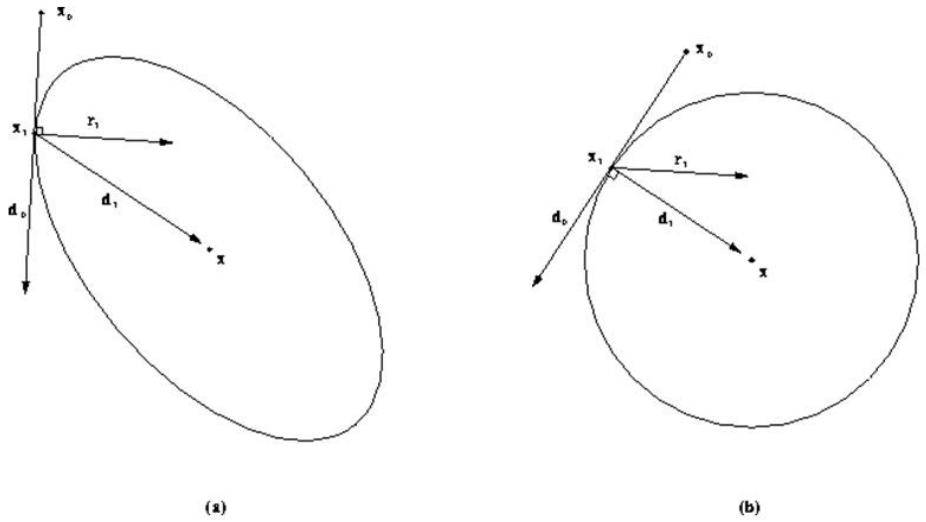

FIGURE A.1: Optimality of the method of conjugate directions. (a) Lines that appear perpendicular are orthogonal. (b) The same problem in a "stretched" space.

$$\nabla F(\mathbf{a} + \mathbf{x}) = \mathbf{Q}\mathbf{x} - \mathbf{b}. \tag{A.8}$$

If we have just minimized along the direction $\mathbf{d}_i$ then the component of the gradient along $\mathbf{d}_i$ must be zero, thus the gradient itself is perpendicular to $\mathbf{d}_i$

$$\nabla F \cdot \mathbf{d}_i = 0. \tag{A.9}$$

As we now move along some direction $\mathbf{d}_j$ the gradient changes by

$$\delta(\nabla F) = \mathbf{Q}\mathbf{d}_j. \tag{A.10}$$

In order not to interfere with our $\mathbf{d}_i$ minimization we require that the gradient remain perpendicular to $\mathbf{d}_i$, ie that the change in gradient itself be perpendicular to $\mathbf{d}_i$. This is simply

$$\mathbf{d}_i^T \mathbf{Q}\mathbf{d}_j = 0. \tag{A.11}$$

If we minimize along each of conjugate directions we will get closer to the minimum efficiently. If the function has an exact quadratic form, one pass through the set will get us exactly to the minimum. Otherwise we must repeat the cycle a number of times.

So, no we can follow in detail how the method works. The initial step is in the direction of the steepest descent:

$$\mathbf{d}_0 = -\mathbf{g}(\mathbf{x}_0) = -\mathbf{g}_0. \tag{A.12}$$

Subsequently, the mutually conjugate directions are chosen so that

$$\mathbf{d}_{k+1} = -\mathbf{g}_{k+1} + \beta_k \mathbf{d}_k. \;\; k = 1, 2, ... \tag{A.13}$$

where the coefficient β_k is given by, for example, the so called Fletcher-Reeves formula:

$$\beta_k = \frac{\mathbf{g}_{k+1}^T \cdot \mathbf{g}_{k+1}}{\mathbf{g}_k^T \cdot \mathbf{g}_k}. \tag{A.14}$$

The step length along each direction is given by

$$\lambda_k = \frac{\mathbf{d}_k^T \cdot \mathbf{g}_k}{\mathbf{d}_k^T \cdot (\mathbf{Q} \cdot \mathbf{d}_k)}. \tag{A.15}$$

The pseudo-code for CGM algorithmic is:

1. Initialize $\mathbf{g}_0 = \nabla F(\mathbf{x}_0)$, $\mathbf{d}_0 = -\mathbf{g}_0$.
2. Determinate the step length $\lambda : F(\mathbf{x}_k + \lambda_k \mathbf{d}_k)$.
3. Calculate the new point: $\mathbf{x}_{k+1} = \mathbf{x}_k + \lambda_k \mathbf{d}_k$.
4. Calculate the gradient: $\mathbf{g}_{k+1} = -\nabla f(x_{k+1})$
5. Determinate the direction of search: $\mathbf{d}_{k+1} = -\mathbf{g}_{k+1} + \beta_k \mathbf{d}_k$.

For details of the method we refer to Numerical Recipes third edition: The Art of Scientific Computing by William H. Press, S. A. Teukolsky, W. T. Vetterling and Brian P. Flannery, Edit. Cambridge University Press (2007).

Appendix B

Dimensionless free energy

Given the thermodynamic potential

$$\widetilde{F}_{pt} = -\frac{\alpha_0}{2}\Lambda^2 + \frac{\beta}{4}\Lambda^4, \tag{B.1}$$

with $\Lambda \equiv \Lambda(\overrightarrow{r})$. Then

If $\Lambda(\overrightarrow{r}) = \sqrt{\alpha_0/\beta}\eta(\overrightarrow{r})$

$$\widetilde{F}_{pt} = \frac{\alpha_0^2}{4\beta}(\eta^2 - 1)^2, \tag{B.2}$$

where it has been taken $t = 0$. Hence $U_0 = \frac{\alpha_0^2}{4\beta}$ (density of the free energy) and $F_{pt} = (\eta^2 - 1)^2$. Since $\widetilde{F}_{pt}$ is measured in unit $[E]/[L]^2$ and F_{pt} is dimensionless, we do a dimensional analysis for the terms 3.8 to 3.11. Given that we use a scaled dimension $x = \xi r$,

$$\widetilde{F}_{pt} = C(\nabla\Lambda)^2 = C\frac{\alpha}{\xi^2\beta}(\nabla\eta)^2 \Rightarrow \frac{[E]}{[L]^2} = \frac{C}{[L]^2} \Rightarrow C \equiv [E]. \tag{B.3}$$

So the normalized factor ξ is

$$\frac{C\alpha}{\xi^2\beta} = \frac{\alpha^2}{4\beta} \Rightarrow \xi = 2\sqrt{\frac{C}{\alpha}}. \tag{B.4}$$

ξ is the coherence length.

Let us define the coupling constant, $\widetilde{\lambda}$ for the dimensionless free density energy.

$$\widetilde{F}_{coup} = -\widetilde{\lambda}(\widetilde{\rho}(\overrightarrow{r}) - \rho_C)\Lambda(\overrightarrow{r}) = \lambda\rho_c(\rho - 1)\sqrt{\frac{\alpha}{\beta}}\eta. \tag{B.5}$$

with $\rho = \widetilde{\rho}/\rho_c$.

F_{coupl} should be related to $\widetilde{F}_{coupl}$ by $\widetilde{F}_{coupl} = U_0 F_{coupl} = U_0\lambda(\rho - 1)\eta$. From the last expression,

$$U_0\frac{4\beta}{\alpha^2}\sqrt{\frac{\alpha}{\beta}}\widetilde{\lambda}\rho_c(\rho - 1)\eta = U_0\frac{4\beta}{\alpha^{3/2}}\alpha^{1/2}\widetilde{\lambda}\rho_c(\rho - 1)\eta, \tag{B.6}$$

Hence,

$$\lambda = \frac{4\beta^{1/2}\widetilde{\lambda}\rho_c}{\alpha^{3/2}}. \tag{B.7}$$

is the dimensionless coupling.

Lastly the LRCI is:

$$F_{Coul} = \frac{K}{2}[\rho(\vec{r}) - \bar{\rho}]\int\frac{\rho(\vec{r'}) - \bar{\rho}}{|\vec{r} - \vec{r'}|}d\vec{r'} = \frac{[E]}{[L]^2}. \tag{B.8}$$

Here ρ is the 3D charge density.

From the relation $\widetilde{F}_{Coul} = U_0 F_{Coul}$,

$$U_0\frac{4\beta}{\alpha^2}\frac{\widetilde{K}}{2}\xi\rho_c^2 = U_0\frac{1}{2}K. \tag{B.9}$$

Thus,

$$K = \frac{4\beta\xi\rho_c^2\widetilde{K}}{\alpha^2}. \tag{B.10}$$

Appendix C

Monte Carlo analysis of convergence

Here we analyze the convergence for selected values of Monte Carlo steps (MC steps) and dimension of the system (LxL). The figure D.1 uses doping $n = 0.15$ and JT coupling $V_{JT-eff} = -1$. DOS is normalized to the number of MC steps, dimension of systems and number of particles. The proper set of variables for MC simulation are based on the error bars and smother curves: LxL = 30x30 and 1000 MC steps,

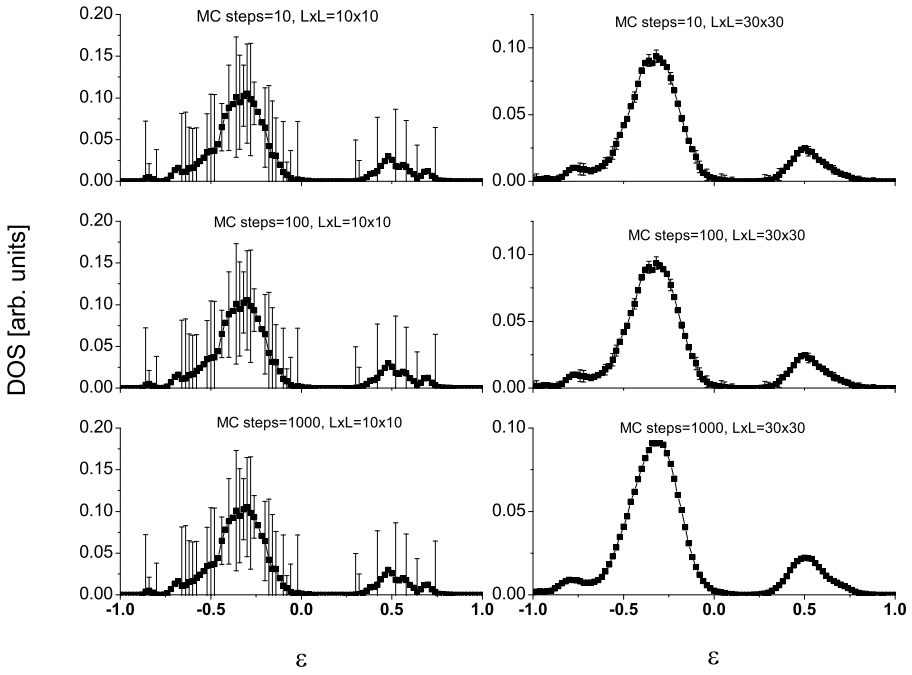

FIGURE C.1: Convergence analysis for DOS, $V_{JT-eff} = -1$, $n = 0.15$. Left column LxL = 10x10, right column LxL = 30x30.

In Figure D.2, polaron and bipolaron mobilities as function of the size of the system (LxL) and the cut-off radius r_c. In both type of mobilities, we assure that the values converge when we fix the parameters JT coupling $V_{JT-eff} = -1$, doping $n = 0.1$ and 1000 MC steps.

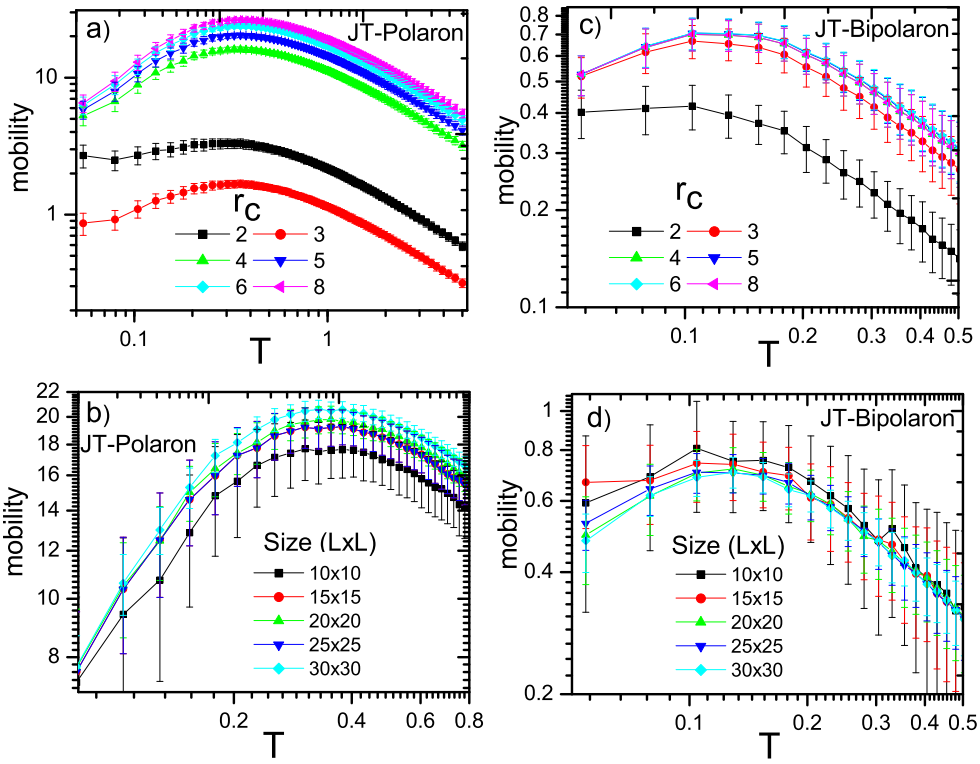

FIGURE C.2: Convergence analysis of the single polaron mobility, (a) and (b) and the effective bipolaron mobility, (c) and (d) at $V_{JT-eff} = 1$, $n = 0.1$. In a) and c) the analysis was done as a function of the cut-off radius, while in c) and d) as a function of the size of the system.

The results for the single JT-polaorn mobility are shown on panels a) and b); while in c) and d) for the JT-bipolaron mobility. In the case of radius cut off, we observe that at $r_c = 6$ both type of mobilities already present a good convergence. Therefore, we use this radius for our MC simulations. Similarly, the dependence on the size of the system already shows good convergence at $LxL = 25$x25. Hence we use this dimension for our studies.

Appendix D

List of publications

Publications from the dissertation.

D.1 Publications in refereed journals

1. *Coulomb frustrated first order phase transition and stripes.* J. Miranda Mena, .V.V. Kabanov, Physica C **468** 358 (2008).

2. *Self-organization of charged particles on a two dimensional lattice subject to anisotropic JahnT eller-type interaction and three-dimensional Coulomb repulsion.* T. Mertelj, V.V. Kabanov, J.Miranda Mena and D. Mihailovic. Physical Review B **76** 054523 (2007).

D.2 Conference proceedings

1. *Gap Opening in a 2D Jahn-Teller-Coulomb model.* J. Miranda Mena, T. Mertelj, V.V. Kabanov and D. Mihailovic. Journal Supercond. Nov Magn **20**, 587-590 (2007).

2. *Bipolaron Jahn-Teller pairing and charge transport in cuprates.* J. Miranda Mena, T. Mertelj, V.V. Kabanov and D. Mihailovic, Journal Supercond. Nov Magn **22**: 281-285 (2009).

3. *Stripe formation induced by doping.* J. Miranda Mena, V.V. Kabanov. Journal Supercond. Nov Magn **22**, 287 (2009).

D.3 Book chapter

1. *Jahn-Teller polarons, bipolarons and inhomogeneities. A possible scenario for superconductivity in cuprates.* Joaquin Miranda. Chapter Review; book: The Jahn-Teller Effect. Springer Series in Chemical Physics Vol. 97 (2010).

Bibliography

[1] Jamei R., Kivelson S., and Spivak B. Universal aspects of Coulomb-frustrated phase separation. *Phys. Rev. Lett.*, **94**:056805, (2005).

[2] Xuan P. A. Gao, Mills A. P.and Ramirez A. P., Pfeiffer L. N., and West K. W. Weak-localization-like temperature-dependent conductivity of a dilute two-dimensional hole gas in a parallel magnetic field. *Phys. Rev. Lett.*, **89**:016801, (2002).

[3] Simonian D., Kravchenko S. V., and Sarachik M. P. Magnetic field suppression of the conducting phase in two dimensions. *Phys. Rev. Lett.*, **79**:2304, (1997).

[4] Kravchenko S. V., Kravchenko G. V., Furneaux V., and Pudalov V. M.and DIorio V. Possible metal-insulator transition at B=0 in two dimensions. *Phys. Rev. Lett*, **50**:8039, (1994).

[5] Editors: Stefan Bluggel and Thomas Bruckel. Lecture notes electronic oxides 4st iff spring-school 2010. *Spring-school Series*, 10, (2010).

[6] Kyle M. Shen, F. Ronning, D. H. Lu, F. Baumberger, N. J. C. Ingle, W. S. Lee, W. Meevasana, Y. Kohsaka, M. Azuma, M. Takano, H. Takagi, and Z.-X. Shen. Nodal quasiparticles and antinodal charge ordering in $Ca_{2-x}Na_xCuO_2Cl_2$. *Science*, **307**:901, (2005).

[7] Tranquada J. M., Woo H., Perring T. G., Goka H., Gu G. D., Xu G., Fujita M., and Yamada K. Quantum magnetic excitations from stripes in copper oxide superconductors. *Nature*, **429**:534, (2004).

[8] Mannella N. et al. Direct observation of high-temperature polaronic behavior in colossal magnetoresistive manganites. *Phys. Rev. Lett.*, **92**:66401, (2004).

[9] Millis A.J. Lattice effects in magnetoresistive manganese perovskites. *Nature*, **392**:147, (1998).

[10] Dai P., Fernandez-Baca J.A., and Wakabayashi N. Short-range polarons correlations in the ferromagnetic $La_{1-x}Ca_xMn_3$. *Phys. Rev. Lett.*, **85**:2553, (2000).

[11] Mori S., Chen C.H., and Cheong S.-W. Pairing of charged-ordered stripes in $(La, Ca)MnO_3$. *Nature*, **392**:473, (1998).

[12] Hotta T., Feiguin A., and Dagotto E. Colossal magnetoresistant material: The key role of phase separation. *Physics reports.*, **344**:1–153, (2001).

[13] Ichikawa N., Uchida S., Tranquada J.M., Niemöller T., Gehring P.M., Lee S. H., and Schneider J. R. Local magnetic order vs superconductivity in a layered cuprate. *Phys. Rev. Lett.*, **76**:3412, (1996).

[14] Hotta T., Feiguin A., and Dagotto E. Stripes induced by orbital ordering. *Phys. Rev. Lett.*, **86**:4922, (2001).

[15] Shen K.M., Ronning F., Lu D.H, and et al. Nodal quasiparticle and antinodal charge ordering in $Ca_{2-x}Na_xCuO_2Cl_2$. *Science*, **307**:901, (2005).

[16] Graf J., d Astuto M., Garcia D.R., Saini N.L., Krish M., and Lanzara A. Bond stretching phonon softening and kinks in the angle-resolved photoemission spectra doped $Bi_2Sr_1.6La_{0.4}O_{6+\delta}$. *Phys. Rev. Lett.*, **100**:227002, (2008).

[17] McQueeney R.J., Sarrao J.L., and Pagliuso P.G. Mixed lattice and electronic states in high-tmepratue superconductors. *Phys. Rev. Lett.*, **87**:077001, (2001).

[18] McQueeney R.J., Petrov Y., Egami T., Yethiraj M., Shirane G., and Endoh Y. Anomalous dispertion of lo phonons in $La_{1.85}Sr_{0.15}Cu_4$ at low temperatures. *Phys. Rev. Lett.*, **87**: 077001, (2001).

[19] Demsar J., Hudej R., Karpinski J., Kabanov V.V., and Mihailovic D. Quasiparticle dynamics and gap structure in $HgBa_2Ca_2Cu_3O_{8+\delta}$ investigated with femtosecond spectroscopy. *Phys. Rev. B*, **63**:054519, (2001).

[20] Deutscher G. Coherence and single-particle excitation in the high-temperature superconductors. *Nature*, **397**:410, (1998).

[21] V. Hinkov et al. Electronic liquid crystal state in the high-temperature superconductor $YBa_2Cu_3O_{6.45}$. *Nature*, **319**:597, (2008).

[22] Hiroyuki Yamase and Walter Metzner. Magnetic excitations and their anisotropy in $YBa_2Cu_3O_{6+x}$: Slave-boson mean-field analysis of the bilayer t-J model. *Phys. Rev. B*, **73**:214517, (2008).

[23] L.D. Landau and E.M. Lifshitz. *Statistical Physics, Part 1. Vol. 5.* Pergamon Press., Oxford, January 1980. ISBN 978-0-750-63372-7.

[24] J. M. Yeomans. *Statistical Mechanics of Phase Transitions*. Oxford University Press, USA, Oxford, June 1992. ISBN 0198517300.

[25] Ortix C., Lorenzana J., and Di Castro C. Frustrated phase separation in two-dimensional charged sytems. *Phys. Rev. B*, **73**:2451171–24511714, (2006).

[26] Ortix C., Lorenzana J., and Di Castro C. Coulomb-frustrated phase separation phase diagram in systems with short-range negative compresibility. *Phys. Rev. Lett.*, **100**:2464021–2464024, (2008).

[27] Fine B.V. and Egami T. Phase separation in the vicinity of a quantum-critical doping concentration: Implication for the high-temperature superconductors. *Phys. Rev. B*, **77**: 014519, (2008).

[28] Kabanov V.V., Mamin R.F., and Shaposhnikova T.S. Localized charges inhomogeneities and phase separation near a second-order phase transition. *JETP.*, **135**:322, (2009).

[29] Jan Zaanen and Olle Gunnarsson. Charge magnetic domain lines and the magnetism of high-T_c oxides. *Phys. Rev. B*, **70**:7391, (2008).

[30] Emery V.J. and Kivelson S.A. Frustrated electronic phase separation and high-temperature superconductors. *Physica C:Superconductivity*, **209**:597, (1993).

[31] Löw U., Emery V.J., Kivelson S.A., and Fabricious K. Study of an Ising model with competing long- and short-range interactions. *Phys. Rev. Lett.*, **72**:1918, (1993).

[32] Gorkov L.P. and Sokol A.V. Phase stratification of an electron liquid in the new superconductors. *JETP Lett.*, **46**:420, (1987).

[33] Alexandrov A.S. and Kabanov V.V. Strings in charge-transfer Mott insulators: Effect of lattice and the Coulomb interaction. *Journ. Supercond.*, **72**:569, (2000).

[34] Kusmartsev F. V. Formation of electron strings in narrow band polar semiconductors. *Phys. Rev. Lett.*, **84**:530, (2000).

[35] Lookman T., Shenoy S.R., Rassmuseen K. O., and A.R. Bishop. Ferroelastic dynamics and strain compatibility. *Phys. Rev. B*, **67**:024114, (2003).

[36] Castellani C., Di Castro C., and Grilli M. Singular quasiparticle scattering in the proximity of charge instability. *Phys. Rev. Lett.*, **75**:4650, (1995).

[37] Mihailovic D., Kabanov V.V., and Muller K.A. The attainable superconductivity T_c in a model of phase coherence by percolating. *Europhys. Lett.*, **57**:254, (2002).

[38] Emery V.J., Kivelson S.A., and Zachar O. Spin gap proximity effect mechanism of high-temperature superconductivity. *Phys. Rev. B*, **56**:6120, (1997).

[39] Muratov C.B. Theory of domain patterns in systems with long-range interactions of coulomb type. *Phys. Rev. E*, **66**:066108, (2002).

[40] Schmalian J. and Wolynes P.G. Stripe glasses: Self-generated randomness in a uniform frustrated system. *Phys. Rev. Lett.*, **85**:836, (2000).

[41] Kivelson S.A. and Emery V.J. *Stripe liquid, crystal, glass phases of doped antiferromagnet. Editors Bianconi A. and Saini L.* Springer, US, April 2006. ISBN 978-0-30646419-5.

[42] Isaac B. Bersuker. *The Jahn-Teller effect.* Cambridge University Press, US, March 2006. ISBN 0521822122.

[43] Teller H.A. and E. Teller. Stability of poliatomic molecules in degenerated electronic states. *Proc. R. Soc.*, **161**:220, (1937).

[44] Alexandrov A. S. *Series in Materials Science: Polarons in Advanced Materials.* Springer, Bristol, UK, April 2007. ISBN 978-1-4020-6347-3.

[45] Hosltein T. Studies of polaron motion : Part ii. the small polaron. *Ann. Phys,*, **8**:343, (1959).

[46] Fröhlich Herbert. Electrons in lattice fields. *Advances in Physics*, **3**:325, (1954).

[47] Alexandrov A. S. and Mott N. *Polarons and bipolarons.* World Scientific, Bristol, UK, March 1996. ISBN 981022298X.

[48] Alexandrov A. S. and Devreese J. T. *Advances in polaron physics.* Springer, Bristol, UK, March 2010. ISBN 978-3-642-01895-4.

[49] Yasutami Takada. Large bipolaron in one- and two-dimensional systems. *Phys. Rev. B*, **26**:1223, (1982).

[50] Hague J. P., Kornilovitch P. E., Samson J. H., and Alexandrov A. S. Superlight small bipolarons in the presence of a strong Coulomb repulsion. *Phys. Rev. Lett.*, **98**:037002, (2007).

[51] Müller K.A. *Structural Phase Transition and Soft Modes. Editors E.J. Samuelsen, E. Anderson and J. Feder.* Universitetsforlag of Oslo, Oslo, March (1971). ISBN 978-3-642-01895-4.

[52] Bednorz J. G. and Müller K.A. Possible high T_c superconductivity in the Ba-La-Cu-O system. *J. Phys.: Condens. Matter.*, **64**:189, (1986).

[53] Wu K. M. et al. Superconductivity at 93 K in a new mixed-phase $Y - Ba - Cu - O$ compound system at ambient pressure. *Phys. Rev. Lett.*, **58**:908, (1987).

[54] Dai P., Chakoumakos B. C., Sun G. F., Wong K. W., Xin Y., and Lu D. F. Synthesis and neutron powder diffraction study of the superconductor $HgBa_2Ca_2Cu_3O_{8+\delta}$ by Tl substitution. *Physica C:Superconductivity*, **243**:201, (1995).

[55] Mihailovic D., Foster C. M, Voss K., and Hegeer A.J. Application of the polaron-transport theory to $\sigma(\omega)$ in $Tl_2Ba_2Ca_{1-x}Gd_xCu_2O_8$, $YBa_2Cu_3O_{7-x}$, and $La_{2-x}Sr_xCuO_4$. *Phys. Rev. B.*, **42**:7989, (1990).

[56] Falck J. P., Levy A., Kastner M.A., and Birgenaou R.J. Optical excitation of polaronic impurities in La_2CuO_{4+y}. *Phys. Rev. B*, **48**:4043, (1993).

[57] Falck J. P., Levy A., Kastner M.A., and Birgenaou R.J. Charge-transfer spectrum and its temperature dependence in La_2CuO_4 $\sigma(\omega)$ in $Tl_2Ba_2Ca_{1-x}Gd_xCu_2O_8$, $YBa_2Cu_3O_{7-x}$, and $La_{2-x}Sr_xCuO_4$. *Phys. Rev. Lett.*, **69**:1109, (1992).

[58] David Emin. Large-bipolaron transport and cuprate superconductors. *Phys. Rev. B*, **45** : 5525, (1992).

[59] Mustre de Leon J., Batistic I., Bishop A. R., Conradson S. D., and Trugman S. A. Polaron origin for anharmonicity of the axial oxygen in $YBa_2Cu_3O_7$. *Phys. Rev.Lett.*, **68**:3236, (1992).

[60] Bilinge S. J. L. and Egami T. Short-range atomic structure of $Nd_{2-x}Ce_xCuO_{4-y}$ determined by real-space refinement of neutron-powder-diffraction data. *Phys. Rev. B.*, **47**: 3236, (1993).

[61] Salkola M., Bishop A. R., Mustre de Leon J., and Trugman S. A. Dynamic polaron tunneling in $YBa_2Cu_3O_7$: Optical response and inelastic neutron scattering. *Phys. Rev. B.*, **49**:3671, (1994).

[62] Boin E. S., Kwei G. H., Takagi, H., and Billinge S. J. L. Neutron diffraction evidence of microscopic charge inhomogeneities in the CuO_2 plane of superconducting $La_{2-x}Sr_xCuO_4(0 \leq x \leq 0.30)$. *Phys. Rev.Lett.*, **84** :5856, (2000).

[63] Mustre de Leon J., Acosta-Alejandro M., Conradson S. D., and Bishop A. R. Evidence for a local structural change in $La_2CuO_{4.1}$ across the superconducting transition. *Journ. Supercond.*, **15**:355, (2004).

[64] Bussmann-Holder A., Keller H., Mustre de Leon J., Simon A., Bishop A. R., and Müller K.A. Testing polaron coherence and the pairing symmetry in cuprate superconductors by local probe methods. *Journ. Supercond.*, **23**:295, (2010).

[65] Mertelj T., Demsar J., Podobnik B., Poberaj I., and Mihailovic D. Photoexcited carrier relaxation in $YBa_2Cu_3O_{7-\delta}$ by picosecond resonant raman spectroscopy. *Phys. Rev. B*, **55** :6061, (1997).

[66] Kabanov V.V., Demsar J., Podobnik B., and Mihailovic D. Quasiparticle relaxation dynamics in superconductors with different gap structures: Theory and experiments on $YBa_2Cu_3O_{7-\delta}$. *Phys. Rev. B*, **59** :1497, (1999).

[67] Mihailovic D. Optical experimental evidence for a universal length scale for the dynamic charge inhomogeneity of cuprate superconductors. *Phys. Rev. Lett.*, **94** :207001, (2005).

[68] Claudio Giannetti, Giacomo Coslovich, Federico Cilento, Gabriele Ferrini, Hiroshi Eisaki, Nobuhisa Kaneko, Martin Greven, and Fulvio Parmigiani. Discontinuity of the ultrafast electronic response of underdoped superconducting $Bi_2Sr_2CaCu_2O_{8+\delta}$ strongly excited by ultrashort light pulses. *Phys. Rev. B*, **79** :224502, (2009).

[69] Giacomo Coslovich, Claudio Giannetti, Federico Cilento, Gabriele Ferrini, Hiroshi Eisaki, Nobuhisa Kaneko, Martin Greven, and Fulvio Parmigiani. *Lectures On The Physics Of Strongly Correlated Systems XIII: Twelfth Training Course In The Physics Of Strongly Correlated Systems.Edit. A. Avella and F. Mancini* . American Institute Of Physics, USA, July (2009). ISBN 0735405352.

[70] Loram J. W., Mirza K. A., Cooper J. R., and Liang W. Y. Electronic specific heat of $YBa_2Cu_3O_{6+x}$ from 1.8 to 300 k. *Phys. Rev. Lett.*, **71**:1740, (1993).

[71] Derro D. J., Hudson E. W., Lang K. M., Pan S. H., Davis J. C., Markert J. T., and de Lozanne A. L. Nanoscale one-dimensional scattering resonances in the CuO chains of $YBa_2Cu_3O_{6+x}$. *Phys. Rev. Lett.*, **88** :097002, (2002).

[72] Pan S.H. et al. Microscopic electronic inhomogeneity in the high-T_c superconductor $Bi_2Sr_2CaCu_2O_{8+x}$. *Nature*, **413**:282, (2001).

[73] McElroy K. et al. Relating atomic-scale electronic phenomena to wave-like quasiparticle states in superconducting $Bi_2Sr_2CaCu_2O_{8+\delta}$. *Nature*, **422**:592, (2003).

[74] Gomes K. et al. Visualizing pair formation on the atomic scale in the high-T_c superconductor $Bi_2Sr_2CaCu2O_{8+\delta}$. *Nature*, **477**:569, (2003).

[75] Bardeen J., Cooper L. N., and Schrieffer J. R. Theory of superconductivity. *Phys. Rev. Rev.*, **108**:1175, (1957).

[76] Batlogg B. et al. Isotope effect in the high-T_c superconductors $Ba_2YCu_3O_7$ and $Ba_2EuCu_3O_7$. *Phys. Rev. Lett.*, **58**:2333, (1994).

[77] Kresin V. Z. and Wolf S. A. Microscopic model for the isotope effect in the high-T_c oxides. *Phys. Rev. B*, **49**:3652, (1994).

[78] Gweon G. H. et al. An unusual isotope effect in a high-transition-temperature superconductor. *Nature*, **430**:187, (2004).

[79] Pasupathy A. et al. Electronic origin of the inhomogeneous pairing interaction in the high-T_c superconductor $Bi_2Sr_2CaCu_2O_{8+\delta}$. *Science*, **320**:196, (2008).

[80] Mustre de Leon J., de Coss R., Bishop A. R., and Trugman S. A. Dynamic polaron tunneling in $YBa_2Cu_3O_7$: Optical response and inelastic neutron scattering. *Phys. Rev. B*, **49**:3671, (1999).

[81] Zech D., Keller H., Conder K., Kaldis E., Liarokapis E., Poulakis N., and K. A. Müller. Site-selective oxygen isotope effect in optimally doped $YBa_2Cu_3O_{6+x}$. *Nature*, **371**:681, (2002).

[82] Rubio Temprano D., Mesot J., Janssen S., Conder K., Furrer A., Mutka H., and K. A. Müller. Large isotope effect on the pseudogap in the high-temperature superconductor $HoBa_2Cu_4O_8$. *Phys. Rev. Lett.*, **84**:1990, (2000).

[83] Rubio Temprano D., Conder K., Furrer A., Mutka H., Trounov V., and K. A. Müller. Oxygen and copper isotope effects on the pseudogap in the high-temperature superconductor $La_{1.81}Ho_{0.04}Sr_{0.15}CuO_4$ studied by neutron crystal-field spectroscopy. *Phys. Rev. B*, **66**: 184506, (2002).

[84] Lanzara A., Guo meng Zhao, Saini N. L., Bianconi A., Conder K. Keller H., and K. A. Müller. Oxygen-isotope shift of the charge-stripe ordering temperature in $La_{2-x}Sr_xCuO_4$ from x-ray absorption spectroscopy. *Journal of Physics: Condensed Matter*, **11**:254, (1999).

[85] Khasanov R., Shengelaya A., Maisuradze A., La Mattina F., Bussmann-Holder A., Keller H., and K. A. Müller. Experimental evidence for two gaps in the high-temperature $La_{1.83}Sr_{0.17}CuO_4$ superconductor. *Phys. Rev. Lett.*, **98**:057007, (2007).

[86] Khasanov R., Strssle S., Di Castro D., Masui T. Miyasaka S., Tajima S., Bussmann-Holder A., and Keller H. Multiple gap symmetries for the order parameter of cuprate superconductors from penetration depth measurements. *Phys. Rev. Lett.*, **99**:237601, (2007).

[87] Khasanov R., Strssle S., Conder K., Pomjakushina E., Masui T. Miyasaka S., Tajima S., Bussmann-Holder A., and Keller H. Universal correlations of isotope effects in $Y_{1-x}Pr_xBa_2Cu_3O_{7-\delta}$. *Phys. Rev. B*, **77**:104530, (2007).

[88] Keller H. and Bussmann-Holder A. Local electron-lattice interactions in high-temperature cuprate superconductors. *Advances in Condensed Matter Physics*, 2010, (2010).

[89] Bussmann-Holder A., Keller H, Bishop A. R, Simon A., and Micnas R. Unconventional isotope effects as evidence for polaron formation in cuprates. *Eur. Phys. Lett.*, **72**:423, (2005).

[90] Bussmann-Holder A., Khasanov R, Shengelaya A., Maisuradze A., La Mattina F., Keller H., and K. A. Müller. Mixed order parameter symmetries in cuprate superconductors. *Eur. Phys. Lett.*, **77**:27002, (2007).

[91] Keller H., Bussmann-Holder A., and K. A. Müller. Jahn-teller physics and high-t_c superconductivity. *Materials Today*, 11:38, (2008).

[92] Michel D. Kaplan and Benjamin G. Vekheter. *Cooperative Phenomena Jahn-Teller Crystals Modern inorganic chemistry*. Springer, US, June 1995. ISBN 0306449285.

[93] Markiewicz R. S. Van Hove exciton-cageons and high-T_c superconductivity XB. polaronic coupling in the doped material. *Physica C:Superconductivity*, **255**:211, (1995).

[94] Johnson K. H., McHenry M. E., Counterman C., Collins A., Donovan M. M., O'Handley R. C., and Kalonji G. Quantum chemistry and high-T_c superconductivity. *Physica C:Superconductivity*, **255**:211, (1988).

[95] Johnson K. H., Clougherty D.P., and McHenry M.E. Dynamic Jahn-Teller coupling, anharmonic oxygen vibrations and high-T_c superconductivity in oxides. *Mod Phys. Lett. B*, **3**:1367, (1989).

[96] Moskvin A. S., Ovchinnikov A. S, and Kovalev O. S. Jahn-Teller centers and pseudospin effects. *Phys. Solid State*, **39**:1742, (1997).

[97] Gennadi I. Bersuker and John B. Goodenough. Large low-symmetry polarons of the high-T_c copper oxides: formation, mobility and ordering. *Physica C:Superconductivity*, **274**: 267, (1997).

[98] Markiewicz B., Kusko C., and Kidambi V. Pinned Balseiro-Falicov model of tunneling and photoemission in the cuprates. *Phys. Rev. B*, **60**:627, (1999).

[99] Goodenough J.B., Zhou J.-S, and Chart J. Copper oxide superconductors: A distinguishable thermodynamic state. *Phys. Rev. B*, **47**:5275, (1993).

[100] Mihailovic D. and Kabanov. V. V. Finite wave vector Jahn-Teller pairing and superconductivity in the cuprates. *Phys. Rev. B*, **63**:054505, (2001).

[101] Kabanov. V. V. and Mihailovic D. Manifestations of mesoscopic Jahn-Teller real-space pairing and clustering in $YBa_2Cu_3O_{7-\delta}$. *Phys. Rev. B*, **65**:212508, (2002).

[102] Matthias Troyer. *Lectures On The Physics Of Strongly Correlated Systems XIII: Twelfth Training Course In The Physics Of Strongly Correlated Systems.Edit. A. Avella and F. Mancini* . American Institute Of Physics, USA, July (2009). ISBN 0735405352.

[103] Stanislaw Ulam. *A collection of mathematical problems (Interscience tracts in pure and applied mathematics)* . Interscience Publishers, USA, July (1960). ISBN 0735405352.

[104] Metropolis N., Rosenbluth Arianna W., Rosenbluth Marshall N., Teller Augusta H., and Teller E. Equation of state calculations by fast computing machines. *Journal of Chemical Physics*, **21**:1087, (1953).

[105] N. Metropolis and S. Ulam. The Monte Carlo Method. *Journal of the American Statistical Association (American Statistical Association)*, **44**:355, (1949).

[106] Kirkpatrick S., Gelatt C. D. Jr., and Vecchi M. P. Optimization by simulated annealing. *Science*, **47**:671, (1983).

[107] Efros A. L. and Shklovskii B.I. Coulomb gap and low temperature conductivity of disordered systems. *J. Phys. C: Solid State Phys.*, **8**:L49, (1975).

[108] Mott N.F. Conduction in non-crystalline materials III. Localized states in a pseudogap and near extremities of conduction and valence bands. *Phil. Mag*, **19**:835, (1969).

[109] Kornilovitch P.E. Band structure of the Jahn-Teller polaron from quantum Monte Carlo. *Phys. Rev. Lett.*, **84**:1551, (2000).

[110] Takada Y. Effective mass of the $E \bigotimes e$ Jahn-Teller polaron in comparison with the Holstein polaron. *Phys. Rev. B*, **61**:8631, (2000).

[111] Barenzten H. An analytic study of the $E \bigotimes e$ Jahn-Teller polaron. *Eur. Phys. Lett.*, **24**: 197, (2001).

[112] El Shawish S., Bonča J., Li-Chung Ku, and Trugman S. A. Numerical study of the $E \bigotimes e$ Jahn-Teller polaron and bipolaron. *Phys. Rev. B*, **67**:014301, (2003).

[113] Mott N.F. *Electronic Properties in Non-crystalline materials.* Clarendon press, Oxford, July (1979). ISBN 0198512880.

[114] Shklovskii B.I. and Efros A.L. *Electronic properties of Doped Semiconductors.* Springer-Verlag, Oxford, September (1984). ISBN 0387129952.

[115] Tenelsen K. and Schreiber M. Low-temperature many-electron hopping conductivity in the Coulomb glass. *Phys. Rev. B*, **52**:13287, (1995).

[116] Perez-Garrido A., Ortuno M., Cuevas E., Ruiz J., and Pollak M. Conductivity of the two-dimensional Coulomb glass. *Phys. Rev. B*, **55**:R8630, (1997).

[117] Tsigankov D.N. and A.L. Efros A. L. Variable range hopping in two-dimensional systems of interacting electrons. *Phys. Rev. Lett.*, **88**:176602, (2002).

[118] Somoza A. M., Ortuno M., and Pollak M. Collective variable-range hopping in the Coulomb gap: Computer simulations. *Phys. Rev. B*, **73**:045123, (2006).

[119] Maniadis P., Lookman T., and Bishop A. R. Elasticity driven self-organization of polarons. *Phys. Rev. B*, **78**:1343043, (2008).

[120] Keimer B., Belk N., Birgeneau R. J., Cassanho A., Chen C. Y., Greven M., M Kastner M.A., Aharony A., Endoh Y., Erwin R. W., and Shirane G. Magnetic excitations in pure, lightly doped, and weakly metallic La_2CuO_4. *Phys. Rev. B*, **46**:14034, (1992).

[121] Masatoshi Imada, Atsushi Fujimori, and Yoshinori Tokura. Metal-insulator transitions. *Rev. Mod. Phys*, **70**:892, (1998).

[122] Yoichi Ando, Lavrov A. N., Seiki Komiya, Kouji Segawa, and X. F. Sun. Mobility of the doped holes and the antiferromagnetic correlations in underdoped high- T_c cuprates. *Phys. Rev. Lett*, **87**:017001, (2001).

[123] Doderer T., Tsuei C. C., Hwang W., and Newns D. M. Charge transport in the normal state of electron- or hole-doped $YBa_2Cu_3O_{7-x}$. *Phys. Rev. B*, **62**:5984, (2000).

[124] Milliken F. P., Doderer T., Koch R. H., and Tsuei C. C. Transport in insulating $YBa_2Cu_3O_{7-\delta}$. *Phys. Rev. B*, **62**:5984, (2000).

[125] Martinez B. Fontcuberta J., Seffar A., Piol S, J Garcia-Muoz J.L, and Obradors X. Colossal magnetoresistance of ferromagnetic manganites structural tuning and mechanisms. *Phys. Rev. Lett.*, **76**:1122, (1996).

[126] Viret M., Ranno L., and Coey J. M. D. Magnetic localization in mixed-valence manganites. *Phys. Rev. B*, **55**:8067, (1997).

[127] Chen X.J., Zhang C.L., Gardner J.S., Sarrao J.L., and Almasan C. C. Variable-range-hopping conductivity of the half-doped bilayer manganite $LaSr_2Mn_2O_7$. *Phys. Rev. B*, **68**: 064405, (2003).

List of Figures